SYNTHESIS AND CHARACTERIZATION OF ANISOTROPIC SEMICONDUCTOR NANOCRYSTALS OF MIXED DIMENSIONALITY

WU WENYA

NATIONAL UNIVERSITY OF SINGAPORE

2014

SYNTHESIS AND CHARACTERIZATION OF ANISOTROPIC SEMICONDUCTOR NANOCRYSTALS OF MIXED DIMENSIONALITY

WU WENYA

(*M. Sc. Chemistry, Nanjing University*)

A THESIS SUBMITTED

FOR THE DEGREE OF DOCTOR OF PHILOSOPHY

DEPARTMENT OF CHEMISTRY

NATIONAL UNIVERSITY OF SINGAPORE

2014

DECLARATION

I hereby declare that this thesis is my original work and it has been written by me in its entirety, under the supervision of Assoc. Prof. Chan Yin Thai, (in CHAN LABORATORY (S7-04-04)), Chemistry Department, National University of Singapore, between Aug, 2010 and Aug, 2014.

I have duly acknowledged all the sources of information which have been used in the thesis. This thesis has also not been submitted for any degree in any university previously.

The content of the thesis has been partly published in:

1) "Efficient Color-Tunable Multiexcitonic Dual Wavelength Emission from Type II Semiconductor Tetrapods"
   W. Y. Wu, M. Li, J. Lian, X. Wu, E. K. L. Yeow, M. H. Jhon, Y. Chan* *ACS Nano* **2014**, 8, 9349.
2) "Promoting 2D Growth in Colloidal Transition Metal Sulfide Semiconductor Nanostructures via Halide Ions"
   W. Y. Wu, S. Chakrabortty, C. K. L. Chang, A. Guchhait, M. Lin * and Y. Chan* *Chem. Mater.* **2014**, 26, 6120.

WU WENYA		
Name	Signature	Date

ACKNOWLEDGEMENT

I would like to express my deep gratitude to my thesis advisor Prof. Chan Yin Thai. He is such an inspiring mentor that he could always give us insightful suggestions when experiments seem hopeless. More importantly, I really appreciate his free-style managements on our projects, which eventually leads to various possibilities and interesting scientific achievements. Besides, I would also like to thank my co-supervisor Dr. Lin Ming, for his patient guidance and useful critiques of my research work.

I wish to acknowledge the valuable help provided by my collaborators. Dr. Mark John and Dr. Bharathi from IHPC provided me with important calculations. Dr. Wu Xiangyang, Dr. Xing Guichuan, Dr. Tong Shi Wun and Dr. Ma Liang have helped me a lot in optical, electronic and electrocatalytic characterizations of materials I have synthesized. Advices given by Prof. Jason Yeo and Prof. Edwin Yeow, have been a great help when we were trying to figure out the potential applications for the obtained materials. My grateful thanks are also extended to the international collaborators. Prof. Tamada, Prof. Okamoto, Dr. Xu Xiaoying, Dr. Yoshida and Mr. Keisuke Imazu in Kyushu University, were appreciated for their kind instruction and help when I was in Fukuoka. I am also grateful for the valuable technical support given by Mr. Lim Poh Chong, Mr. Lee Kian Keat, Mr. Lee Ka Yau, Ms. Tan Hui Ru, Mr. Wong How Kwong for handling various characterization equipment that are essential for successful completion of my thesis.

I was lucky to be educated by all my previous teachers in the past 20+ years. My special thanks go to my Master's thesis advisor, Prof. Zhu Jun-Jie in Nanjing University, as well as Prof. Zhang Jian-Rong and Prof. Jiang Liping

in the same group. Without their guidance and encouragement, I may not even come to Singapore and pursue a higher degree.

To all past and present Chan Lab members, I am glad to have been here with you, where we squeezed in that small lab and shared the same bench top, experienced bitter but fascinating research life. My seniors, five doctors came out from Chan Lab, Sabya, Xu Yang, Nimai, Lian Jie and Yile, I have witnessed your successful graduation and wish you all the best in the future. Kai Ling and Yan Zhen, thank you for all the help in my research work during 2013 ~2014. I also want to thank Dr. Asim and Dr. Mingjie, for the valuable and important help in my projects. I would like to express my gratitude to the following people for all the help and support that you have given, Yali, Zhi Min, Xuanwei, Shashank, Tang Xiao, Ziming, Sumit, Kitty, Xinheng, Xinyan, Mingyu, Xinying, Yee Min, Kelvin, Jessica and Yong Wen.

To all my dear friends since childhood, thank you for enriching my life with unforgettable stories. Especially to Junjie, a friend like you is a rare gift. Wish you all have a wonderful life.

Finally, I would like to thank my parents, who brought me to this magnificent world and raised me up with extraordinary love and patience. I was lucky to grow up in such a loving family together with my younger sister Wenlin, which brought me with lots of positive energy. Last but not least, it has been amazing and enjoyable to be batch-mate in school for 11 years with Li, wish us all the best in the journey ahead.

To my family

TABLE OF CONTENTS

Synthesis and Characterization of Anisotropic Semiconductor Nanocrystals of Mixed Dimensionality

SUMMARY

The dimensionality of colloidal semiconductor nanocrystals is a key factor in determining their various physicochemical properties, such as the extent of quantum-confinement, rate of excitonic recombination and surface-to-volume ratio. The overarching goal of this thesis is to investigate these properties in semiconductor nanocrystals of mixed dimensionality. We developed novel synthetic approaches for achieving branched nanoheterostructures comprising of a 0D core with 1D arms, as well as 2D nanosheets with highly anisotropic lateral dimensions. The growth mechanisms of these nanoparticles were investigated and their optical and electronic properties were characterized by ultrafast spectroscopy techniques and within the context of optoelectronic devices. In Chapters 2 and 3, we describe the synthesis and characterization of Type-II InP/ZnS seeded CdS tetrapod nanoheterostructures capable of exhibiting highly photostable multi-wavelength multiexciton emission (MME). These structures were found to possess a wide range of pump-dependent emission color tunability from red to white to blue, which was ascribed to the anisotropic tetrapod morphology and staggered band alignment at the core-arm interface. In addition, via sequentially cation exchange reaction, these Type-II tetrapods could be chemically transformed into Type-I InP/ZnS seeded ZnS tetrapods with wurtzite ZnS arms. Moving from strongly quantum confined branched nanoheterostructures to 2D nanosheets, Chapters

4 and 5 details our efforts to explore novel synthetic approaches for achieving free standing 2D semiconductor nanosheets where halide ions (Cl^- and Br^-) were found to play a decisive role for lateral growth. Via this premise, we successfully synthesized and structurally characterized sheet-like structures of Ni_9S_8 and Cu_2S with thicknesses on the order of ~ 1 nm. We employed this strategy in conjunction with the cation exchange approach to transform the Cu_2S structures obtained into ultrathin PbS nanosheets. The PbS nanosheets possessed a well-defined hexagonal shape, comparatively large lateral dimensions of ~150-200 nm, and an unusual facet orientation whereby the highest surface energy ±{111} facets terminate the top and bottom planes of the PbS nanosheets. Incorporation of the PbS nanosheets into a field effect transistor revealed that they were n-type, which is highly desirable in view of their stability under ambient conditions. We propose that the n-type behavior of these nanosheets may be rationalized in view of their unique structure.

LIST OF FIGURES

LIST OF SCHEMES

LIST OF ABBREVIATIONS

Abbreviation	Actual name
2D	Two Dimensional
AFM	Atomic Force Microscope
ODE	1-octadecene
CB	Conduction Band
CVD	Chemical Vapor Deposition
°C	Degree centigrade
DDA	Dodecylamine
DDT	Dodecanethiol
EDX	Energy-dispersive X-ray spectroscopy
EA	Elemental Analysis
e^-	Electron
EELS	Electron Energy Loss Spectroscopy
EL	Electroluminescence
EQE	External Quantum Efficiency
eV	Electronvolts
FET	Field Effect Transistor
FFT	Fast Fourier Transform
FWHM	Full-width at Half Maxi
g	Gram
HRTEM	High Resolution Transmission Electron Microscopy
HAADF-STEM	High Angle Annular Dark Field-Scanning Transmission Electron Microscopy
h^+	Hole
IR	Infra-Red
KHz	Kilo Hertz
kV	Kilovolts
LED	Light Emitting Diodes
µM	Micro molar
µL	Micro litter
MA	Myristic Acid
MPA	Mercaptopropionic acid
MME	Multiexciton emission

NCs	Nanocrystals
nm	Nanometer
NIR	Near Infra-Red
HPA	n-hexylphosphonic acid
ODPA	n-Octadecylphosphonic acid
PB	Photobleaching
PL	Photoluminescence
$P(TMS)_3$	Tris(methylsilyl) Phosphine
QDs	Quantum Dots
QYs	Quantum Yields
RBF	Round bottom flask
rGO	Reduced Graphene Oxide
SILAR	Successive Ion Layer Adsorption and Reaction
TRPL	Time Resolved Photoluminescence
TEM	Transmission Electron Microscopy
TOP	Trioctylphosphine
TOPO	Trioctylphosphine oxide
TMS	Transition Metal Sulfides
UV	Ultra Violet
VB	Valence Band
VCSEL	Vertical Cavity Surface-Emitting Laser
wz-	Wurtzite
XRD	X-Ray Diffraction
zb-	Zinc blende

CHAPTER 1

General Introduction

1.1 General introduction of colloidal semiconductor nanocrystals

Colloidal semiconductor nanocrystals (NCs) are nanoparticles comprising of a small crystalline inorganic core (1-10 nm) that is stabilized by a capping layer of organic molecules on the surface, thus enabling good suspension in a polar/non-polar solvent system (see **Figure 1.1(a)**).[1] Such NCs are called quantum dots (QDs) because of their unique size-dependent band gaps and tunable optical properties, which is due to the quantum confinement effect.[2] Since the first successful synthesis of colloidal CdSe QDs in 1993,[3] the composition of QDs have vastly expanded from II-VI to I-VI, III-VI, IV-VI and III-V group semiconductors. Examples include, ZnX (X=S, Se, Te),[4] Ag_2X (X=Se/S),[5] In_2S_3,[6] InX (X = P, As),[7, 8] and PbX (X=Se, S).[9] QDs have been fabricated into thin films via the spin coating method and are widely utilized in a range of optoelectronic devices owing to their diverse optical and electronic properties,[10] such as light emitting diodes (LED),[11] solar cells,[12] photo-detectors,[13] field effect transistors (FET)[14]. Besides, due to their narrower fluorescence emission and improved quantum yield (QY), QDs have been intensively used in bioimaging applications as well.[15, 16] **Figure 1.1(b)** is a typical low resolution transmission electronic microscopy (TEM) image of highly monodispersed PbS QDs synthesized via the hot injection method. The high resolution transmission electronic microscopy (HRTEM) image focusing on a single particle is displayed in **Figure 1.1(c)** with its corresponding fast fourier transform (FFT) in **Figure 1.1(d),** which clearly reveals the lattice fringes and the reflection patterns of {220} and {200} planes. This indicates the good crystallinity of the colloidal QDs obtained from a wet-chemistry synthetic approach.

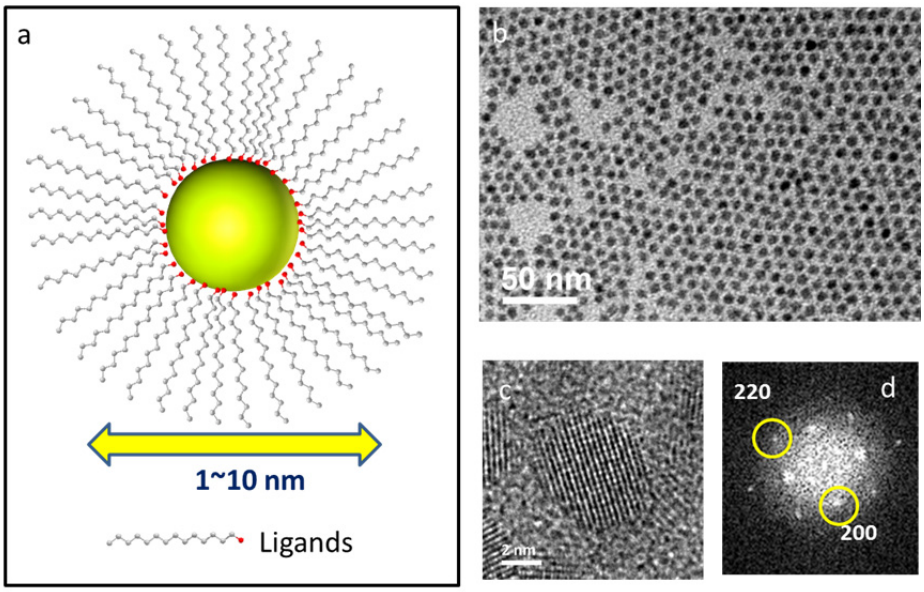

Figure 1.1 Typical colloidal semiconductor nanocrystals. (a) Schematic drawing of NCs surrounded by surfactants, typically primary alkyl amines / acids, or trioctylphosphine / trioctylphosphine oxide; (b) low resolution TEM image of a typical PbS QDs with good size distribution; (c) HRTEM image on a single QD showing clear lattice fringes indicating good crystallinity of the nanocrystals; (d) FFT pattern which corresponds to the single particle displayed in (c) showing reflections from {200} and {220} planes in rock salt PbS crystal.

1.1.1 Electronic states of nanocrystals with different dimensionality

Semiconductors differ from metals in that the Fermi level is within a band gap as illustrated in **Figure 1.2(a)**. The closest band above the band gap is called the conduction band, and the closest band beneath the band gap is called the valence band. The minimum amount of energy required for promoting an electron from valance band to conduction band depends on the size of the band gap. When the electron is excited into the conduction band, a hole is created at the same time in the valence band, resulting in the generation of an exciton (electron-hole pair). The evolution of the electronic state of semiconductor nanocrystals with respect to the decreasing size from bulk to zero-dimensional is shown in **Figure 1.2(b)**. The electronic state is continuous in bulk semiconductor, but progressively becoming discrete with further

decrease of their size. From one-dimensionally confined nanosheets to two-dimensionally confined nanowires, the discrete electronic state becomes more prominent, while further transforms into totally discrete density of states in the case of three-dimensionally confined nanoparticles.

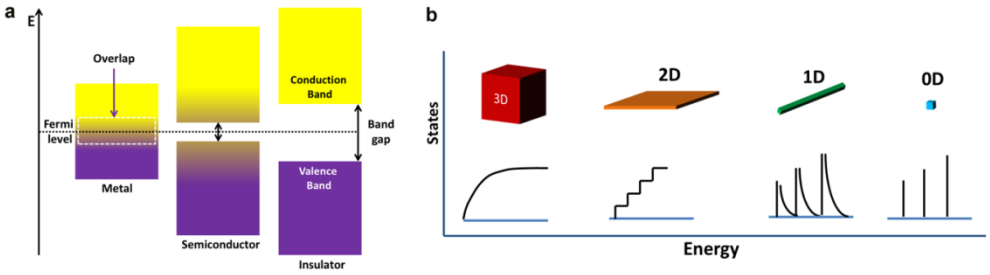

Figure 1.2 Density of state and electronic structures of NCs with different dimensionality. (a) Schematic illustration of density of states in metal, semiconductor, and insulator, showing an increased band gap between conduction band and valence band; (b) density of states for one band of a semiconductor structure with three, two, one and zero dimensionalities. In the three-dimensionality case the energy levels are continuous, while in the "0D" or molecular limit the levels are becoming discrete.

When the dimensions of the semiconductor nanoparticles become close to their Bohr radius, one would observe significant quantum confinement effect causing discrete electronic energy levels in the band edge.[17, 18] As illustrated in **Figure 1.3(a)**, as the particle size shrinks, the band gap increases accordingly, accompanied by blue shifting of photo-luminescence peak as well as first absorbance feature, both presented in **Figure 1.3(b)** and **1.3(c)**. The color tunability and the flexible surface chemistry make quantum dot attractive candidates for various optoelectronic applications as well as bioimaging.

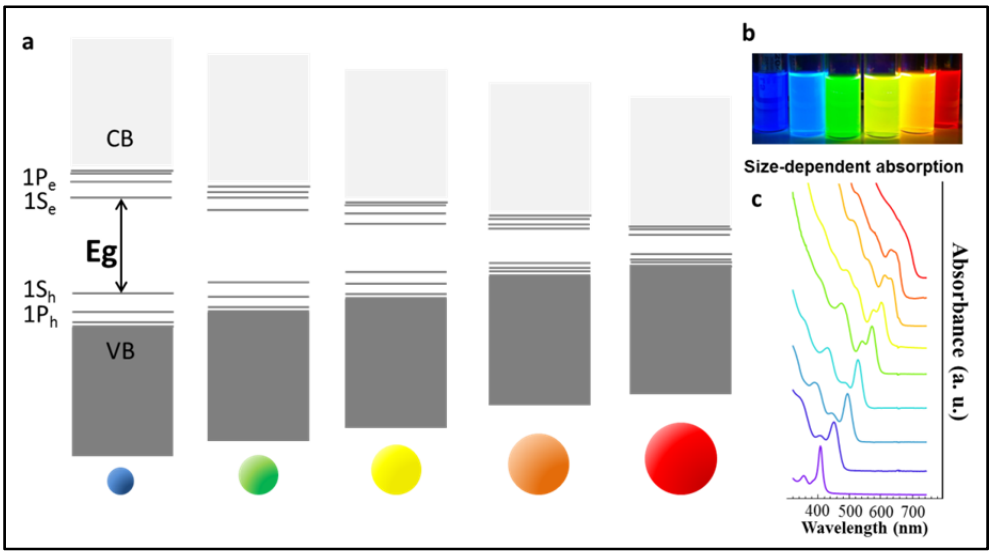

Figure 1.3 Size dependent absorption and PL emission of QDs. (a) Scheme of quantum confinement with size dependent band gap of QDs, where the smaller the nanocrystals, the larger of the band gap; (b) a photograph of CdSe nanocrystals dispersed in hexane, which presented a wide range of emission color tunability from blue to red; (c) a plot of size-dependent UV-vis absorption spectrum of CdSe quantum dots in various sizes, indicating the red shifting the first absorption feature with respect to the increasing size of CdSe quantum dots.

1.1.2 Indium phosphide quantum dots

Besides the well-developed CdSe QDs, Indium Phosphide (InP) is one of the emerging III-V group QDs species has becoming more attractive due to its environmentally friendly cadmium-free components and large Bohr radius up to 15 nm (band gap energy of ~1.34 eV)[19] that allows wide photo luminescence range covering the whole visible spectrum and near IR wavelengths as well.[20] The advent of solution-based synthetic routes to InP NCs dates back to the 1960s.[21] Highly toxic and pyrophoric phosphorous precursors were utilized during that period, such as phosphine gas (PH_3), which were used together with $In(CH_3)_3$ to synthesize InP nanocrystals. As researchers found better alternatives such as the precursor $P(TMS)_3$,[22] this constituted a large step forward to producing InP nanocrystals with the

necessary characteristics of high crystallinity, monodispersity and solubility. Significant contributions to the improvement of quantum yield and colloidal stability of InP NCs were made by Peng et. al., who found that both the fatty acids and noncoordinating solvents were crucial factors for yielding high quality InP quantum dots.[23] The quantum yield of these as-synthesized InP NCs could be increased to almost 60% by further coating with a secondary shell of a wide-band gap semiconductor ZnS, which not only improves its optical performance but also protects the InP core from oxidation.[24]

1.2 Nanoheterostructures: 0D to 3D

Aside from QDs, nanochemistry research has moved on to make tremendous advances in the solution phase synthesis of heterostructured NCs with a well-controlled morphology, size distribution and composition. The nanocrystal heterostructures are multicomponent NCs consisting of two or more different semiconductor material that are joined to each other by chemical bonding interfaces without any molecular bridges.[25] For the interface of two different semiconductors where the intrinsic band gap differs from each other, depending on the relative position of electronic energy levels of the semiconductors involved, there are different cases of band alignment at the interface of the heterostructure. **Figure 1.4(a)** gives an overview of the band alignment of the bulk materials, which are mostly used for synthesis of heterostructures.[26] As illustrated in **figure 1.4(b)**, there are mainly three alignment types, type I, type II, and reverse type I.

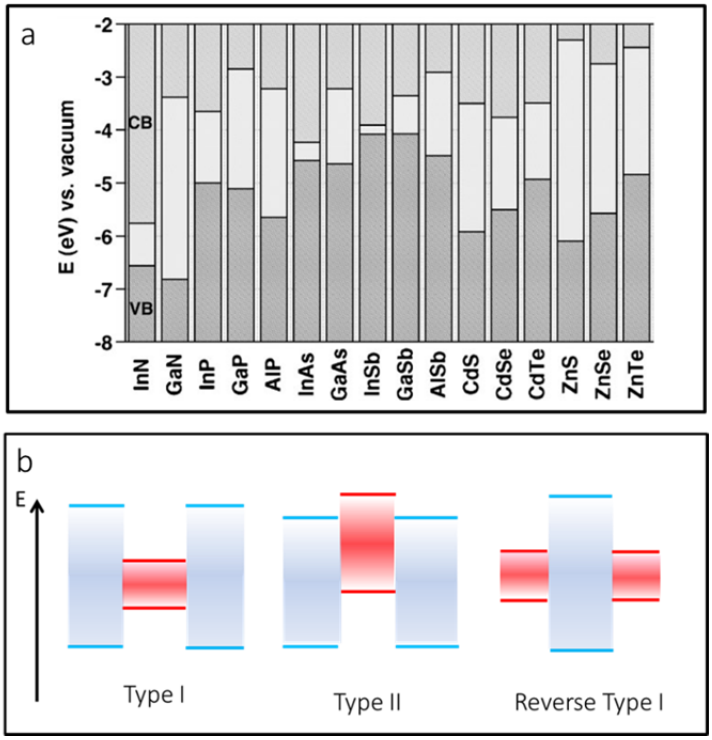

Figure 1.4 Band alignment of selected semiconductors. (a) Electronic energy levels of selected III–V and II–VI semiconductors using the valence-band offsets (VB: valence band, CB: conduction band);[27] (b) schematic representation of the band alignment in different core/shell systems, including type I, type II and reverse type I. Adapted with permission from Ref. 27.

In type I scenario, due to the outer higher band gap material, both electrons and holes are confined in the core which has a comparatively lower band gap. Such band alignment could allow high recombination efficiency of electron and hole while providing brighter QDs. The second staggered band alignment where either the valence band edge or conduction band edge of the shell material is located within the band gap of the core, could cause spatial charge separation upon excitation where the electron and hole go to different domains within the same structure. The third band alignment is the reverse case of Type I where the core possesses a higher band gap than the shell. This kind of structure is not as frequently studied as the previous two cases.

1.2.1 Type I Heterostructures

Type I heterostructures typically aim to elevate the quantum yield (QY) by well-passivation of the core surface with another semiconductor shell that possess a comparatively higher band gap. Such inorganic barrier further protects the core from the surrounding environment and efficiently eliminates the surface trap states, giving rise to an enhanced photo-stability as well as fluorescence quantum yield.

1.2.1.1 Core/shell semiconductor nanocrystals

The most widely studied type of core/shell NCs is the II-VI group semiconductor of CdSe/ZnS, where ZnS shell acts as a physical barrier for the active CdSe core. The synthesis of these NCs was first introduced by Hines and Guyot-sionnest, who managed to get 50% QY NCs by coating CdSe dots with one to two monolayers of ZnS.[28] The ZnS shell has been created by dropwise injection of a mixture of diethylzinc and bis(trimethylsiyl) sulfide into the core solution. Recently, the successive ion layer adsorption and reaction (SILAR) method has been adopted for synthesis of thick shell CdSe/CdS NCs via slow and well-controlled stepwise monolayer epitaxial growth in solution.[29] Due to extensive efforts being made to achieve high QY of these NCs, many type I core/shell NCs have been developed in the field with some of them exhibiting high quantum yield, such as CdSe/ZnSe, CdS/ZnS, ZnSe/ZnS, and CdTe/ZnS.[27]

Compared to II-VI semiconductors, III-V group of NCs are less extensively studied due to the lack of anion precursors, unstable surface conditions and wide FWHM values. InP is the most widely studied III-V compound as its emission could be tuned across the visible range until near IR

by simply changing the size of the QDs, due to the large Bohr radius as mentioned previously. Unlike CdSe QDs, however, the size dispersity of InP NCs have been very large, and was only recently attributed to an Ostwald ripening process which occurs very shortly after the nucleation of InP during its synthesis.[30] The NCs surface is easily oxidized when exposed to air causing extremely low QY, therefore plenty of attempts have been made to improve the surface chemistry and increase the QY. Other than etching the InP NCs surface by HF,[31] higher band gap semiconductors (such as ZnS) has been used to encapsulate InP core in order to increase the QY, either by adopting the similar approach of CdSe/CdS[32] or a single step one-pot synthesis method where a mixture of indium, phosphors, zinc and sulfur precursors along with the solvent and ligands are heated up to 250-300 ^{o}C, which obtains a QY of up to 50%-70%.[33]

It should be noted that the successful synthesis of spherical core/shell heterostructures such as core shell InP/ZnS,[34] core/gradient shell InP/GaP/ZnS[35] and core/shell/shell ZnSe/InP/ZnS[36] (as shown in **figure 1.5(a-c)),** have been reported in literature, some of them possessing high efficiency LED performance as well.[37] Further surface modification of the InP/ZnS core/shell NCs, such as ligand exchange (see **Figure 1.5(d-i)** for the surface modification strategy), could allow water-soluble InP/ZnS QDs to be used in cell-imaging applications.[38] Confocal fluorescence microscopic images shown in **Figure 1.5(d-ii, iii, iv)** demonstrate the high sensitivity for selectivity targeting cancer cells (MiaPaCa cells) while using anticlaudin 4-conjugated InP/ZnS QDs.

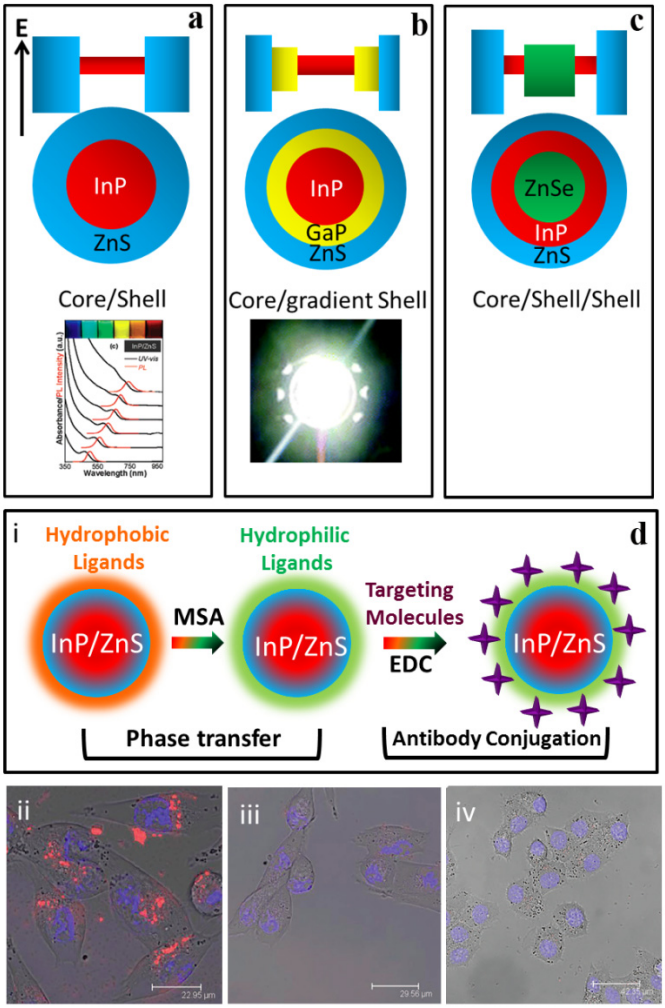

Figure 1.5 Various core/shell heterostructures based on InP QDs: (a) normal InP/ZnS core/shell NCs, with tunable emission covering whole visible range; (b) gradient shell growth over InP core, with improved quantum yield and thus high LED efficiency; (c) a reversed type I band alignment where low band gap InP is sandwiched between two high band gap semiconductor of ZnSe (core) and ZnS (shell); (d) water-soluble InP/ZnS QDs with surface conjugation of antibody for the sensitive cell imaging application: (i) schematic illustration showing the formation of the water-dispersible InP/ZnS QD bioconjugates; (ii) MiaPaCa cells treated with anticlaudin 4-conjugated InP/ZnS QDs light up due to the luminescence of InP/ZnS QDs; (iii) MiaPaCa cells treated with unconjugated InP/ZnS QDs and (iv) KB (human nasopharyngeal epidermal carcinoma cell line) cells treated with anticlaudin 4-conjugated InP/ZnS QD were both dark. Adapted with permission from Ref. 20, 35, 38.

It is clear that the synthesis of InP based nanomaterials is far less developed than those of Cd chalcogenides, where more structurally complex

nanoparticles such as CdSe seeded CdS nanorods and CdTe seeded CdS tetrapods have been synthesized with good uniformity and crystallinity. Therefore, we have explored in this thesis (**Chapter 2**), the unique optical properties of InP QDs while combining with other II-VI semiconductors, notably giving dual color emission from a single species of a branched nanoheterostructure which opens the door for stable and efficient color-tunable LED development.

1.2.1.2 Anisotropic heterostructures

Increasingly sophisticated core/shell architectures have been realized through seeded growth synthetic strategies taking advantage of facet similarity of the core and shell semiconductor materials. A type I CdSe/CdS dot-in-rod heterostructure with high aspect ratio has been firstly achieved by rapid injection of TOP/S as well as the hexagonal wurtzite (wz) CdSe seeds into a hot solvent bath of Cd-ligand complexes.[39] With further decomposition of Cd and S complexes at high temperature, the reaction has been kinetically driven to form the seeded nanorod with the wz-CdSe seed located in an eccentric position across a <001> direction. Alternatively, when a cubic zinc blende (zb) seed is used as shown in **Figure 1.6**, the second semiconductor will selectively nucleate on the {111} facets of the seed, and start to grow and branch into multipods. The most remarkable branched morphologies were the tetrapod[40] and octapod[41] where each heterostructure possess four and eight arms respectively. In this case, the size and number of facets of the starting seed is crucial for determination of the degree of branching, so high quality seeds are pivotal for the yield of the heterostructures with uniform shapes. These seeded nanoheterostructures reveal many interesting physical and chemical properties,

making them potential candidates for next generation optoelectronic applications which will be discussed in the following section with more details.

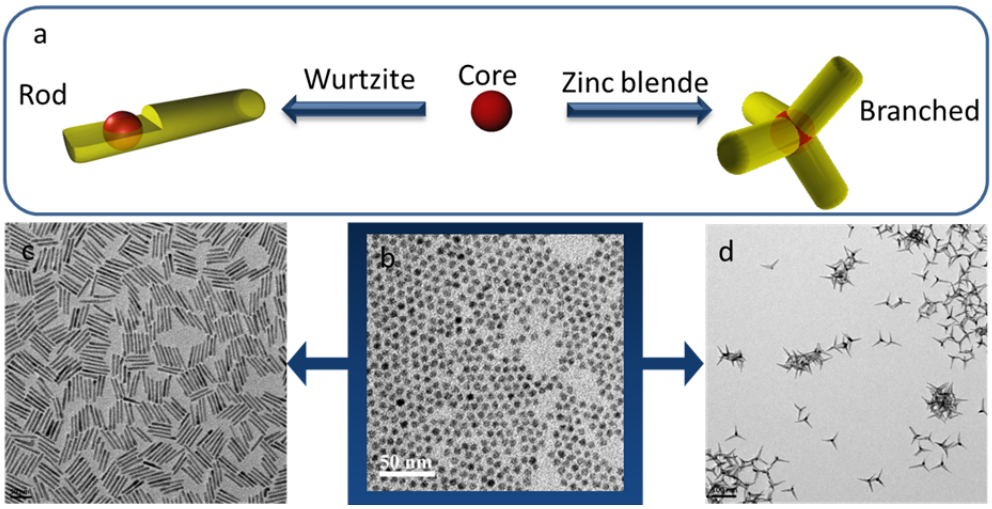

Figure 1.6 Anisotropic nanoheterostructures. (a) Schemetic drawing of seeded growth approach of dot in rod and core/arm tetrapod, which are determined by the crystal structure of the seeds; (b) typical TEM image of CdSe seed; (c) CdSe/CdS seeded nanorods with wurzite CdSe seeds and (d) CdSe/CdS seeded tetrapods with zinc blende CdSe seeds.

1.2.1.3 Bright QDs heterostructures for light emitting devices

The greatest advantage of QDs based LED is the tunable band gap; Due to the quantum confinement effect, the emission shifts towards the blue region as the size of QDs decrease, thus one could easily fabricate QDs emitting at various wavelengths without changing the components. Moreover, the strongly confined electron-hole pairs (excitons) lead to atomic emission-like spectra possessing comparatively narrow linewidth. The core/shell QDs heterostructures acting as the emissive layer usually could allow much higher external quantum efficiency (EQE) when used in QD-LED, because such core/shell structures could effectively reduce non-radiative recombination sites by external inorganic passivation. The first demonstration of red-green-blue electroluminescence (EL) from QD-LED has been shown in **Figure 1.7(a), 1.7(b)** and **1.7(c)** while Kim T. H. et al. have reported a large-area, full-color

QDs display, including flexible form, optimized quantum dot films, well-controlled nano-interfaces and carrier behaviour.[42] They introduced the solvent-free transfer printing method into the LED fabrication procedure, suggested a novel and promising route for creating future large scale devices, such as displays and solid-state photovoltaics.

QD-LED has been further developed recently and shown more interesting behaviours owing to the unique anisotropic shapes and their multicomponent heterostructures, as summarised in **Figure 1.7(b) and 1.7(c)**. The first example was the dual EL coming from CdSe/CdS nanotetrapod, with four extended CdS arms spatially far from CdSe core allowing emission of multiple wavelengths due to radiative excitonic recombination in the different material regions, namely CdSe core and CdS arms.[43] Another striking case has been published in Science, where Cao's group successfully achieved a polarized red-color-emitting QD-LED (see **Figure 1.7(c)**)[44] They adopted highly monodispersed core/shell CdSe/CdS nanorods and assembled them into needle-like super particles, with further lateral alignment along a specific direction on a Si_3N_4 substrate for the fabrication of the polarized LED.

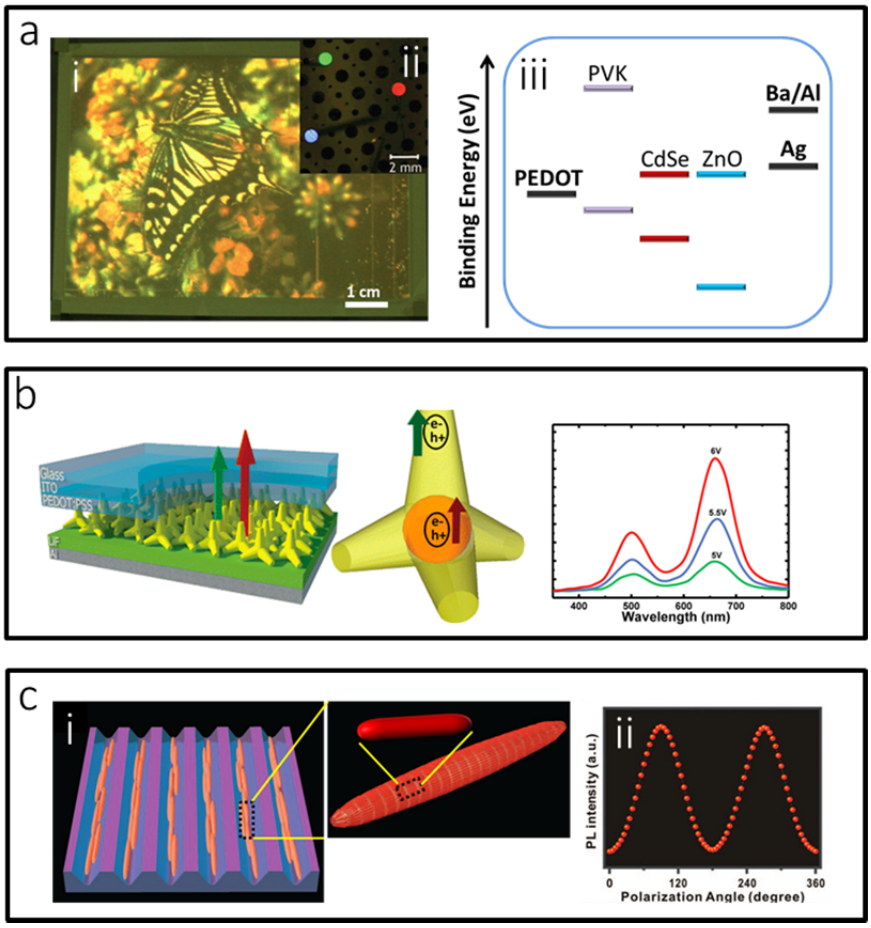

Figure 1.7 Type I anisotropic nanoheterostructures utilized in light emitting devices. (a) Full color quantum dot display fabricated by transfer printing;[42] (i) state-of-the-art QD-LED fabricated into a size of four inch full-color active matrix display (ii) the red-green-blue QD-LED demonstrating a contact printing method for depositing patterned QD monolayer films; (iii) Energy band diagram of QD-LED employing ZnO as the electron injection layer for high-performance devices. (b) CdSe/CdS nanotetrapods acting as the active layer in QD-LED producing two spectrally distinct wavelengths;[43] (c) (i) lateral alignment of needle-like superlattice assembly of nanorods with (ii) PL intensity versus polarization angle as the polarization was manually rotated while measuring a typical superparticle-embedded PDMS thin film under excitation wavelength of 380 nm.[44] Adapted with permission from Ref. 42, 43, 44.

1.2.2 Type II heterostructures

The synthetic strategies for type II heterostructure NCs are more or less the same as those for achieving type I structures through wet chemistry

approaches. It has been extensively studied for the spherical core/shell heterostructures on their tunability of photo-physical properties resulting from variation in the structural parameters. Core/shell spherical NCs (as shown in **Figure 1.8(a)**) are the most explored and various combinations of semiconductors include CdTe/CdSe,[45] ZnSe/CdS,[46] InP/CdS[47] and ZnTe/CdS.[48] On the other hand, shape-control over the NCs heterostructures with anisotropic morphologies potentially provides another approach to vary the electronic state and band alignment at the interface of the adjacent materials. Many examples are shown in **Figure 1.8(b-h)**, with more elaborate multi-component tetrapods, nanorods, barbells, and multbranched architectures.[49] Besides bottom-up synthesis method, cation/anion exchange process has been frequently adopted in recent years to achieve type II heterodimers, such ion exchange reaction is superior in the aspect of the selective formation of a hybrid structure with an epitaxial heterointerface (illustrated in **Figure 1.8(i)**).[50] Alivisatos's group was the pioneer in cation exchange reaction, and they managed to assemble the CdS nanorods onto a substrate, followed by exposing the CdS monolayer to the copper reagent for cation exchange. The Cu^{+} ions could only approach the CdS rods from the exposed single ends across the substrate, resulting in the well-controlled half exchange of the whole monolayer which is naturally a heterojunction for further device fabrication (depicted in **Figure 1.8(j)**).[51] The CdS/CdTe peanuts-like heterodimer in **Figure 1.8(k)** has been achieved via anion exchange of CdS nanoparticle with tri-octylphosphine telluride (TOP-Te). Type II band alignment between CdS and CdTe allowed the charge separation under excitation, where the electrons went into CdS and holes stayed in CdTe.

Using control over volume ratio between the CdS and CdTe during the anion exchange, one could engineer the band structure and alignment in a precise manner.[50]

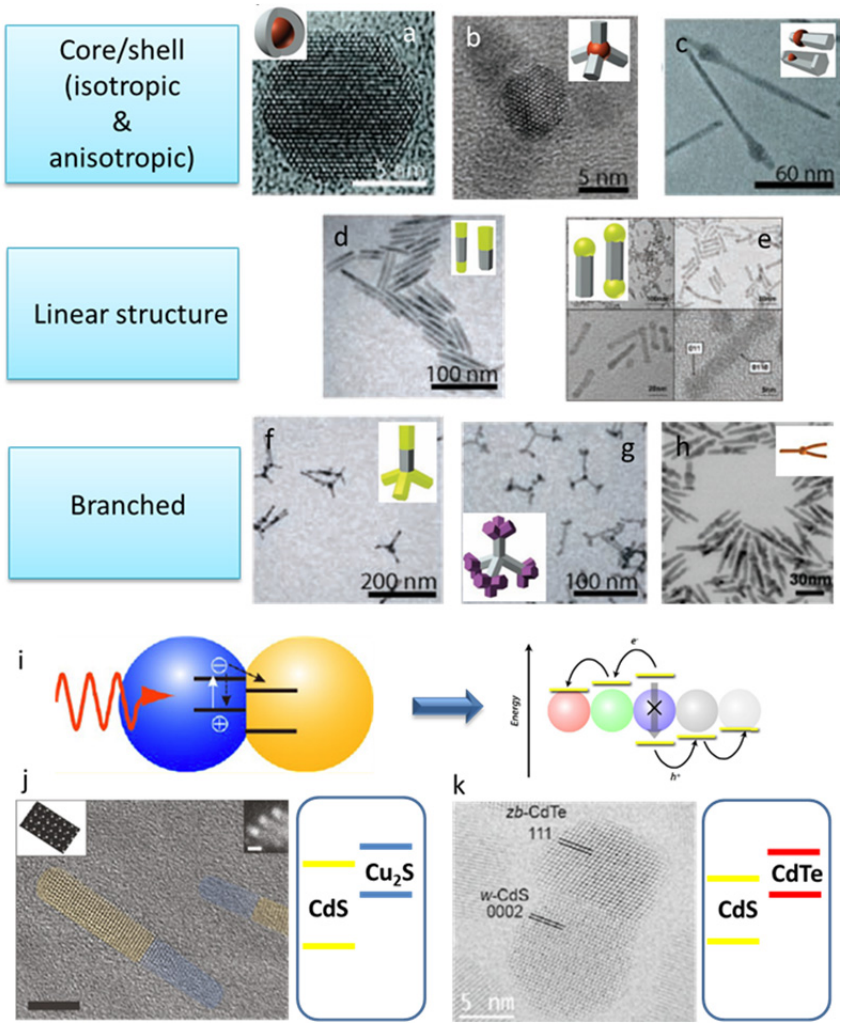

Figure 1.8 Nanoheterostructures with Type II alignment. (a) Core/shell spherical NCs;[52] (b)[53] and (c)[54] are seeded-nanorods and seeded-tetrapods respectively; (d)[55] and (e)[56] are linear heterostructures with barbell shape; (f)-(h) branched heterostructures with multiple different semiconductors;[49] (i) illustration of type II charge transfer in heterodimers;[57] (j) HRTEM of CdS-Cu_2S heterorod obtained by cation exchange with band offset between the two materials;[51] (k) HRTEM of CdS-CdTe heterodimers via anion exchange reaction.[50] Adapted with permission from Ref. 49, 51, 52, 53, 54, 55, 56, 57.

However, contrary to the type I structure, due to the staggered band alignment, the emission of the core undergoes significant red shift while the shell grows atop. The reduced overlap between electron and hole

wavefunctions allowing long-lived lifetime ranging from hundreds of nanoseconds to a few microseconds, which are important implications for applications such as nonlinear optics, lasing and photovoltaic technologies.

Solar cell has been continuously attracting people's attention in the past few decades due to the growing demand for renewable and clean energy, which requires significant efforts in investigation of efficient and low-cost photovoltaic materials. NCs based photovoltaics are probably the most desired candidates that possess the advantages of high stability, inexpensive, solution-processable fabrication, and superior optical and electronic properties.[58] Several works have been reported using NCs with type II band alignment, such as Cu_2S-CdS, CdTe-CdSe, which have rather low efficiency due to shortcuts and insufficient driving force for carrier separation in the active layer. With the improved device fabrication strategies, Loh's group recently reported that type II CdSe/CdTe tetrapods immobilized on oleylamine-functionalized reduced graphene oxide (rGO) sheets could be homogeneously mixed with PCDTBT to form donor–acceptor dispersed heterojunctions and exhibit a high power conversion efficiency of ~3.3% in solar cell devices.[59]

1.3 2D sheet-like nanostructures

Two-dimensional (2D) semiconductor NCs with thickness much smaller than the lateral dimensions have been strikingly highlighted over the past few years since the discovery 2D graphene and vast exploration of other 2D semiconductor materials. Recent research has demonstrated that the arrangement of atoms and the dimensionality of such materials are pivotal and greatly influence their electronic and optical properties.[60] The fast development of optoelectronic devices based on semiconductors strongly

motivate the synthetic field of 2D materials for the achievement of free standing nanosheets that possess ultrathin thickness and well-defined lateral morphology. To this point, wet chemistry synthetic approach is more favoured over Chemical Vapor Deposition (CVD) method, because one could tune the surface chemistry accordingly and easily manipulate the solution processable nanosheets during device fabrication.[61]

To date, various semiconductor nanosheets obtained via wet chemistry method have been reported in literature, including layered and non-layered materials, such as In_2S_3,[62] SnSe(S),[63] CdSe (Te, S),[64] FeS_2,[65] CuS,[66] and PbS.[67] Detailed discussion of the methodologies is presented in the following paragraphs.

1.3.1 Wet chemically synthetic approaches of 2D nanosheets

1.3.1.1 Top-down approach: exfoliation

Inspired by the discovery of scotch-tape exfoliated 2D graphene nanosheets, Coleman et al. demonstrated a general chemical exfoliation method for a group of transition metal chalcogenides in solution, such as MoS_2, WS_2, $NbSe_2$, BN, Bi_2Te_3, with good dispersion in solvent (see **Figure 1.9**) and easy processablility for the composite film during device fabrication.[68] Other groups tried to carry out surface modification of the chemically exfoliated MoS_2 nanosheets for the application purposes, for instance, David et al. have produced a selective artificial protein receptor for β-galactosidase by successfully modulating the ζ-potential of MoS_2 sheets with improved colloidal stability through thiol ligand designs.[69] However the exfoliation method could only be useful for the naturally layered semiconductors with van der waals interaction between each two unit cell

single layers, and the lateral morphology of the obtained 2D sheets via this method were not under control. Hence, the bottom-up synthetic route is highly essential in synthesizing nanosheets for non-layered semiconductors.

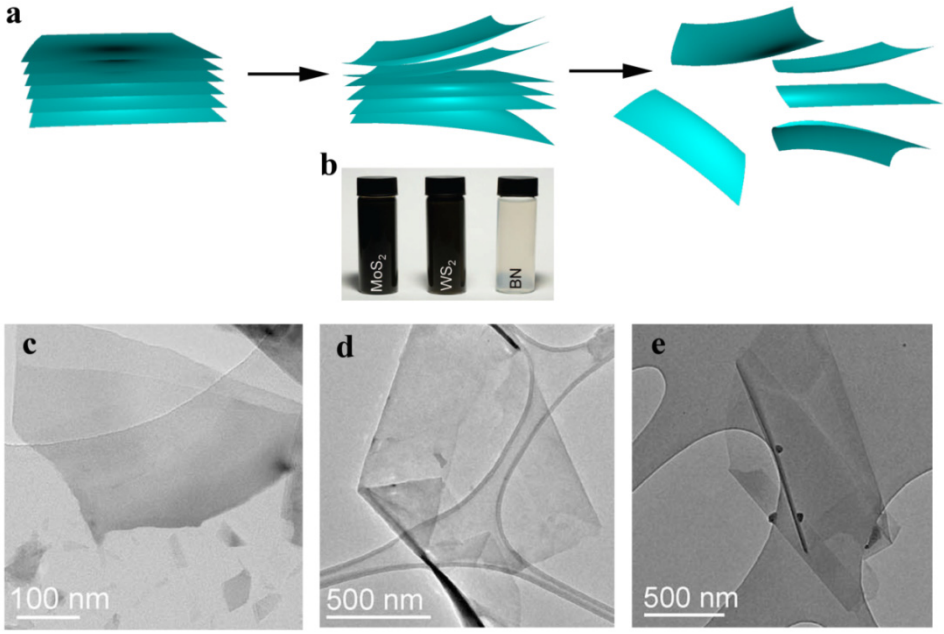

Figure 1.9 Top-down exfoliation approach for achieving 2D layered nanosheets. (a) Scheme of solution phase exfoliation of bulk layered semiconductor for achieving 2D nanosheets; (b) Digital photograph of exfoliated nanosheet suspension, as depicted from the image, the homogenous dispersion of exfoliated nanosheets in organic solvents reveal their potential for further fabrication of solution processable thin films in devices; TEM images showing ultrathin nanosheets achieved via exfoliation method, (c) MoS_2, (d) WS_2, and (e) BN. Adapted with permission from Ref. 68.

1.3.1.2 Bottom-up approach

Synthesis of free standing 2D nanosheets directly in solution has been widely explored in the past few years. Tang et al. have firstly published in Science 2006, introducing a self-assembled template-free mechanism for obtaining free-floating 2D CdTe nanosheets via a wet chemistry approach.[70] The CdTe nanosheets could go beyond micrometer scale in size while keeping a small thickness of 3.4 nm on average. This opens the door for bottom-up synthesis with tremendous opportunities for the design and manipulation of various NCs species. Recently, by injection of chlorine contained solvents into

the reaction pot of the homogenously nucleated PbS nanospheres just beyond the solvents' boiling point, one could trigger an oriented attachment reaction among the existing PbS dots to happen and yield PbS free-standing nanosheets with an average thickness of 2.5 nm and the lateral dimension of up to 500 nm.[67] Although the PbS nanosheets obtained would have some crystal defects, they effectively minimized the charge hopping problem with the large lateral dimension while being fabricated onto a photodetector device.

The most adopted method in recent years, were called the "soft template method". This reaction often takes place in a nonpolar organic system with self-assembly of molecular surfactants in solution to form a lamellar structure which serves as a template for the semiconductor monomers to nucleate and grow within the structure, resulting in flattened 2D nanostructures, as illustrated in **Figure 1.10(a)**. The long-chain surfactants, normally fatty acids or amines, self-assembled into a well-defined lamellar molecular structure leaving the empty thin spacing between each of the two molecular layers, with the metal and sulphur precursors surrounded in a non-polar reaction system. The metal and sulphur precursors then gradually enter the thin spaces, start reacting and forming tiny clusters, further annealing of the products will allow transformation into continuous thin semiconductor sheet-like structures. 2D CdSe has been deeply explored; nanoribbons[71] and nanoplates[72] have been successfully synthesized with alkylamine or acids in the system facilitating the molecular self-assembly of the lamellar template. This process has been especially observed in the CdSe nanoplatelets reported by Ithurria et al.,[73] as shown in **Figure 1.10(b)** and **1.10(c),** which clearly demonstrated the controlled tunability of thickness as well as the unrolling of

CdSe nanoplatelets after CdS shell growth. Beside, Peng's group reported the first zinc blende CdSe plates and demonstrated the pure Cd atom termination of top and bottom faces.[74] Besides CdSe(S), H. Zhang's group developed a general protocol, based on lamellar structure as well, for achieving 2D metal chalcogenides nanosheets. As represented in **Figure 1.10(d)**, they were able to achieve highly monodispersed 2D CuS nanosheet with ultrathin thickness of 2.5 nm and a large lateral dimension reaching 200 nm.[66] This general method could be extended to synthesize ZnS and Bi_2S_3 as well. Other examples such as In_2S_3 nanoplates, have also been achieved via a thiol assisted lamellar structure through a similar growth process, as displayed in **Figure 1.10(e)**.

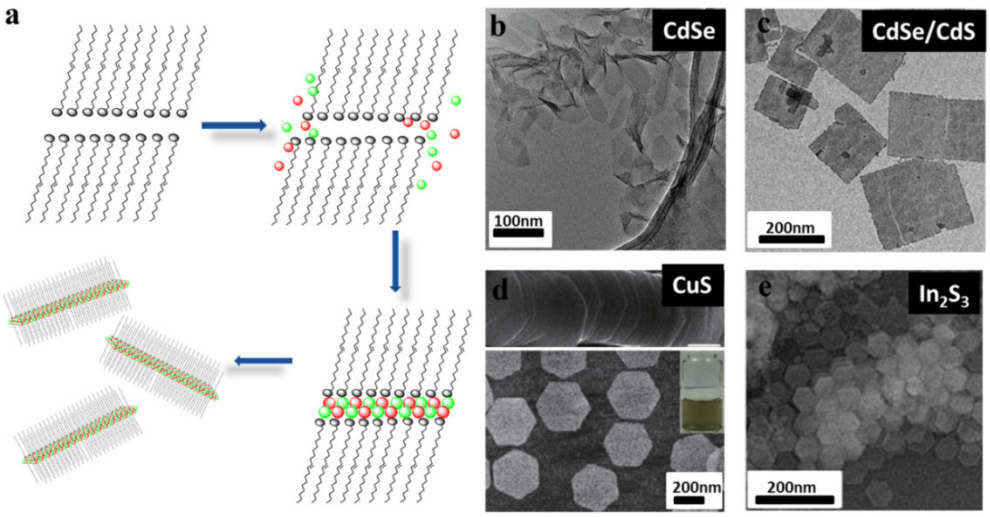

Figure 1.10 Illustration of nanosheet formation mechanism through Lamella structure and the examples of solution processable nanosheets obtained via Lamella structure. (a) Scheme of the Lamella structure formation, the red and green balls represented metal and non-metal atoms with the long chain molecule stood for surfactants that responsible for building lamella structures; semiconductor nanosheets that have been achieved via Lamella structures, such as (b) CdSe,[73] (c) CdSe/CdS,[73] (d) CuS nanosheets,[66] as well as (e) In_2S_3 nanosheets.[62] Adapted with permission from Ref. 62, 66, 73.

Furthermore, 2D nanosheets could also be synthesised via a few more approaches besides soft template method. For instance, addition of a special chelate molecule named 1,10-phenanthroline to the SnSe NCs synthetic pot

resulted in ultrathin 2D nanosheets while removing the molecule instead will lead to flower-like 3D structures. As the 1,10-phenanthroline could not be detected on the surface of as-synthesized nanosheets, it might play the role of modifying the precursor complex without binding to the nanosheet surface (see **Figure 1.11(a)**).[75] Langmuir-Blodgett (LB) assembly on the air-water interface has been adopted as well for obtaining PbS 2D nanosheets with large surface area. This method involves synthesis of PbS nanowires followed by self-assembly via LB film and annealing with higher temperature after compression of the floating PbS nanowires into a close-packed solid film. [76] In **Chapter 4**, we have developed another novel synthetic approach to achieve 2D metal sulphides sheet-like nanostructures with the addition of halide ions. The as-synthesized sheet-like nanostructures could be further used as potential electrochemical catalyst for hydrogen evolution reaction.

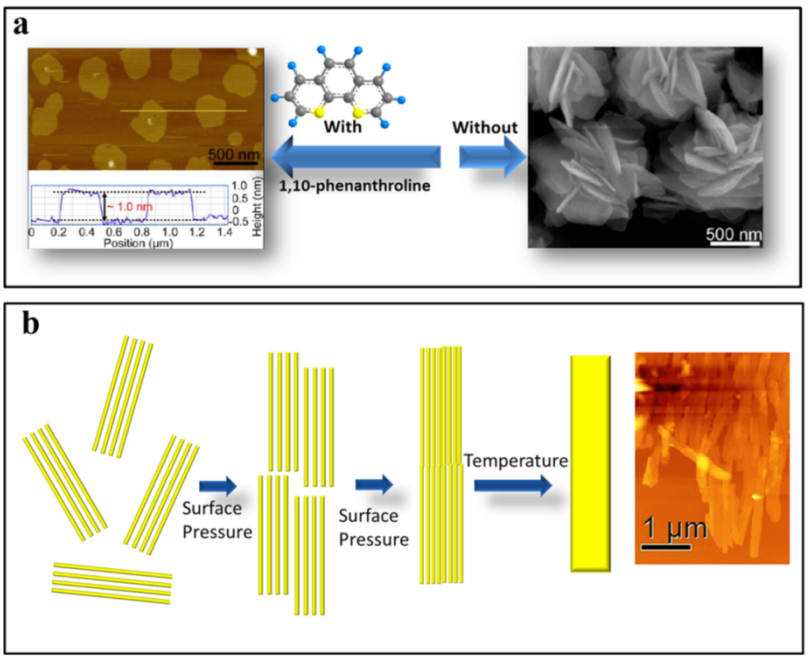

Figure 1.11.Other methods to obtain nanosheet structures. (a) Ultrathin SnSe nanosheets obtained with the presence of 1,10-phenanthroline, and nanoflowers with the absence of such molecule; (b) ultra-large PbS nanosheets achieved via LB compression and higher temperature annealing. Adapted with permission from Ref. 75, 76.

1.3.2 Optical and electronic properties of 2D nanosheets

The electronic wave function of a semiconductor is strongly confined in the case of two dimensional nanosheet, special electronic and optical properties would start to emerge. In the case of CdSe and CdS nanoplatelets, these semiconductor nanoplatelets possess a thickness dependant absorption and emission spectra, as well as an extremely narrow full-width at half-maximum less than 40 meV at room temperature which makes the nanoplatelets the fastest colloidal fluorescent emitters ever.[77]

In other cases, the energy band position could be shifted accordingly. In layered semiconductors, for instance, MoS_2 nanosheets, when the total number of layers decreased from several to two, the indirect band gap would increase from 1.29 eV to 1.6 eV. When there is a single layer of MoS_2, the indirect band gap would transform into a direct one which could result in an even larger band gap and bright photoluminescence.[78] Similar effects have been observed in semiconductors possessing surface plasmonic resonance properties as well. $Cu_{2-x}S$ NCs have exemplified such influence where 2D CuS nanoplates, given its anisotroptic shape, exhibited two plasmonic peaks representing in-plane (Infra-Red (IR) range) and out-plane (Near Infra-Red range) resonences respectively, while the spherical CuS have only one peak located in the near IR wavelength.[79]

1.3.3 Applications based on 2D nanosheets

Since two-dimensional materials have been considered to be one of the most promising candidates for future quantum devices, the field has been pushing for materials which can be easily processed by spin-coating or dip-coating methods during the device fabrication. On one hand, compared to its

spherical counter parts, 2D nanosheets have greater potential in overcoming the tunnel barriers in the active film within each individual sheet given its large lateral dimension while still retaining the one-dimensional confinement along the vertical axis. As mentioned previously, H. Weller's group have recently demonstrated that micrometer-size 2D PbS nanosheet can be produced via a solution based oriented attachment route.[67] A follow-up paper reported the subsequent fabrication of PbS nanosheet based FET device by spin-coating of the nanosheets suspension (in toluene) onto the SiO_2 coated Si substrate where highly n-doped Si served as the gate electrode, and a pair of gold electrodes were deposited onto the single PbS sheet as source and drain, shown in **Figure 1.12 (a)**.[80] This gold contacted PbS device has achieved a remarkable field-effect mobility of 0.417 $cm^2 V^{-1} s^{-1}$ (V_g = -5V, V_{DS} = 1V, T = 290K) with a p-type character. Moreover, the device performance is one of the best among the colloidal nanocrystals based FET without any chemical or thermal treatment, and further highlighted the advantage and potential for 2D nanosheet over spherical dots that are being used in optoelectronic devices. Secondly, in colloidal NCs based optical devices such as Lasers, 2D nanosheets are superior due to their large absorption cross-sections, slow Auger recombination rates, and the narrow emission line width. As depicted in the recent discovery reported by Guzelturk et al., they successfully observed the increment of optical gain from CdSe nanoplatelets core to CdSe/CdS core/crown structures with different CdS crown sizes (See **Figure 1.12(b)**).

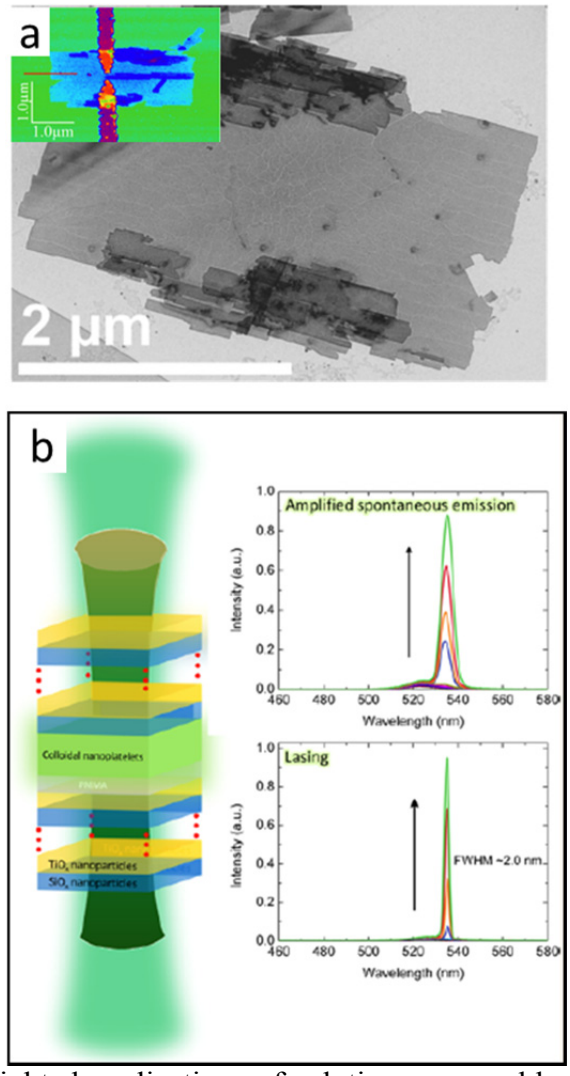

Figure 1.12 Highlighted applications of solution processable 2D nanosheets. (a) Low resolution TEM image of a single PbS nanosheet with the thickness of 5 to 6 nm and lateral size up to 2 to 3 μm, the left-top inset is the AFM image of two gold electrodes contacted with a single PbS nanosheet; (b) schematic drawing of the vertical cavity surface-emitting laser (VCSEL) of the ensemble nanoplatelets, the right-top graph is the two photon absorption pumped ASE of the 21 nm size core/crown nanoplatelets, while the right-bottom plot is the emission spectrum of the VCSEL as the pump intensity is progressively increased. Adapted with permission from Ref. 77, 80.

With the amplified spontaneous emission thresholds as low as 41 $\mu J/cm^2$ and 4.48 mJ/cm^2 for one- and two- photon absorption respectively, this thresholds became the best among the state-of-art colloidal NCs (eg. QDs, rods and tetrapods) based optical gain devices with similar emitting wavelength. The gain coefficient of these nanoplatelets was measured as 650 cm^{-1} with a 4-fold enhancement over the best reported gain coefficient of the

colloidal QDs. Such remarkable observation pointed out the possibility of 2D nanostructures as a great candidate for producing high-efficiency, solution-processed lasers.[77]

On the other hand, the Lithium ion battery has been considered as one of the top promising energy storage systems due to its high absolute potential against the standard hydrogen cell and its low atomic weight. Compared to the traditional bulk layered crystals such as graphite and metal dichalcogenides, 2D nanostructures are of great interest in such energy-storage devices, given its shortened paths for fast lithium ion diffusion and large exposed surface offering more lithium-insertion channels. In recent years, increasing efforts based on developing novel 2D nanosheets with various morphologies have led to impressively improved charge/discharge capacity, cycling performance and rate capability. The porous nanosheets were one of the attractive materials that have been utilized in lithium storage device due to their large exposed surface that allows short path for lithium insertion and open porous structures holding nanodrops of electrolyte which may reduce electrode polarization during fast lithium storage. [81, 82] Besides acting as the active layer, 2D nanosheets could also play an excellent role as the electrode material. For example ultrathin CuS nanosheets synthesized by Zhang's group via a organometallic soft template in solution has been used to fabricate the electrode for lithium-ion battery, which exhibits a large capacity and good cycling stability even after 360 cycles.[66]

1.4 Thesis Outline

In **Chapter 2**, we successfully synthesized colloidal InP/ZnS seeded CdS tetrapods by harnessing the structural stability of the InP/ZnS seed nanocrystals at the high reaction temperatures needed to grow the CdS arms.

Owing to an unexpected Type II band alignment at the interface of the InP/ZnS core and CdS arms which enhanced the occurrence of radiative excitonic recombination in CdS, these tetrapods were found to be capable of exhibiting highly efficient multiexcitonic dual wavelength emission of equal intensity at spectrally distinct wavelengths of ~ 485 nm and ~ 675 nm. Additionally, the Type II InP/ZnS seeded CdS tetrapods displayed a wider range of pump-dependent emission color-tunability (from red to white to blue) within the context of a CIE 1931 chromaticity diagram and possessed higher photostability due to suppressed multiexcitonic Auger recombination when compared to conventional Type I CdSe seeded CdS tetrapods. By employing time resolved spectroscopy measurements, we were able to attribute the wide emission color-tunability to the large valence band offset between InP and CdS. This work highlights the importance of band alignment in the synthetic design of semiconductor nanoheterostructures which can exhibit color-tunable multi-wavelength emission with high efficiency and photostability.

In **Chapter 3**, we exposed the red emitting type-II InP/CdS tetrapods to Ag^{+} resulted in the preservation of the InP core while the CdS arms underwent full cationic exchange to Ag_2S. Interestingly, subsequent exposure to Zn^{2+} allowed the formation of Type I InP/ZnS tetrapods with relatively strong fluorescence emission at ~530 nm. This approach provides a good opportunity for effective cation exchange of the shell while preserving the core material, which is not easily achieved for the II-VI based materials.

In **Chapter 4**, we further moved from 3D nanoheterostructures to two dimensional transition metal sulfides (TMS), because these wet chemically synthesized TMS are promising materials for catalysis, batteries and

optoelectronics. However a firm understanding on the chemical conditions which result in selective lateral growth has been lacking. As a result, we demonstrated that Ni_9S_8, which is a less common nonstoichiometric form of nickel sulfide, can exhibit two-dimensional growth when halide ions were present in the reaction. We show that the introduction of halide ions reduced the rate of formation of the nickel thiolate precursor, thereby inhibiting nucleation events and slowing growth kinetics such that sheet-like formation was favored. Structural characterization of the nanosheets produced revealed that they were single-crystal with lateral dimensions in the range of ~ 100 – 1000 nm and thicknesses as low as ~4 nm (about 3 unit cells). Varying the concentration of halide ions present in the reaction allowed for the shape of the nanostructures to be continuously tuned from particle- to sheet-like, thus offering a facile route to controlling their morphology. The synthetic methodology introduced was successfully extended to Cu_2S, which suggests that the importance of impeded growth kinetics in the formation of nanosheets may be applicable to a wide variety of TMS.

In **chapter 5**, we adopted the as synthesized Cu_2S nanosheets (introduced in **Chapter 4**) as the starting material to carry out Pb^{2+} exchange reaction for obtaining PbS nanosheets. The unique advantage of cation exchange allowed us to achieve a novel facet orientation in cubic face-centered PbS nanosheet where the high energy {111} facet terminated both top and bottom of the lateral plane of nanosheets leaving relatively lower energetic {110} and {100} facets to appear on the side (corners and edges). With the wet chemical synthetic environment with excess oleic acid, the {111} facets could be possibly terminated by Pb atoms only, giving a Pb-rich surface

and eventually retaining n-type behaviour in field effect transistor. This unique Pb-rich PbS nanosheet would show promise for achieving n-type material that can stabilize itself under ambient air and possess excellent FET performance**.**

1.5 References

1. Yin, Y.; Alivisatos, A. P., *Nature* **2005,** 437, 664.

2. El-Sayed, M. A., *Accounts Chem. Res.* **2004,** 37, 326.

3. Murray, C. B.; Norris, D. J.; Bawendi, M. G., *J. Am. Chem. Soc.* **1993,** 115, 8706.

4. Lin, S. L.; Pradhan, N.; Wang, Y. J.; Peng, X. G., *Nano Lett.* **2004,** 4, 2261.

5. Du, Y. P.; Xu, B.; Fu, T.; Cai, M.; Li, F.; Zhang, Y.; Wang, Q. B., *J. Am. Chem. Soc.* **2010,** 132, 1470.

6. Pejova, B.; Bineva, I., *J. Phys. Chem. C* **2013,** 117, 7303.

7. Xu, S.; Kumar, S.; Nann, T., *J. Am. Chem. Soc.* **2006,** 128, 1054.

8. Battaglia, D.; Peng, X. G., *Nano Lett.* **2002,** 2, 1027.

9. Hines, M. A.; Scholes, G. D., *Adv. Mater.* **2003,** 15, 1844.

10. Amelia, M.; Lincheneau, C.; Silvi, S.; Credi, A., *Chem. Soc. Rev.* **2012,** 41, 5728.

11. Coe, S.; Woo, W. K.; Bawendi, M.; Bulovic, V., *Nature* **2002,** 420, 800.

12. Gur, I.; Fromer, N. A.; Geier, M. L.; Alivisatos, A. P., *Science* **2005,** 310, 462.

13. Konstantatos, G.; Sargent, E. H., *Nat. Nanotechnol.* **2010,** 5, 391.

14. Koh, W. K.; Saudari, S. R.; Fafarman, A. T.; Kagan, C. R.; Murray, C. B., *Nano Lett.* **2011,** 11, 4764.

15. Michalet, X.; Pinaud, F. F.; Bentolila, L. A.; Tsay, J. M.; Doose, S.; Li, J. J.; Sundaresan, G.; Wu, A. M.; Gambhir, S. S.; Weiss, S., *Science* **2005,** 307, 538.

16. Biju, V.; Itoh, T.; Ishikawa, M., *Chem. Soc. Rev.* **2010,** 39, 3031.

17. Smith, A. M.; Nie, S. M., *Accounts Chem. Res.* **2010,** 43, 190.

18. Choi, C. L.; Alivisatos, A. P., In *Annu. Rev. Phys. Chem.*, Annual Reviews: Palo Alto, **2010**; Vol. 61, pp 369.

19. Guzelian, A. A.; Katari, J. E. B.; Kadavanich, A. V.; Banin, U.; Hamad, K.; Juban, E.; Alivisatos, A. P.; Wolters, R. H.; Arnold, C. C.; Heath, J. R., *J. Phys. Chem.* **1996,** 100, 7212.

20. Xie, R.; Battaglia, D.; Peng, X., *J. Am. Chem. Soc.* **2007,** 129, 15432.

21. Didchenko, R.; Alix, J. E.; Toeniskoetter, R. H., *J. Inorg. Nucl. Chem.* **1960,** 14, 35.

22. Micic, O. I.; Curtis, C. J.; Jones, K. M.; Sprague, J. R.; Nozik, A. J., *J. Phys. Chem.* **1994,** 98, 4966.

23. Battaglia, D.; Peng, X. G., *Nano Lett.* **2002,** 2, 1027.

24. Xu, S.; Ziegler, J.; Nann, T., *J. Mater. Chem.* **2008,** 18, 2653.

25. Donega, C. D., *Chem. Soc. Rev.* **2010,** 40, 1512.

26. Wei, S. H.; Zunger, A., *Appl. Phys. Lett.* **1998,** 72, 2011.

27. Reiss, P.; Protiere, M.; Li, L., *Small* **2009,** 5, 154.

28. Hines, M. A.; Guyot-Sionnest, P., *J. Phys. Chem.* **1996,** 100, 468.

29. Li, J. J.; Wang, Y. A.; Guo, W. Z.; Keay, J. C.; Mishima, T. D.; Johnson, M. B.; Peng, X. G., *J. Am. Chem. Soc.* **2003,** 125, 12567.

30. Allen, P. M.; Walker, B. J.; Bawendi, M. G., *Angew. Chem.-Int. Edit.* **2010,** 49, 760.

31. Talapin, D. V.; Gaponik, N.; Borchert, H.; Rogach, A. L.; Haase, M.; Weller, H., *J. Phys. Chem. B* **2002,** 106, 12659.

32. Li, J. J.; Wang, Y. A.; Guo, W. Z.; Keay, J. C.; Mishima, T. D.; Johnson, M. B.; Peng, X. G., *J. Am. Chem. Soc.* **2003,** 125, 12567.

33. Li, L.; Reiss, P., *J. Am. Chem. Soc.* **2008,** 130, 11588.

34. Kim, T.; Kim, S. W.; Kang, M., *J. Phys. Chem. Lett.* **2012,** 3, 214.

35. Kim, S.; Kim, T.; Kang, M.; Kwak, S. K.; Yoo, T. W.; Park, L. S.; Yang, I.; Hwang, S.; Lee, J. E.; Kim, S. K.; Kim, S. W., *J. Am. Chem. Soc.* **2012,** 134, 3804.

36. Kim, S.; Park, J.; Kim, T.; Jang, E.; Jun, S.; Jang, H.; Kim, B.; Kim, S. W., *Small* **2011,** 7, 70.

37. Yang, X. Y.; Zhao, D. W.; Leck, K. S.; Tan, S. T.; Tang, Y. X.; Zhao, J. L.; Demir, H. V.; Sun, X. W., *Adv. Mater.* **2012,** 24, 4180.

38. Yong, K. T.; Ding, H.; Roy, I.; Law, W. C.; Bergey, E. J.; Maitra, A.; Prasad, P. N., *ACS Nano* **2009,** 3, 502.

39. Carbone, L.; Nobile, C.; De Giorgi, M.; Sala, F. D.; Morello, G.; Pompa, P.; Hytch, M.; Snoeck, E.; Fiore, A.; Franchini, I. R.; Nadasan, M.; Silvestre, A. F.; Chiodo, L.; Kudera, S.; Cingolani, R.; Krahne, R.; Manna, L., *Nano Lett.* **2007,** 7, 2942.

40. Talapin, D. V.; Nelson, J. H.; Shevchenko, E. V.; Aloni, S.; Sadtler, B.; Alivisatos, A. P., *Nano Lett.* **2007,** 7, 2951.

41. Deka, S.; Miszta, K.; Dorfs, D.; Genovese, A.; Bertoni, G.; Manna, L., *Nano Lett.* **2010,** 10, 3770.

42. Kim, T. H.; Cho, K. S.; Lee, E. K.; Lee, S. J.; Chae, J.; Kim, J. W.; Kim, D. H.; Kwon, J. Y.; Amaratunga, G.; Lee, S. Y.; Choi, B. L.; Kuk, Y.; Kim, J. M.; Kim, K., *Nat. Photonics* **2011,** 5, 176.

43. Wong, J. I.; Mishra, N.; Xing, G. C.; Li, M. J.; Chakrabortty, S.; Sum, T. C.; Shi, Y. M.; Chan, Y. T.; Yang, H. Y., *ACS Nano* **2014,** 8, 2873.

44. Wang, T.; Zhuang, J. Q.; Lynch, J.; Chen, O.; Wang, Z. L.; Wang, X. R.; LaMontagne, D.; Wu, H. M.; Wang, Z. W.; Cao, Y. C., *Science* **2012,** 338, 358.

45. Kim, S.; Fisher, B.; Eisler, H. Y.; Bawendi, M. G., *J. Am. Chem. Soc.* **2003,** 125, 11466.

46. Nemchinov, A.; Kirsanova, M.; Hewa-Kasakarage, N. N.; Zamkov, M., *J. Phys. Chem. C* **2008,** 112, 9301.

47. Dennis, A. M.; Mangum, B. D.; Piryatinski, A.; Park, Y. S.; Hannah, D. C.; Casson, J. L.; Williams, D. J.; Schaller, R. D.; Htoon, H.; Hollingsworth, J. A., *Nano Letters* **2012,** 12, 5545.

48. Xie, R. G.; Zhong, X. H.; Basche, T., *Adv. Mater.* **2005,** 17, 2741.

49. Lo, S. S.; Mirkovic, T.; Chuang, C. H.; Burda, C.; Scholes, G. D., *Adv. Mater.* **2011,** 23, 180.

50. Saruyama, M.; So, Y. G.; Kimoto, K.; Taguchi, S.; Kanemitsu, Y.; Teranishi, T., *J. Am. Chem. Soc.* **2011,** 133, 17598.

51. Rivest, J. B.; Swisher, S. L.; Fong, L. K.; Zheng, H. M.; Alivisatos, A. P., *ACS Nano* **2011,** 5, 3811.

52. Smith, A. M.; Nie, S. M., *Accounts Chem. Res.* **2010,** 43, 190.

53. Xie, R. G.; Kolb, U.; Basche, T., *Small* **2006,** 2, 1454.

54. Hewa-Kasakarage, N. N.; El-Khoury, P. Z.; Schmall, N.; Kirsanova, M.; Nemchinov, A.; Tarnovsky, A. N.; Bezryadin, A.; Zamkov, M., *Appl. Phys. Lett.* **2009,** 94, 133113.

55. Milliron, D. J.; Hughes, S. M.; Cui, Y.; Manna, L.; Li, J. B.; Wang, L. W.; Alivisatos, A. P., *Nature* **2004,** 430, 190.

56. Halpert, J. E.; Porter, V. J.; Zimmer, J. P.; Bawendi, M. G., *J. Am. Chem. Soc.* **2006,** 128, 12590.

57. Teranishi, T.; Sakamoto, M., *J. Phys. Chem. Lett.* **2013,** 4, 2867.

58. Talapin, D. V.; Lee, J. S.; Kovalenko, M. V.; Shevchenko, E. V., *Chem. Rev.* **2010,** 110, 389.

59. Tong, S. W.; Mishra, N.; Su, C. L.; Nalla, V.; Wu, W. Y.; Ji, W.; Zhang, J.; Chan, Y.; Loh, K. P., *Adv. Funct. Mater.* **2014,** 24, 1904.

60. Hu, S.; Wang, X., *Chem. Soc. Rev.* **2013,** 42, 5577.

61. Bouet, C.; Tessier, M. D.; Ithurria, S.; Mahler, B.; Nadal, B.; Dubertret, B., *Chem. Mat.* **2013,** 25, 1262.

62. Park, K. H.; Jang, K.; Son, S. U., *Angew. Chem.-Int. Edit.* **2006,** 45, 4608.

63. Vaughn, D. D.; In, S. I.; Schaak, R. E., *ACS Nano* **2011,** 5, 8852.

64. Son, J. S.; Wen, X. D.; Joo, J.; Chae, J.; Baek, S. I.; Park, K.; Kim, J. H.; An, K.; Yu, J. H.; Kwon, S. G.; Choi, S. H.; Wang, Z. W.; Kim, Y. W.; Kuk, Y.; Hoffmann, R.; Hyeon, T., *Angew. Chem.-Int. Edit.* **2009,** 48, 6861.

65. Kirkeminde, A.; Ruzicka, B. A.; Wang, R.; Puna, S.; Zhao, H.; Ren, S. Q., *ACS Appl. Mater. Interfaces* **2012,** 4, 1174.

66. Du, Y. P.; Yin, Z. Y.; Zhu, J. X.; Huang, X.; Wu, X. J.; Zeng, Z. Y.; Yan, Q. Y.; Zhang, H., *Nat. Commun.* **2012,** 3, 1177.

67. Schliehe, C.; Juarez, B. H.; Pelletier, M.; Jander, S.; Greshnykh, D.; Nagel, M.; Meyer, A.; Foerster, S.; Kornowski, A.; Klinke, C.; Weller, H., *Science* **2010,** 329, 550.

68. Coleman, J. N.; Lotya, M.; O'Neill, A.; Bergin, S. D.; King, P. J.; Khan, U.; Young, K.; Gaucher, A.; De, S.; Smith, R. J.; Shvets, I. V.; Arora, S. K.; Stanton, G.; Kim, H. Y.; Lee, K.; Kim, G. T.; Duesberg, G. S.; Hallam, T.; Boland, J. J.; Wang, J. J.; Donegan, J. F.; Grunlan, J. C.; Moriarty, G.; Shmeliov, A.; Nicholls, R. J.; Perkins, J. M.; Grieveson, E. M.; Theuwissen, K.; McComb, D. W.; Nellist, P. D.; Nicolosi, V., *Science* **2011,** 331, 568.

69. Chou, S. S.; De, M.; Kim, J.; Byun, S.; Dykstra, C.; Yu, J.; Huang, J. X.; Dravid, V. P., *J. Am. Chem. Soc.* **2013,** 135, 4584.

70. Tang, Z. Y.; Zhang, Z. L.; Wang, Y.; Glotzer, S. C.; Kotov, N. A., *Science* **2006,** 314, 274.

71. Joo, J.; Son, J. S.; Kwon, S. G.; Yu, J. H.; Hyeon, T., *J. Am. Chem. Soc.* **2006,** 128, 5632.

72. Ithurria, S.; Dubertret, B., *J. Am. Chem. Soc.* **2008,** 130, 16504.

73. Ithurria, S.; Tessier, M. D.; Mahler, B.; Lobo, R.; Dubertret, B.; Efros, A., *Nat. Mater.* **2011,** 10, 936.

74. Li, Z.; Peng, X. G., *J. Am. Chem. Soc.* **2011,** 133, 6578.

75. Li, L.; Chen, Z.; Hu, Y.; Wang, X. W.; Zhang, T.; Chen, W.; Wang, Q. B., *J. Am. Chem. Soc.* **2013,** 135, 1213.

76. Acharya, S.; Das, B.; Thupakula, U.; Ariga, K.; Sarma, D. D.; Israelachvili, J.; Golan, Y., *Nano Lett.* **2013,** 13, 409.

77. Guzelturk, B.; Kelestemur, Y.; Olutas, M.; Delikanli, S.; Demir, H. V., *ACS Nano* **2014**, 8, 6599.

78. Chhowalla, M.; Shin, H. S.; Eda, G.; Li, L. J.; Loh, K. P.; Zhang, H., *Nat. Chem.* **2013,** 5, 263.

79. Hsu, S. W.; On, K.; Tao, A. R., *J. Am. Chem. Soc.* **2011,** 133, 19072.

80. Dogan, S.; Bielewicz, T.; Cai, Y. X.; Klinke, C., *Appl. Phys. Lett.* **2012,** 101, 073102.

81. Liu, J. H.; Liu, X. W., *Adv. Mater.* **2012,** 24, 4097.

82. Liu, J. H.; Liu, X. W., *Energy Environ. Sci.* **2014***,* **7**, 2608.

CHAPTER 2

Efficient Color-Tunable Multiexcitonic Dual Wavelength Emission from Type II Semiconductor Tetrapods

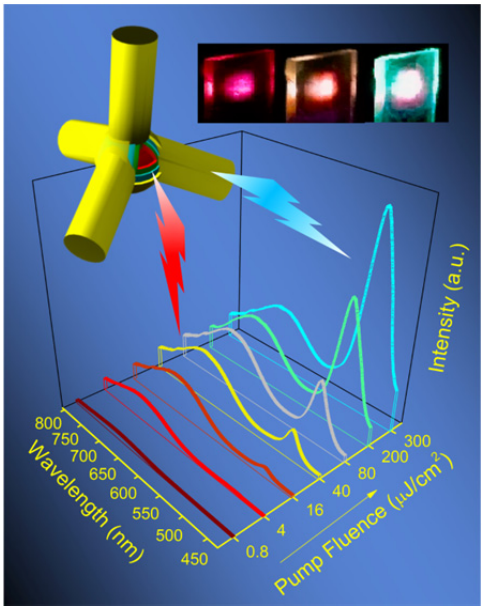

2.1 Introduction

Multi-wavelength multiexciton emission (MME) in strongly quantum confined semiconductor nanoparticles may be broadly defined as a process in which excitons of different energies radiatively recombine within the same nanoparticle to give spectrally distinct emission wavelengths. This can be attractive for applications in which more than one emission color is desirable, such as multiplexed fluorescence labeling schemes[1-5] or ratiometric sensing in which the ratio of emission intensities of at least two resolvable wavelengths provides a means of quantifying changes in the chemical environment.[6-9] Unlike typical multi-wavelength emitting nanoparticle-dye or nanoparticle-nanoparticle conjugates which suffer from a statistical distribution of stoichiometries between each type of chromophore in the conjugate, the different wavelengths of emission in the MME process originate from the same nanoparticle, thereby offering the possibility of quantitative ratiometric sensing at the single particle level. Additionally, where the integrated emission intensities of the different wavelengths differ as the excitation fluence is changed, MME offers a convenient means to dynamically modify the overall color of emission (as perceived by eye) from the nanoparticles by simply varying the pump intensity. It is therefore desirable to develop an architecture in which MME can be produced efficiently and with wide pump-dependent color tunability.

One method for achieving MME is via the use of heterostructured semiconductor nanoparticles such as CdSe seeded CdS tetrapods, where it was previously shown by Lutich et. al. that saturating the CdSe core with excitons results in an “exciton-blocking” effect in which excitons generated in the CdS

arms do not localize into the CdSe core but instead undergo radiative recombination. This yields steady-state PL at red and blue wavelengths from both the CdSe core and CdS arms respectively, and it was shown that ~ 55 nm long CdS arms were required to achieve effective spatial separation of the CdS exciton from the CdSe core. Attaining equally intense emission for both core and arms in these quasi Type II semiconductor nanoheterostructures, however, required relatively high pump fluence.[10] Recent work on CdSe/CdS dot-in-a-bulk structures showed that dual emission from CdSe and CdS can be obtained at much lower pump intensities, but with limited size-dependent wavelength tunability from its bulk-like CdS shell.[11] In this work we describe a novel InP/ZnS seeded CdS tetrapod (tpod) which by virtue of its Type II alignment and large valence band offset between the core and arms allowed for efficient dual wavelength emission to be achieved with wider pump-dependent emission color tunability than its Type I CdSe seeded CdS counterpart. These results highlight the importance of band alignment in achieving MME in colloidal semiconductor nanostructures.

2.2 Experimental section

2.2.1 Chemicals and materials

Myristic acid (MA, 99 %), tris(methylsilyl) phosphine ($P(TMS)_3$,95%), 1-octadecene (ODE, 90%), zinc acetate ($Zn(Ac)_2$, 99%), 1-dodecanethiol (DDT, 97%), cadmium oxide (CdO, 99.5%), sulphur (S, reagent grade), were purchased from Sigma Aldrich. Indium acetate ($In(Ac)_3$, 99.99%), Trioctylphosphine (TOP, 97%), were purchased from Alfa Aesar. n-octadecylphosphonic acid (ODPA, 97%), trioctylphosphine oxide (TOPO,

99%) and n-hexylphosphonic acid (HPA, 97%) were purchased from Strem. All the chemicals were used as received without further purification. Unless stated otherwise, all the reactions were conducted in oven-dried glassware under nitrogen atmosphere using standard Schlenk techniques.

2.2.2 Synthetic details

Synthesis of InP/ZnS seeds

The synthesis of InP/ZnS nanocrystals (NCs) was carried out based on a procedure previously reported by Peter Reiss et al.[12] but with slight modifications. Briefly, 0.2 mmol of $In(Ac)_3$, 0.6 mmol of MA and 8 mL of ODE were degassed at 100 ℃ for 1 hour in a 3-neck round bottom flask and then cooled down to room temperature under N_2. 0.2 mmol $Zn(Ac)_2$ and 0.2 mmol of DDT were then added to the flask, evacuated and purged with N_2 three times. Finally, 0.2 mmol of $P(TMS)_3$ in 1 mL ODE was injected into the reaction pot at 40 ℃, and the overall mixture was rapidly heated to 300 ℃ (within ~ 10 mins) and kept at 300 ℃ for 1-1.5 hours to grow the InP/ZnS NCs.

Further coating of InP/ZnS seed with additional ZnS

After the formation of the InP/ZnS seeds, the reaction flask was cooled to room temperature and 0.2 mmol of $Zn(Ac)_2$ powder was added. The mixture was then heated to 230 ℃, and maintained at this temperature for ~3 hrs. 0.1 mmol of DDT was then injected dropwise to the reaction mixture under vigorous stirring. The reaction mixture was subsequently allowed to anneal at 240-250 ℃ for ~0.5 – 1 hour and at 300 ℃ for ~20 min.

To isolate the NCs, the reaction mixture was cooled to room temperature and 14 equivalents of acetone was added (which caused precipitation of the NCs), followed by centrifugation at 3900 rpm for 15 min. The nanocrystal precipitate was then purified via 2 cycles of re-dispersion in hexane and precipitation in a stock solution of methanol/ethanol/isopropanol (in a 1:1:1 volume ratio). The purified InP/ZnS NCs were readily dispersed in hexane and used as seeds for the growth of tetrapods.

Synthesis of InP/ZnS seeded CdS tetrapods

The synthesis of InP/ZnS seeded CdS tetrapods follows the procedure introduced by Manna et al. for ZnSe seeded CdS tetrapods.[13] TOPO (3.0 g), ODPA (0.29 g), HPA (0.08 g) and CdO (0.065 g) were mixed in a 50 mL reaction flask and degassed at 150 ℃ for two hours. After degassing, the temperature was increased to 360 ℃ under N_2 to yield a clear colorless solution. At this point, 1.8 mL of TOP (97%) was injected into the pot, and the temperature was allowed to recover to 360 ℃. An injection mixture comprising of S powder dissolved in 1.8 mL TOP (97%) and 10 nmol InP/ZnS seeds was rapidly injected into the reaction flask, upon which the temperature in the flask dropped to 300 ℃. The reaction temperature was recovered to 360 ℃ and maintained at this growth temperature for about 3 min. The final products were then purified via 2 cycles of re-dispersion in toluene and precipitation in methanol.

Synthesis of InP/ZnS/CdS core/shell spheres

The procedure is the same as that of InP/ZnS seeded CdS tetrapods described in the above paragraph, with the sole exception that the injection and growth temperature employed was 300 ℃ instead.

2.2.3 Characterizations

Structural characterization

Transmition Electron Microscopy (TEM)

A JEOL JEM 1220F (100 kV accelerating voltage) microscope was used to obtain bright field TEM images of the nanoparticles. For TEM sample preparation, a drop of the nanoparticle solution was placed onto a 300 mesh size copper grid covered with a continuous carbon film. Excess solution was removed by an adsorbent paper and the sample was dried at room temperature. The High-Resolution TEM images and detailed elemental analysis were carried out on a FEI Titan 80-300 electron microscope operated at 200 KV, which is equipped with an electron beam monochromator, an energy dispersive X-ray spectroscopy (EDX) and a Gatan electron energy loss spectrometer. The probing electron beam size for the EDX measurement was around 0.3 nm. The dwell time for each EDX spectrum is 10s.

X-Ray Diffraction (XRD)

XRD data was obtained with a diffractometer (Bruker AXS, GADDS) using Cu-Kα radiation (λ=1.540598Å) in the range of 20˚ to 100˚. Samples were prepared on a clean silicon wafer by placing drops of concentrated silica coated nanoparticles in hexane on the silicon surface and dried at 60 ℃ in the oven. This was repeated several times until a thin layer of solid was formed on the silicon substrate.

Optical characterization

Absorption spectra were obtained with an Agilent 8453 UV-Visible spectrophotometer in UV-visible range. Photoluminescence (PL) spectra in visible region and NIR region were collected with a spectrofluorophotometer

and HORIBA Jobin Yvon Fluorolog 3 spectrometer equipped with liquid nitrogen cooled InGaAs photodiode detector respectively. Time-resolved fluorescence data were obtained by using a NanoLED pulsed laser diode excitation source and a HORIBA Jobin Yvon TCSPC detection system FluoroHub. Care was taken to ensure that the concentrations of the core and core-seeded nanostructures were sufficiently dilute to avoid contributions from re-absorption or energy transfer. Absolute quantum yield measurement of the type II nanocrystals has been carried out by Hamamatsu Quantaurus-QY with NIR model (C11347-12) which is suitable for measurements from 400 nm to 1100 nm.

The femtosecond laser source for the following optical measurements was a Coherent Legend Ti:Sapphire regenerative amplifier (150 fs, 1 kHz, 800 nm) seeded by a Coherent Vitesse oscillator (100 fs, 80 MHz). For the pump-fluence-dependent PL measurements, the solution samples in the 2 mm thick quartz cells were excited using 400 nm excitation pulses obtained by using a BBO doubling crystal. The time-integrated PL spectra were collected in a conventional backscattering geometry and detected by a charge-coupled device array (Princeton Instruments, Pixis 400B) coupled to a monochromator (Acton, Spectra Pro 2500i).

For pump-probe measurements, the solution samples in quartz cells were pumped by the 400 nm pulses which were focused onto a 200 μm spot and overlapped with white-light continuum probe pulses generated with a 1 mm thick sapphire plate (that was focused by a parabolic mirror to a spot of ~20 μm diameter). The differential transmission (ΔT/T) spectra of the samples were performed in a non-degenerate pump-probe configuration with chirp-

correction, where $\Delta T/T = (T - T_0)/T_0$ (where T_0 is the transmission of probe beam without pump excitation of the sample, *T* is transmission of probe beam with pump excitation of the sample). The linear polarization of the pump pulse was adjusted to be perpendicular to that of the probe pulse with a polarizer and a half-wave plate. The cross-polarization will help eliminate any contribution from coherent artifacts at early times. Pump-induced changes $\Delta T/T$ were monitored using a monochromator/PMT configuration coupled to a lock-in amplifier. The pump beam was chopped at 83 Hz and used as the reference frequency for the lock-in amplifier.

2.3 Results and discussions

The formation of monodispersed colloidal tetrapods based on II-VI semiconductors such as CdTe and CdSe via a seeded approach critically requires that the seeds possess a zinc blende (zb) or sphalerite crystal structure which provides four out of eight {111} crystal facets to support the growth of the tetrapod arms.[13-15] Given that the crystal structure of InP fabricated at moderate reaction temperatures of below ~ 360 ℃ is typically that of zinc blende,[16] it is expected that colloidal InP particles should be able to serve as seeds for the heterogeneous nucleation and growth of CdS arms to yield III-V / II-VI tetrapod nanostructures with unique physicochemical properties. Our initial attempts to utilize the bare InP particles as seeds for the growth of CdS tetrapod arms, however, resulted in the severe structural degradation of InP at the high reaction temperatures required. This was overcome by the use of ZnS coated InP QDs synthesized via a single pot approach. In this procedure, a mixture of In, P, Zn, and S precursors were heated up to a temperature of between 240-300 ℃ for ~ 1.5 hours in a reaction flask containing octadecene

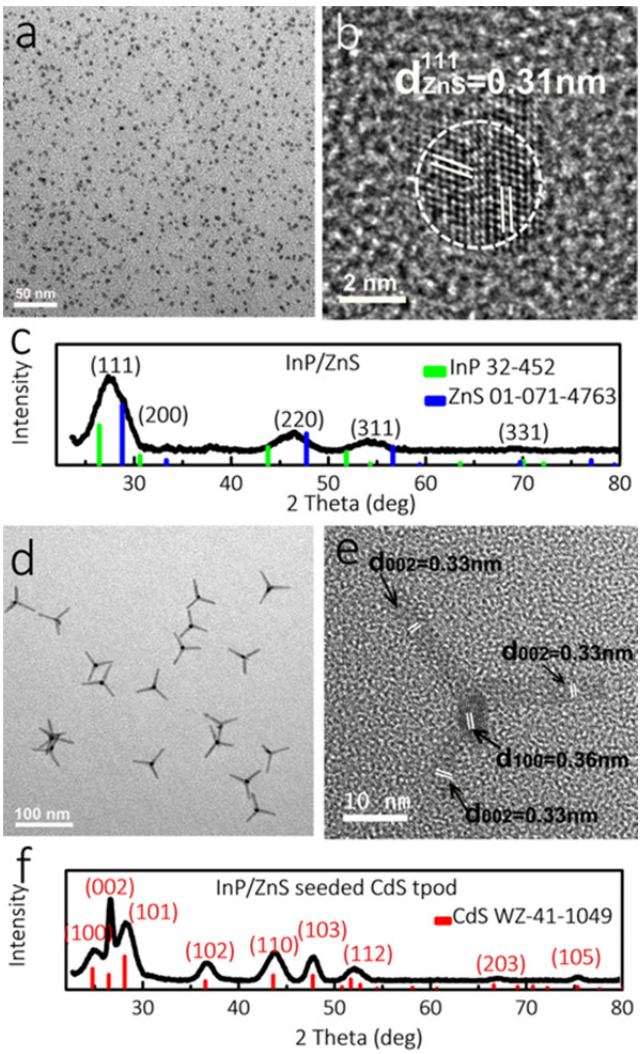

Figure 2.1 Structural characterization of InP/ZnS seed and InP/ZnS seeded CdS tetrapod. (a) TEM image of as synthesized InP/ZnS cores with an average diameter of ~3 nm; (b) HRTEM image of a typical core showing lattice fringes with a d-spacing corresponding to the (111) plane of ZnS; (c) Powder XRD spectrum of InP/ZnS showing peaks in-between those of standard reference zb-InP and zb-ZnS; (d) TEM image of InP/ZnS seeded CdS tetrapods with an average arm length of ~27 nm and mean diameter of ~5 nm; (e) HRTEM image of a single tetrapod showing lattice fringes of the (100) and (002) planes corresponding to CdS; (f) Powder XRD spectrum of InP/ZnS seeded CdS tetrapods showing the peaks of CdS wurtzite.

(ODE) as the solvent and myristic acid as the capping group. This resulted in an alloyed InZnP interfacial layer between the InP core and a thin outermost ZnS shell, as previously characterized by Reiss et al.[17, 18] A second ZnS shell was grown onto the as-synthesized nanocrystals mentioned above in a one-pot fashion by re-introducing the Zn and S precursors followed by annealing at

250 ℃ for ~ 30 mins. This was found to be necessary to achieve better surface crystallinity to support the growth of CdS arms. **Figure 2.1(a)** is a typical transmission electron microscope (TEM) image of the InP/ZnS nanoparticles produced, where the average particle diameter is ~3 nm with a size dispersity of ~9%. These particles were then used as cores to support the growth of CdS. Briefly, the InP/ZnS particles were mixed with trioctylphosphine sulfide (TOPS) and injected swiftly into a cadmium precursor containing a mixture of n-trioctylphosphine oxide (TOPO), n-octadecylphosphonic acid (ODPA) and n-hexylphosphonic acid at a temperature of ~350 ℃. This resulted in uniform InP/ZnS seeded CdS tetrapod structures with CdS arm dimensions of ~ 5.2 nm and ~ 28.5 nm in length, as exemplified in **Figure 2.1(d)**. Analogous to the seeded growth of CdSe/CdS tetrapods, the use of ODPA and HPA as surfactants was found to be critical for tetrapod arm growth in our system.[15]

Structural characterization of the as-synthesized InP/ZnS cores and InP/ZnS seeded CdS tetrapods proceeded via high resolution transmission electron microscopy (HRTEM) and powder X-ray diffraction (XRD) measurements, which are summarized in **Figure 2.1(b)**, **(e)** and **2.1(c)**, **(f)** respectively. The XRD spectra of the InP/ZnS seeds revealed three major peaks that lie in between those corresponding to the (111), (220) and (311) facets of zb-InP and zb-ZnS, which is consistent with a InP/ZnS core-shell structure.[16] This is further supported by the HRTEM image in **Figure 2.1(b)**, which shows the zb-ZnS lattice fringes of its (111) plane. The exposed cubic zinc blende ±{111} facets of ZnS are atomically similar to the ±{001} facets of hexagonal (wurtzite) CdS,[19] and can therefore support growth of the CdS arms. The XRD data obtained for the InP/ZnS seeded CdS tetrapods showed a

dominance of peaks corresponding to that of w-CdS, which may be attributed to the fact that the four CdS arms account for most of the material comprising each tetrapod. The HRTEM image of a single tetrapod, as illustrated in **Figure 2.1(e)**, shows that the extension of the CdS arms (fast growth) occurs along the (002) plane while increase in the arm diameter takes place along the (100) plane, which is a slow growth facet due to strongly binding alkyl phosphonic acids.[14]

In order to ascertain their materials composition, High-angle Annular Dark-Field Imaging Scanning TEM (HAADF-STEM) analysis was performed on individual tetrapods, as depicted in **Figure 2.2(a)**. Point Energy-Dispersive X-ray Spectroscopy (EDX) measurements at the central region of tetrapod, as delineated in **Figure 2.2(b)**,

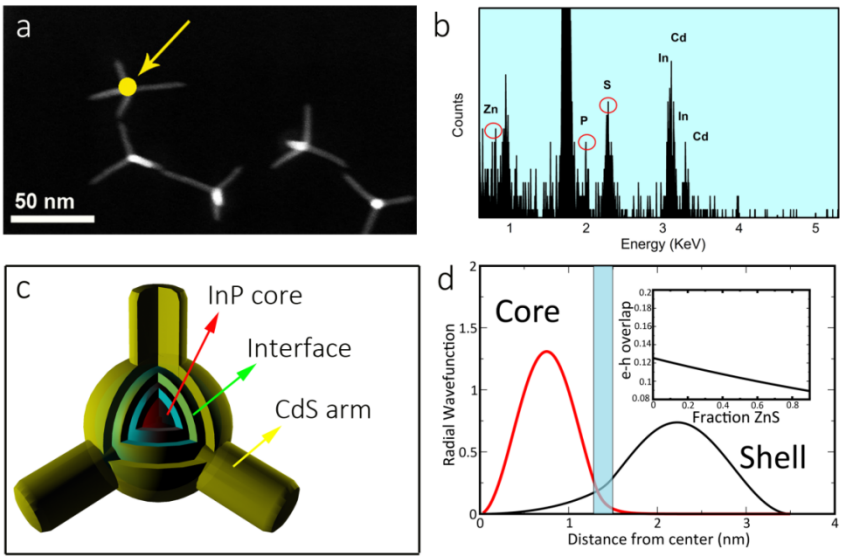

Figure 2.2 Components at the core/arm interface. (a) HAADF-STEM image of InP/ZnS seeded CdS tetrapods; (b) Point EDX probing the center of a single tetrapod (yellow dot in (a)), revealing signals attributed to Cd, S, In, P and Zn; (c) Cartoon depicting the structure and composition of a InP/ZnS seeded CdS tetrapod; (d) e and h wavefunctions for a core-shell InP/CdS nanocrystal with an intermediate interlayer. The inset shows the overlap as a function of interlayer composition with respect to ZnS.

yielded a low intensity of Zn, In and P, along with comparatively strong signals from Cd and S. The Zn signal obtained using point EDX at the core region was relatively weak but was observed more prominently in area EDX, suggesting that diffusion of Zn into the CdS arms at the high reaction temperature used (as previously shown in thin film studies[20]) had occurred. This would result in a graded $Zn_xCd_{1-x}S$ core-to-arm transition, and would leave little Zn at the branch point as confirmed by point EDX analysis.

The band alignment between bulk InP and CdS is Type II, where the bands are staggered. Excitons at the InP/CdS interface are expected to exhibit spatial separation of the electron and hole wavefunctions: the electron is localized to CdS while the hole is confined to InP.[21] However, in our InP/ZnS seeded CdS tetrapods, the interface between the InP core and CdS arms is most likely composed of an alloy of $In_yZn_{1-y}P$ and $Zn_xCd_{1-x}S$ as inferred from our structural characterization data. The consequences of the interphase structure are not immediately obvious. While InP/CdS has a Type II alignment, ZnS has a Type I (straddling) alignment with both InP and CdS. **Figure 2.2(c)** is a cartoon depiction of the complex structural composition of a InP/ZnS seeded CdS tetrapod where we illustrated both the graded $In_yZn_{1-y}P$ layer between the InP core and ZnS shell and the $Zn_xCd_{1-x}S$ layer at the seed / arm interface. To develop an intuitive understanding of the role of an alloyed Type I interlayer on the bound states of a Type II system, we considered a simplified model. We analyzed a spherical, core-shell nanocrystal with an alloyed interlayer using an effective mass approximation.[22] For simplicity, the hole and electron effective masses were assumed to be $m_h^* = 0.2m_0$ and $m_e^* = 0.6m_0$ in all phases. The band offsets of zb-ZnS relative to w-CdS were

taken from reference bulk values as $\Delta U_e^{\mathrm{ZnS/CdS}} = 0.70$ eV and $\Delta U_h^{\mathrm{ZnS/CdS}} = 0.40$ for electrons and holes respectively.[23] We simulated the alloy nature of the interlayer by taking the offset of the interlayer to be proportional to the Zn content, x. The band offsets of the InP relative to the CdS were taken to be $\Delta U_e^{\mathrm{InP/CdS}} = -0.394$ eV and $\Delta U_h^{\mathrm{InP/CdS}} = 1.25$.[21] We calculated the ground state (n=1) electron and hole wavefunctions numerically for various nanocrystal geometries. Our analysis lead us to conclude that the electron and hole ground state wavefunction overlap was very small and that the maximal overlap was at the interface. This is consistent with a Type II structure in which recombination occurs at the interface. The e-h overlap decreases as the height of the barrier increases, indicating that a thin Type I barrier should not interfere with charge separation. Consequently, it may be expected that the tetrapod effectively possess a Type II alignment between its core and arms.

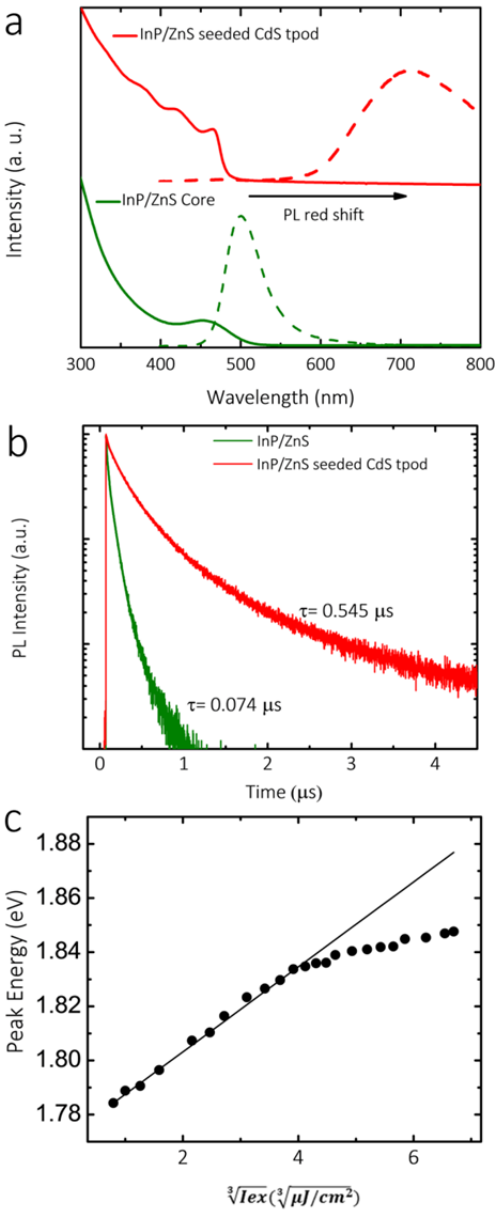

Figure 2.3 UV, PL and lifetime measurement. (a) Normalized PL (dashed lines) and UV-vis spectra (solid lines) of InP/ZnS QDs, and InP/ZnS-CdS tetrapods; (b) Normalized PL decay dynamics of two samples. The pump fluence is 5 μJ/cm2. (c) Pump fluence dependent emission band position of InP/ZnS-CdS tetrapods.

Optical characterization of the InP/ZnS seeded CdS tetrapods via absorption and PL spectrophotometry, as illustrated in **Figure 2.3(a)**, showed that growth of the CdS arms resulted in a CdS-dominated absorption spectrum and yielded a large emission redshift of ~ 200 nm with respect to the original InP/ZnS core (excited at 400 nm). The emission redshift was commensurate

with an increase in the length of the CdS arms (which is inferred from comparing with core-shell InP/ZnS/CdS NCs with the structural and optical characterizations described in the **Figure 2.4**), indicating that the observed PL was not due to deep trap emission from CdS. The absolute QY of the tetrapods at an excitation wavelength of 400 nm was determined to be ~ 20%, which is reasonable if one considers that the electron wavefunction is delocalized into four CdS arms which are not themselves passivated by an inorganic shell. Time-resolved PL measurements on the InP/ZnS seeds as depicted in **Figure 2.3(b)** revealed a fluorescence lifetime of ~ 74 ns, whereas that of InP/ZnS seeded CdS tetrapods showed a dramatically prolonged lifetime of ~ 545 ns. These observations collectively support the notion that the tetrapods possess a Type II alignment between the core and arms, which is consistent with the prediction based on calculation.

It was also observed that the emission at ~ 700 nm was blue-shifted with increasing pump fluence as shown in **Figure 2.3(c)**. The continuous spectral shift cannot be ascribed to the repulsive interaction between photo-generated biexcitons at high pump intensity, which would appear as an additional peak at a higher energy than that of the single exciton peak.[24, 25] On the other hand, the peak energy (E_P) at excitation intensities (I_{ex}) below 60 μJ/cm^2 can be well-fitted (solid line in **Figure 2.3(c)**) with the expression $E_p = E_0 + c\sqrt[3]{I_{ex}}$, where E_0 is the extrapolated peak energy at zero intensity excitation and c is a fitting parameter. This is indicative of band bending, which is caused by an electric field generated by the separation of opposite charges across an interface and results in an emission blue-shift.[26-28] Deviation from the fit at pump intensities much larger than 60 μJ/cm^2 may be due to the

saturation of photo-generated charge carriers at the interface. These observations provide further evidence that the InP/ZnS seeded CdS tetrapods exhibit Type II behavior. Upon photoexcitation, most of the excitons are generated in the CdS tetrapod arms due to their much larger absorption cross-

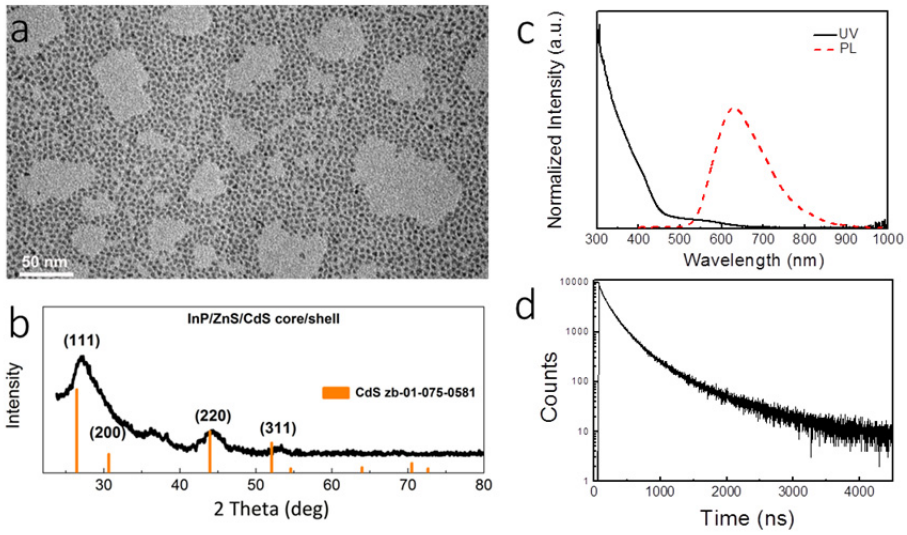

Figure 2.4 Structural and optical characterization of the core/shell InP/ZnS/CdS spheres. (a) Low resolution TEM and (b) powder XRD of InP/ZnS/CdS core/shell spheres. A reference spectrum (orange) of standard zinc blende CdS is included; (c) UV and PL spectrum of the InP/ZnS/CdS core/shell spheres. The absorption and emission of InP/ZnS are both redshifted upon the growth of the CdS shell on top. Comparing with the PL (500 nm) of the initial InP/ZnS seeds, the InP/ZnS/CdS core/shell spheres gives 628 nm emission with ~128 nm redshift of the PL spectrum. This further indicated the Type-II band alignment at the interface between InP/ZnS seed and CdS shell; (d) time resolved PL decay curve of InP/ZnS/CdS core/shell spheres showing a weighted average lifetime of ~ 280 ns.

section compared with the core at the branch point. The holes generated in the CdS arms localize to the InP core and emission takes place via recombination between electrons in CdS and holes in InP across the alloyed interface. Saturation of the hole states in InP would be expected to lead to radiative recombination within CdS due to the "exciton blocking effect", thus producing efficient multiexcitonic dual emission from both CdS and the InP/ZnS-CdS interface.

In order to better illustrate the efficiency of Type II InP/ZnS seeded CdS tetrapods in producing dual wavelength emission of similar peak intensity, a comparison was made with Type I CdSe seeded CdS tetrapods of similar CdS arm diameter and length. Both samples were excited with 400 nm pulses (1 KHz repetition rate, ~150 fs pulse duration) from a frequency doubled Ti : Sapphire laser. **Figures 2.5(a)** and **2.5(b)** show a series of pump intensity dependent PL spectra of dilute toluene solutions of equal concentrations of InP/ZnS seeded CdS tetrapods and CdSe seeded CdS tetrapods respectively, and it is readily seen that emission from both core and arms occurs at sufficiently large pump fluence. Their corresponding emission peak intensities as a function of the average number of photogenerated excitons per nanoparticle <N> are given in **Figure 2.5(c)**. It is seen that the saturation of the InP/ZnS-CdS interface emission at a pump threshold of ~ 10 $\mu J/cm^2$ was commensurate with a superlinear increase in the emission intensity of CdS, which may be attributed to the saturation of hole states within InP. The InP/ZnS-CdS interface emission therefore dominates at low pump fluence while the CdS emission prevails at high excitation intensities. In contrast, for the Type I tetrapods, the core CdSe emission starts to saturate at pump fluences about an order of magnitude larger without a corresponding superlinear increase in the CdS emission intensity. The sublinear increase of the CdSe core emission at large pump intensities is likely due to the Auger recombination process associated with multiexcitons[24,29] rather than core

state saturation. This size-dependent Auger recombination process can also explicate the saturation of emission from the CdS arms although at larger pump fluence (~ 1000 μJ/cm^2) given their much larger volume.

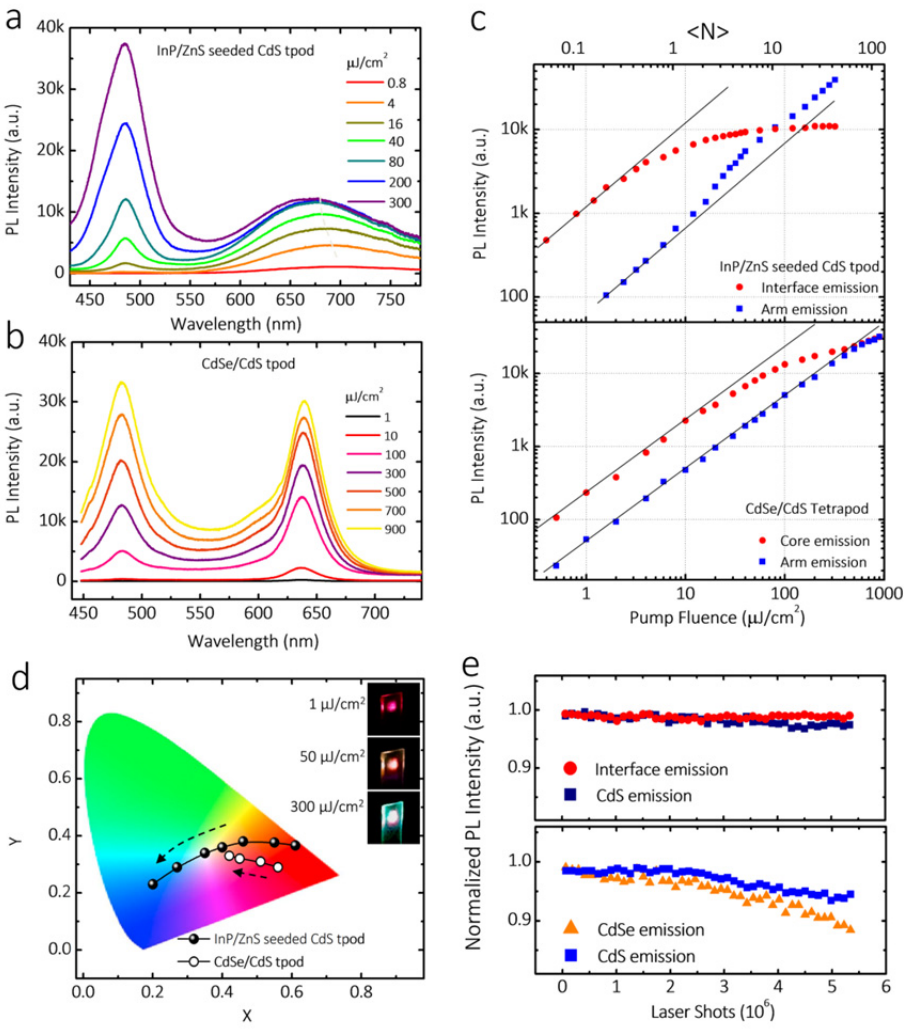

Figure 2.5 Pump-fluence dependent PL spectra from (a) InP/ZnS-CdS and (b) CdSe/CdS tetrapods with almost the same length of the CdS arms in the dilute toluene solution. (c) The plot of peak intensities of interface (red circles) and CdS arm (blue squares) emissions for InP/ZnS-CdS (upper panel) and CdSe/CdS tetrapods (lower panel) as a function of excitation fluence on a log−log scale in comparison to linear growth (solid line). (d) Pump-intensity dependent emission color coordinates plotted in the CIE 1931 chromaticity diagram for InP/ZnS-CdS and CdSe/CdS tetrapods. The arrows imply the increasing of pump fluence from 1 to 300 μJ/cm^2. Three inset photographs show the emission color changing of InP/ZnS-CdS tetrapods which were drop casted on a glass slide; (e) Emission intensity variation of Type II and Type I tetrapods upon the continuous excitation at a pump fluence of 300 μJ/cm^2 over the course of 1.5 hours.

Due to the cross-over of integrated emission intensity between core and arm at a relatively low pump fluence of ~ 100 μJ/cm^2 as illustrated in **Figure 2.5(c)**, InP/ZnS seeded CdS tetrapods exhibit a wide range of perceived emission color-tunability over a small excitation range. **Figure 2.5(d)** plots the calculated CIE coordinates according to the PL spectra in **Figures 2.5(a)** and **2.5(b)**. By increasing the pump fluence gradually from 0.4 - 300 μJ/cm^2, the effective emission color can be tuned from red to bluish-green passing through the coordinates for white, and photographs of the Type II tetrapods drop-casted on a glass substrate optically excited under different pump intensities are given in the insets of **Figure 2.5(d)**. In the case of the CdSe/CdS tetrapods, the emission color has a much more limited tunability and can only be changed from red to orange with increasing pump fluence. The phostability of the Type I and Type II tetrapods as MME emitters were evaluated by monitoring their core and arm emission intensity under continuous excitation at a pump fluence of 300 μJ/cm^2 over the course of 1.5 hours. As illustrated in **Figure 2.5(e)**, the core emission intensity from the Type II tetrapods did not show any noticeable decrease whereas that of the Type I tetrapods declined appreciably over the measurement time window. This may be rationalized by the presence of a detrimental Auger recombination process in the core region of Type I tetrapods at the high pump intensities used that can result in additional occurrences of charge trapping. In the case of the Type II nanocrystals, the Auger recombination process is highly suppressed,[21,30] leading in this case to higher photostability for the Type II tetrapods.

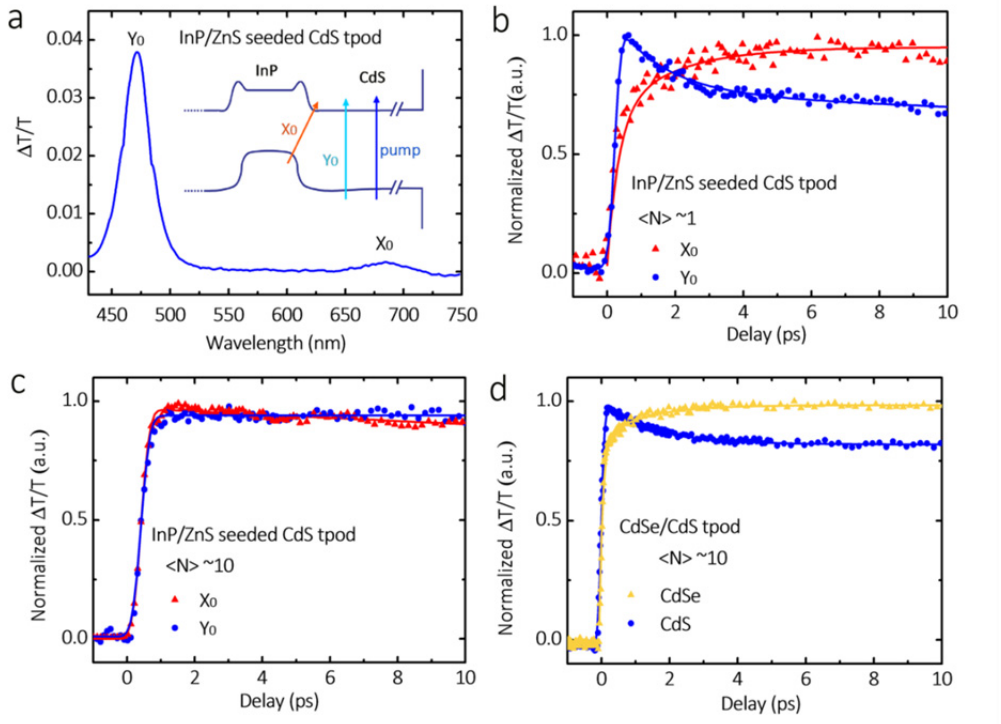

Figure 2.6 (a) Differential transmission spectra of InP/ZnS-CdS tetrapods dispersed in toluene at a probe delay of 1 ps under 400 nm light excitation at a pump fluence of 10 μJ/cm^2. The photobleaching (PB) bands labeled as X_0 and Y_0 are correspond to the transitions across the Type II interface and in the CdS arms, respectively, as shown schematically in the inset of the energy level diagram. Normalized PB transients probed at the peaks of the X_0 and Y_0 PB bands for InP/ZnS seeded CdS tetrapods with <N> ~1 (b) and <N> ~10 (c). (d) Normalized PB transients probed at the peaks of the CdSe and CdS transitions for the counterpart Type I tetrapods with <N> ~10.

In order to ascertain the origins of the early sublinear and superlinear increase in the InP/ZnS-CdS interface and CdS arm emission as a function of pump power, which is the basis for the wide color tunability obtained, the interplay of carrier dynamics between the core and arms of the tetrapod was investigated. Transient absorption (TA) measurements were performed on tetrapods to monitor their carrier relaxation and recombination processes. **Figure 2.6(a)** shows the differential transmission (ΔT/T) spectra at a probe delay of 1 ps following a 400 nm pulse excitation for InP/Zns seeded CdS tetrapods dispersed in toluene. Two photobleaching (PB) bands (i.e., ΔT/T > 0)

denoted as X_0 and Y_0 were observed, corresponding to the transition between the InP valence band and CdS conduction band across the alloyed interface and excitonic transitions within the CdS arm. The larger amplitude ratio of Y_0 to X_0 is due to the much larger volume of the CdS arms in comparison with the InP core.

Figure 2.6(b) and **2.6(c)** show the normalized bleach decay and formation kinetics monitored at the peak of the respective X_0 and Y_0 PB bands under different pump fluence. The X_0 and Y_0 PB signals are fitted with single rising and double decaying exponential functions, respectively, as shown with solid lines. At a pump fluence corresponding to <N> ~ 1 (where <N> is the average number of excitons per tetrapod), the buildup of the X_0 PB is simultaneously matched with a fast bleach decay at Y_0 PB occurring within ~ 1.0 ps, which reflects the approximate hole relaxation time from the CdS arm to the InP core. From the amplitude of the fast decay component of Y_0 PB, it may be estimated that not all of the photoexcited holes are localized into the core and some holes remain within the CdS arms. This is consistent with our earlier supposition that the hole states in InP become filled and the driving force for hole relaxation to the InP core is diminished, which results in the observed superlinear increase and saturation in the CdS and core-arm interface emission respectively as depicted in **Figure 2.5(c)**. The onset of saturation in the InP/ZnS-CdS interface emission as the pump fluence is increased to <N> ~10, the bleaching of X_0 and the corresponding decay of Y_0 occurs extremely fast, indicating that holes in CdS located close to the InP/ZnS core are sufficient to fully saturate its hole states. These TA results are consistent with the PL spectra in **Figure 2.5(c)**, where at this pump fluence, the Type II

emission is fully saturated and CdS emission increases linearly. In contrast, for CdSe seeded CdS tetrapods excited at the same high pump fluence (i.e., <N> ~10), there is still a fast decay (~1.4 ps) for the transition in the CdS arm and a correspondingly slow rise for the transition in the CdSe core as revealed in **Figure 2.6(d)**, which indicates that the core hole states in CdSe have not been filled completely. This may be explained by the weaker driving force for hole relaxation into the CdSe core due to the smaller valence band offset (~0.4 eV[31] as opposed to ~0.8 eV in InP-CdS) at the interface between the CdSe core and CdS arm. In the case of the InP/ZnS seeded CdS tetrapods, the large valence band offset between the InP/ZnS core and CdS arms provided a large thermodynamic impetus for arm-to-core hole localization, allowing for fast saturation of the hole states in the core.

2.4 Conclusions

In conclusion, we have demonstrated that Type II InP/ZnS seeded CdS tetrapods can achieve MME of comparable intensities at relatively low pump fluence and pump-dependent color tunability over a wide range on the CIE diagram. By comparing with Type I CdSe seeded CdS tetrapods of approximately the same CdS arm dimensions, it was concluded that the efficient dual emission, high photostability and wide color tunability in the Type II tetrapods was due to the large valence band offset and suppressed Auger recombination. This work highlights the importance of band alignment in the achievement of highly efficient color-tunable MME in semiconductor nanoheterostructures.

2.5 References

1. Han, M. Y.; Gao, X. H.; Su, J. Z.; Nie, S. *Nat. Biotechnol.* **2001,** 19, 631.

2. Jaiswal, J. K.; Mattoussi, H.; Mauro, J. M.; Simon, S. M. *Nat. Biotechnol.* **2003,** 21, 47.

3. Resch-Genger, U.; Grabolle, M.; Cavaliere-Jaricot, S.; Nitschke, R.; Nann, T. *Nat. Methods* **2008,** 5, 763.

4. Goldman, E. R.; Clapp, A. R.; Anderson, G. P.; Uyeda, H. T.; Mauro, J. M.; Medintz, I. L.; Mattoussi, H. *Anal. Chem.* **2004,** 76, 684.

5. Medintz, I. L.; Uyeda, H. T.; Goldman, E. R.; Mattoussi, H. *Nat. Mater.* **2005,** 4, 435.

6. Snee, P. T.; Somers, R. C.; Nair, G.; Zimmer, J. P.; Bawendi, M. G.; Nocera, D. G. *J. Am. Chem. Soc.* **2006,** 128, 13320.

7. Thakar, R.; Chen, Y. C.; Snee, P. T. *Nano Lett.* **2007,** 7, 3429.

8. Liu, W.; Howarth, M.; Greytak, A. B.; Zheng, Y.; Nocera, D. G.; Ting, A. Y.; Bawendi, M. G. *J. Am. Chem. Soc.* **2008,** 130, 1274.

9. Thakar, R.; Chen, Y. C.; Snee, P. T. *Nano Lett.* **2007,** 7, 3429.

10. Lutich, A. A.; Mauser, C.; Da Como, E.; Huang, J.; Vaneski, A.; Talapin, D. V.; Rogach, A. L.; Feldmann, J. *Nano Lett.* **2010,** 10, 4646.

11. Galland, C.; Brovelli, S.; Bae, W. K.; Padilha, L. A.; Meinardi, F.; Klimov, V. I. *Nano Lett.* **2013,** 13, 321.

12. Li, L.; Reiss, P. *J. Am. Chem. Soc.* **2008,** 130, 11588.

13. Fiore, A.; Mastria, R.; Lupo, M. G.; Lanzani, G.; Giannini, C.; Carlino, E.; Morello, G.; De Giorgi, M.; Li, Y.; Cingolani, R.; Manna, L. *J. Am. Chem. Soc.* **2009,** 131, 2274.

14. Manna, L.; Milliron, D. J.; Meisel, A.; Scher, E. C.; Alivisatos, A. P. *Nat. Mater.* **2003,** 2, 382.

15. Talapin, D. V.; Nelson, J. H.; Shevchenko, E. V.; Aloni, S.; Sadtler, B.; Alivisatos, A. P. *Nano Lett.* **2007,** 7, 2951.

16. Kan, S.; Mokari, T.; Rothenberg, E.; Banin, U. *Nat. Mater.* **2004,** 3, 72.

17. Ung, T. D. T.; Reiss, P.; Nguyen, Q. L. *Appl. Phys. Lett.* **2010,** 97, 193104.

18. Ung, T. D. T.; Pham, T. T.; Nguyen, Q. L.; Li, L.; Reiss, P. *Appl. Phys. Lett.* **2010,** 96, 073102.

19. *CRC Handbook of Chemistry and Physics. 82nd ed.; CRC Press, Inc.: FL **2001**; p 2588.*

20. Oladeji, I. O.; Chow, L. *Thin Solid Films* **2005,** 474, 77.

21. Dennis, A. M.; Mangum, B. D.; Piryatinski, A.; Park, Y. S.; Hannah, D. C.; Casson, J. L.; Williams, D. J.; Schaller, R. D.; Htoon, H.; Hollingsworth, J. A. *Nano Lett.* **2012,** 12, 5545.

22. Piryatinski, A.; Ivanov, S. A.; Tretiak, S.; Klimov, V. I. *Nano Lett.* **2007,** 7, 108.

23. Wu, J. C.; Zheng, J. W.; Zacherl, C. L.; Wu, P.; Liu, Z. K.; Xu, R. *J. Phys. Chem. C* **2011,** 115, 19741.

24. Htoon, H.; Malko, A. V.; Bussian, D.; Vela, J.; Chen, Y.; Hollingsworth, J. A.; Klimov, V. I. *Nano Lett.* **2010,** 10, 2401.

25. Kulakovskii, V. D.; Bacher, G.; Weigand, R.; Kummell, T.; Forchel, A.; Borovitskaya, E.; Leonardi, K.; Hommel, D. *Phys. Rev. Lett.* **1999,** 82, 1780.

26. Morello, G.; Fiore, A.; Mastria, R.; Falqui, A.; Genovese, A.; Creti, A.; Lomascolo, M.; Franchini, I. R.; Manna, L.; Della Sala, F.; Cingolani, R.; De Giorgi, M. *J. Phys. Chem. C* **2011,** 115, 18094.

27. Wang, C. H.; Chen, T. T.; Tan, K. W.; Chen, Y. F.; Cheng, C. T.; Chou, P. T. *J. Appl. Phys.* **2006,** 99, 123521.

28. Chang, W. H.; Liao, Y. A.; Hsu, W. T.; Lee, M. C.; Chiu, P. C.; Chyi, J. I. *Appl. Phys. Lett.* **2008,** 93, 033107.

29. Garcia-Santamaria, F.; Chen, Y. F.; Vela, J.; Schaller, R. D.; Hollingsworth, J. A.; Klimov, V. I. *Nano Lett.* **2009,** 9, 3482.

30. Oron, D.; Kazes, M.; Banin, U. *Phys. Rev. B* **2007,** 75, 035330.

31. Steiner, D.; Dorfs, D.; Banin, U.; Della Sala, F.; Manna, L.; Millo, O. *Nano Lett.* **2008,** 8, 2954.

CHAPTER 3

Visible to Near Infrared Emission from Branched Type I and Type II InP Based Nanostructures

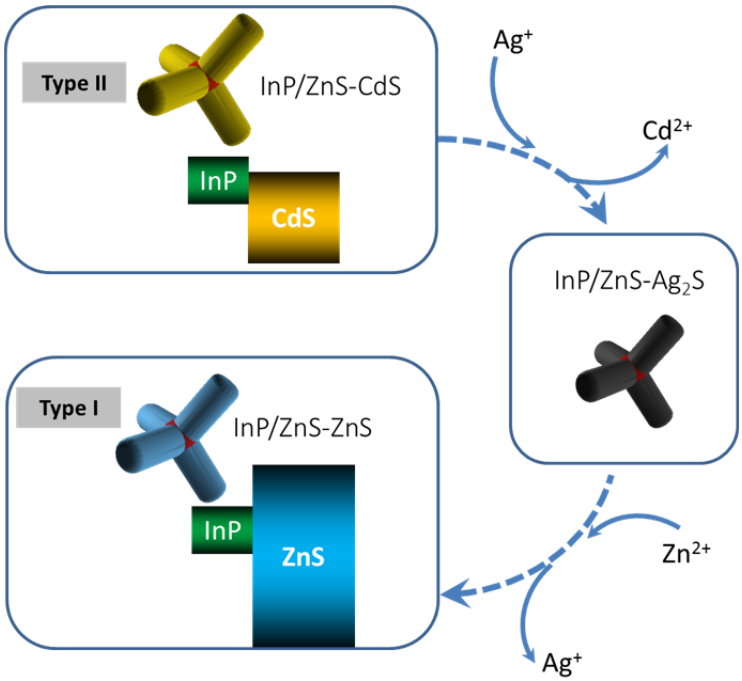

3.1 Introduction

Amongst the various wet-chemically synthesized semiconductor nanoparticles currently known, colloidal InP is arguably one of the most promising alternatives to the proverbial CdSe quantum dot (QD), whose emission is capable of covering the entire visible range.[1-5] Given its bulk Bohr exciton radius of 11 nm and a bulk band gap of ~1.34 eV, which may be compared with that of CdSe at 5.6 nm and ~1.74 eV respectively,[6] strong quantum confinement effects in nanometer-sized InP and a consequently wide spectral tunability from 450 nm to 750 nm has been demonstrated for InP particles.[4] A notable number of efforts have been made to produce highly crystalline InP QDs with high quantum yields and long-term photostability, typically via surface passivation with a larger band gap semiconductor such as ZnS or ZnSe to yield a Type I configuration.[7,8] Due to these improvements, InP based QDs have been harnessed for optical applications such as bio-imaging[9] and light emitting diodes (LEDs).[10,11] In such applications, the desired wavelengths of emission and action cross-section of the chromophore are of paramount importance, however methods to extend the spectral window of quantum confined InP beyond its bulk emission while increasing its absorption cross-section have been extremely limited. One possible solution to achieve such properties is the use of anisotropic Type II nanoheterostructures, which have been reported for II-VI materials. Take the ZnSe seeded CdS nanorod as an example, the rod-like CdS shell serves as an antenna for absorbing photons while radiative excitonic recombination takes place at the interface between ZnSe and CdS.[12] In the case of branched structures such as tetrapods, the absorption cross-section at the same wavelength of excitation

can exceed that of spherical QDs by factors on the order of 100.[13] Unlike II-VI semiconductors, however, wet-chemistry methodologies involving colloidal III-V semiconductor QDs are considerably less mature and developed, and the synthesis of well-defined core/shell anisotropic nanoheterostructures based on an InP core has to date remained an elusive goal to achieve.

Developments in the wet-chemical synthesis of colloidal anisotropic heterostructures have focused largely on II-VI semiconductor systems, where surfactant-controlled and seeded growth approaches have successfully produced highly monodisperse structures such as tetrapod and rod nanoheterostructures.[14-17] On the other hand, efforts to grow the III-V based analogues of such nanoparticles via a wet chemistry approach have been far less intensive, presumably due to the lack of air-stable precursors and facet-specific binding ligands. Previous efforts to fabricate III-V semiconductor nanowires and nanorods employed metal nanoparticles which served as catalysts for nucleation,[18-22] analogous to the well-known vapor-liquid-solid (VLS) techniques often used to produce semiconductor nanowires.[23,24] The dimensions of the resulting III-V nanorods or wires, however, were generally not well-controlled or monodisperse, in contrast with their colloidal II-VI counterparts synthesized via wet-chemical means. Moreover, direct contact with the metal nanoparticle catalyst can result in severe fluorescence quenching, thus nullifying an important optical property of the semiconductor nanostructure. Herein we show that core-shell InP/ZnS based QDs can serve as seeds for the heterogeneous nucleation and growth of CdS arms, forming structurally well-defined tetrapods of high size uniformity. The emission wavelengths were red-shifted by ~0.71 eV as compared to the original InP

based cores, along with significantly lengthened photoluminescence (PL) lifetimes of ~ 500 ns. These observations collectively suggest a Type II alignment between the InP/ZnS based core and CdS arms where the holes are likely to remain in InP while the electrons are delocalized into the CdS arms upon exciton formation, consistent with the behavior of bulk InP/CdS.[25] Furthermore, we demonstrate that via a series of facile cationic exchange processes, the as-synthesized Type II InP based core seeded CdS may be transformed to Type I InP/ZnS-ZnS tetrapods via intermediate InP seeded Ag_2S tetrapod structures. A dramatic blueshift of the fluorescence to shorter wavelengths comparable to the original emission wavelength of the InP based cores was observed, commensurate with the Type I band alignment. Remarkably, the fact that In^{3+} did not undergo cationic exchange with Ag^{+} or Zn^{2+} under the reaction conditions employed in this work suggests that cationic exchange may be a feasible synthetic route towards the derivation of a large variety of anisotropic InP based nanoheterostructures.

3.2 Experimental section

3.2.1 Chemicals and materials

Myristic acid (MA, 99 %), tris(methylsilyl) phosphine ($P(TMS)_3$, 95%), 1-octadecene (ODE, 90%), zinc acetate ($Zn(AC)_2$, 99%), 1-dodecanethiol (DDT, 97%), cadmium oxide (CdO, 99.5%), sulfur (S, reagent grade), were purchased from Sigma Aldrich. Indium acetate ($In(AC)_3$, 99.99%), trioctylphosphine (TOP, 97%), silver nitrate ($AgNO_3$, 99%), zinc nitrate ($Zn(NO_3)_2$, 99%) were purchased from Alfa Aesar. n-octadecylphosphonic acid (ODPA, 97%), trioctylphosphine oxide (TOPO, 99%) and n-hexylphosphonic acid (HPA, 97%) were purchased from Strem. All the

chemicals were used as received without further purification. Unless stated otherwise, all reactions were conducted in oven-dried glassware under a nitrogen atmosphere using standard Schlenk techniques.

3.2.2 Synthetic details

Synthesis of InP/ZnS seeds

Refer to **Chapter 2**.

Synthesis of InP/ZnS seeded CdS (InP/ZnS-CdS) tetrapods

Refer to **Chapter 2**.

Cation exchange from InP/ZnS-CdS to InP/ZnS-Ag_2S tetrapods:

An Ag^+ stock solution was produced as follows: $AgNO_3$ (0.0035g) was dissolved in methanol (1 mL), yielding a concentration of 0.02M. To about 0.022 nmol of processed InP/ZnS-CdS tetrapods in toluene (1 mL), Ag^+ stock solution (60 μL) was added dropwise with vigorous stirring. The reaction was carried out under dark conditions at ~ -15 ^oC for about 10 minutes. The products were precipitated by adding excess methanol to the growth solution, and centrifuged at 3900rpm for 6 min. Upon discarding the supernatant, the resulting InP/ZnS-Ag_2S tetrapods were then dispersed in 1 mL toluene for further cation-exchange reactions.

*Note that the concentration of InP/ZnS-CdS tetrapods was evaluated using the bulk molar absorption coefficient of CdS at 350 nm (ε_{350} for CdS is 6.15×10^7 [26]). This approximation was used due to the fact that the volume of the InP/ZnS core is about 240 times smaller than that of the 4 CdS arms (based on a 2.8 nm diameter InP/ZnS core with CdS arms having a diameter of 5 nm

and an arm length of 28 nm), hence absorption at blue wavelengths is essentially attributed to CdS.

Cation exchange from InP/ZnS- Ag_2S to InP/ZnS-ZnS tetrapods:

A Zn^{2+} stock solution was prepared as follows: $Zn(NO_3)_2$ (0.945g) was dissolved in methanol (5mL). The entire sample of InP/Ag_2S tetrapods as described above was dispersed in toluene and stirred vigorously at 60^oC. The Zn^{2+} stock solution (0.6 mL) was then slowly added to the solution of tetrapods, and the overall mixture was stirred for 10 mins at 60^oC. TOP (0.07 mL) was then added to the mixture, and stirred at 70^oC for ~ 20 hours. The final products obtained were precipitated from methanol once, and then further processed via 2-3 cycles of precipitation/re-dispersion in acetone/ chloroform, before finally dispersing in cyclohexane for characterization.

3.2.3 Characterizations

Structural characterization

Transmission Electron Microscopy (TEM): A JEOL JEM 1220F (100 kV accelerating voltage) microscope was used to obtain bright field TEM images of the nanoparticles. For TEM sample preparation, a drop of the nanoparticle solution was placed onto a 300 mesh copper grid covered with a continuous carbon film. Excess solution was removed by an adsorbent paper and the sample was dried at room temperature. The High-Resolution TEM images and detailed elemental analysis were carried out on a FEI Titan 80-300 electron microscope (operated at 300 KV) which is equipped with an electron beam monochromator, an energy dispersive X-ray spectroscopy (EDX) and a Gatan electron energy loss spectrometer. The probing electron beam size for

point EDX measurements was around 0.3 nm. The dwell time for each EDX spectrum was about 10 s.

X-Ray Diffraction (XRD): XRD data was obtained with a diffractometer (Bruker AXS, GADDS) using Cu-Kα radiation (λ=1.540598Å) in the range of 20˚ to 80˚. Samples were prepared on a clean silicon wafer by placing several drops of concentrated nanoparticle samples in hexane on the silicon surface and dried at 60˚C in the oven. This was repeated several times until a thin layer of solid was formed on the silicon substrate.

Optical characterization

Absorption spectra were obtained with an Agilent 8453 UV-Visible spectrophotometer using a quartz cuvette with a path length of 1 cm. Photoluminescence (PL) spectra in the visible - NIR region were collected using a HORIBA Jobin Yvon Fluorolog 3 spectrometer equipped with a silicon and liquid nitrogen cooled InGaAs photodiode detector. Time-resolved fluorescence lifetime profiles were obtained using a time-correlated single photon counting TCSPC spectrofluorimeter (Fluorohub, Horiba Jobin Yvon). Care was taken to ensure that the concentrations of the core and core-seeded nanostructures were sufficiently dilute to avoid contributions from re-absorption or energy transfer. Absolute quantum yield measurements of the various samples were carried out on a Hamamatsu Quantaurus-QY with NIR model (C11347-12) which has an effective range from 400 nm to 1100 nm.

3.3 Results and discussions

As discussed in this thesis (**Chapter 2**), we employed ZnS coated zb-InP QDs which were synthesized via a previously reported single pot procedure.[27] The one-pot synthetic approach resulted in an alloyed InZnP interfacial layer

between the InP core and a thin outermost ZnS shell, as previously characterized by Reiss et al.[28, 29] **Figure 3.1** is a transmission electron microscope (TEM) image of the InP/ZnS-CdS tetrapods produced via a slightly modified seeded approach of Manna et. al.[16] The resulted tetrapods possessed CdS arm dimensions of ~ 5.2 nm in diameter and ~ 28.5 nm in length on average. Analogous to the seeded growth of CdSe/CdS tetrapods, the use of ODPA and HPA as surfactants was critical for tetrapod arm growth in our system, and it is reasonable to assume that the growth mechanism for the branched arms follow closely to that of CdSe/CdS.[17]

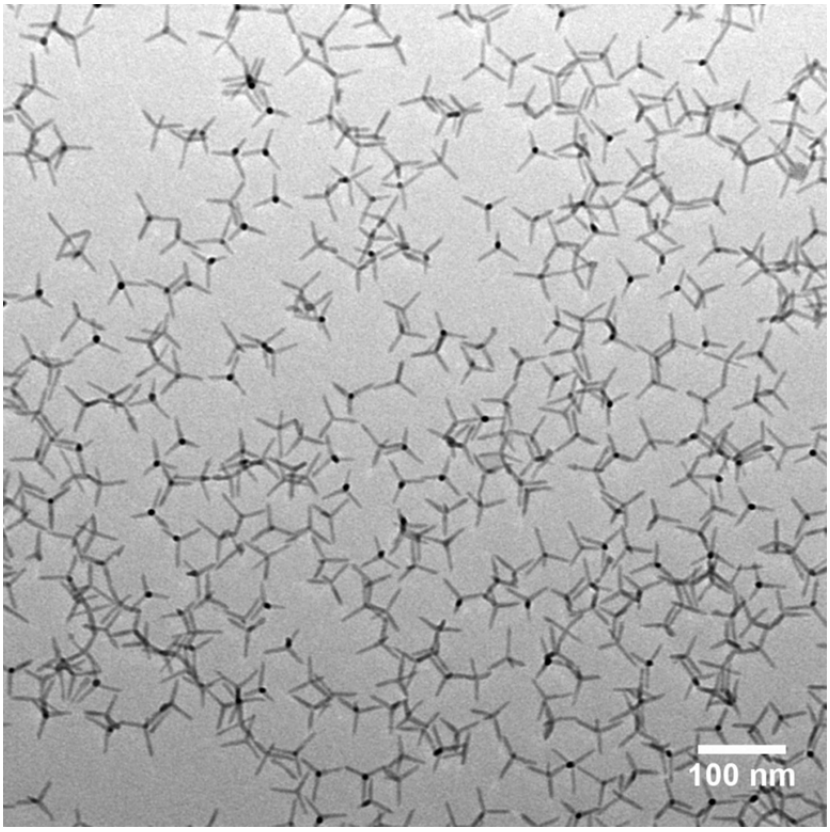

Figure 3.1 Low resolution TEM image of InP/ZnS seeded CdS tetrapods.

Structural and optical characterization of the as-synthesized InP/ZnS cores and InP/ZnS seeded CdS tetrapods, including powder X-ray diffraction (XRD) measurements, UV-vis / PL spectra, and lifetime which were

summarized in **Figure 2.1** and **Figure 2.3** in **Chapter 2**. Although the ZnS layer seems to form a type I alignment for both InP core and CdS arm, according to our previous calculations and analysis (see **Figure 2.2(c)** and **2.2(d)**, **Chapter 2**), we were able to conclude that the electron and

hole ground state wavefunction overlap was very small and that the maximal overlap was at the interface. This is consistent with a Type-II structure in which recombination occurs at the interface. Only if the thickness of ZnS increases a lot that can cause a decrease of e-h overlap at the interface, indicating that a thin Type-I

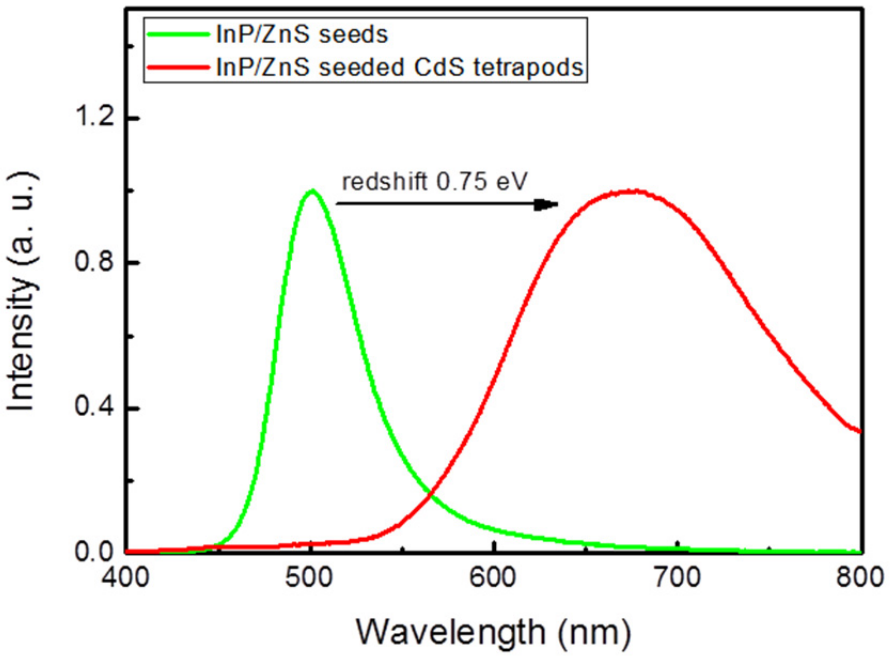

Figure 3.2 PL data of InP/ZnS seeds (green) and InP/ZnS seeded CdS tetrapod (red). The InP/ZnS seeds have the emission of 500 nm under excitation wavelength of 365 nm, while InP/ZnS seeded CdS tetrapods redshifted to 674 nm exhibiting type II band alignment.

barrier should not interfere with charge separation. Consequently, it may be expected that the tetrapod effectively possess a Type II alignment between its InP core and CdS arms.

The band alignment between bulk InP and CdS forms a staggered Type II configuration in which spatial separation of an exciton at the interface of the two materials results in the electron primarily localized in CdS while the hole is confined to the InP moiety.[30] For a sufficiently thick shell (a tetrapod-shape), the electron wavefunction is predominantly located in CdS and subsequently undergoes spatially indirect radiative recombination with the hole located in the InP core. Consequently, the emission is dramatically redshifted with respect to band-edge recombination in interface and the PL lifetime is significantly lengthened. The InP/ZnS-CdS tetrapods were commensurate with delocalization of the electron wavefunction into the CdS arms. As shown in **Figure 3.2**, the PL emission for the InP/ZnS seeds and InP/ZnS seeded CdS tetrapods at 500 nm and 674 nm respectively. Such a dramatic redshift of the PL peak again indicated the type II band alignment at the interface regardless of the thin ZnS layer between the seed and the arm.

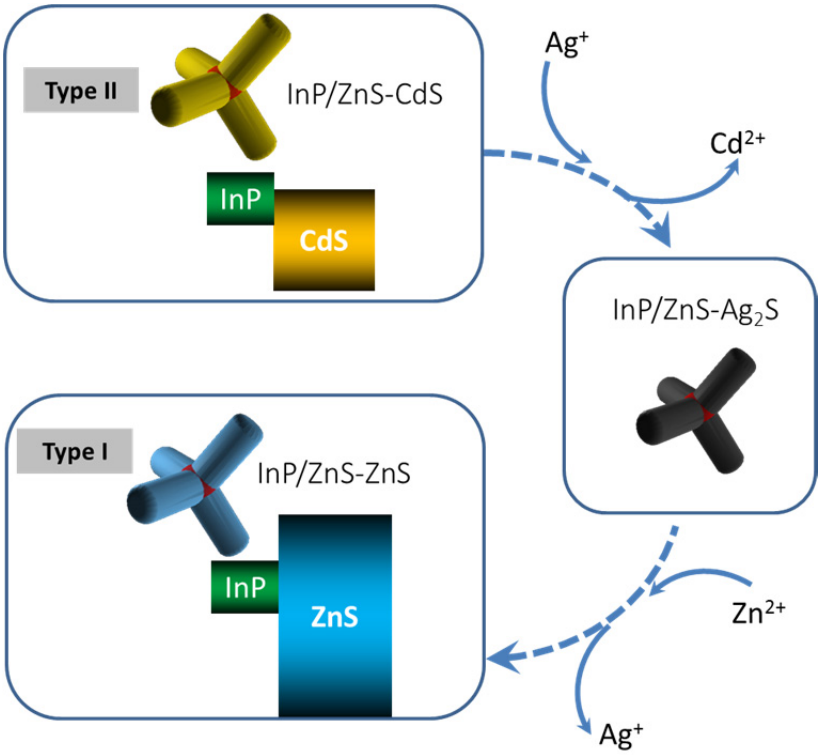

Scheme 3.1. Illustration of the sequential cation exchange process that transforms InP/ZnS-CdS to InP/ZnS-Ag_2S and InP/ZnS-ZnS tetrapods via sequential exposure to Ag^+ and Zn^{2+} respectively.

In order to expand the potential utility of anisotropic InP based tetrapods in different applications, we explored the possibility of using cationic-exchange reactions to transform the tetrapod arms into other materials, thereby modifying the optical properties of the entire tetrapod construct. In the case of core/shell particles and heterostructures composed of II-VI QDs, exposure to cations such as Cu^+ and Ag^+ in the presence of ligands which preferentially coordinate to the cations in the II-VI semiconductor results in a spontaneous cation-exchange reaction in which the shape and size of the original QDs are preserved while transformation to the new semiconductor material takes place.[31-33] For cations such as Pb^{2+} which cannot be exchanged directly with CdS for example, transformation to PbS can be mediated via the formation of an intermediate structure such as $Cu_{2-x}S$.[34] For III-V QDs on the

other hand, exposure to Cu^+ or Ag^+ does not result in cation-exchange, but rather a diffusion of these guest ions into the lattice vacancies of the III-V host.[35] We thus deduced that for the Type II InP/ZnS seeded CdS tetrapods with a III-V core and II-VI arms, sequential cationic exchange with Ag^+ followed by Zn^{2+} should result in the formation of Type I InP seeded ZnS tetrapods with dramatically different optical properties, as illustrated in **Scheme 3.1**.

Briefly, processed InP/ZnS seeded CdS tetrapods were dispersed in toluene and exposed to $AgNO_3$ in methanol with stirring for ~ 15 minutes under dark conditions in order to minimize the photoreduction of Ag^+. This resulted in the formation of tetrapods with an InP based core and Ag_2S arms, as shown in **Figure 3.3(a)**. The material composition of the InP/ZnS-Ag_2S tetrapods was investigated via EDX measurements, which confirmed the presence of Ag in the arms of the tetrapods and the retention of the InP core, as depicted in **Figure 3.3(b)**. The absence of Cd suggested that the cationic exchange reaction proceeded to completion. The presence of several dark clusters at the centre or tips of the tetrapod arms was found to be that of Ag, which may be attributed to the reduction of unreacted Ag^+. While the underlying mechanism for the reduction of Ag^+ on the surface of Ag_2S is unclear since no reducing agent was added, we can only speculate that the reduction of Ag^+ to Ag (reduction potential = +0.80 V) may have been facilitated by the presence of TOP From the initial synthesis of the InP/ZnS seeded CdS tetrapods or Cd^+ (oxidation potential to Cd^{2+} = +1.01 V) that may be present at the lattice surface during the cation-exchange process. Optical characterization via UV-Vis absorption spectrometry, as delineated in **Figure**

3.4 showed a transition from a spectrum portraying a number of peaks distinctive of CdS in the UV- blue region to an essentially featureless and broad absorption profile that extends to the NIR wavelengths, as is expected

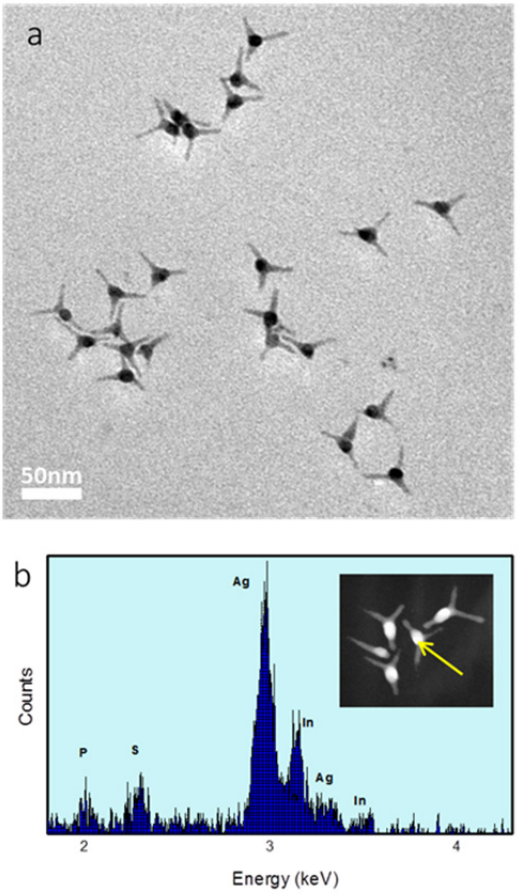

Figure 3.3 (a) Bright-field TEM image of InP/ZnS-Ag_2S tetrapods; (b) Point EDX at the central region of a typical tetrapod (shown in inset). The resulted Ag signal is significantly higher than In signal, possiblly due the silver metal deposition on the obtained Ag_2S tetrapods.

for Ag_2S which has a bulk band gap of ~ 1.1 eV.[36] The insets in **Figure 3.4** illustrate the appearance of the solutions of tetrapods before and after the cation-exchange process, yielding pale yellow and dark brown solutions respectively. Fluorescence from the InP/ZnS core was entirely quenched, which may be understood by the close proximity of the Ag cluster and the

high likelihood that excitons generated in the InP core are transferred to the Ag_2S arms.

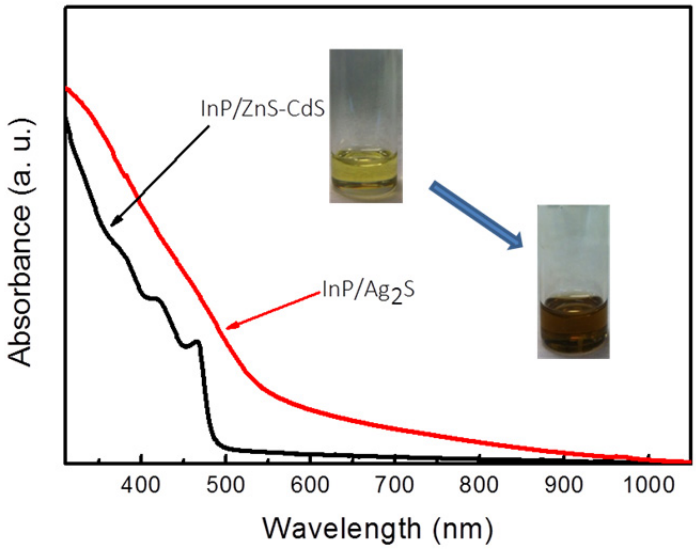

Figure 3.4 UV-Vis absorption of the tetrapod solution before (black) and after (red) exchange with Ag^+. Inset: Corresponding solution vials before and after the cation exchange process.

The as-synthesized InP/ZnS-Ag_2S tetrapods dispersed in toluene were exposed to a methanolic solution of $Zn(NO_3)_2$, along with trioctylphosphine (TOP) as a soft base which can stabilize Ag^+ and thus provide a thermodynamic impetus for the cation-exchange reaction with Zn^{2+}. Unlike the spontaneous displacement of Cd^{2+} by Ag^+ at room temperature, cation-exchange with between Ag^+ and Zn^{2+} required to be carried out at a reaction temperature of ~60-80 ^oC for ~ 24 hours. It should be noted that the use of Cu_2S as an intermediate for the conversion of nanostructures of CdS to ZnS, as previously reported by Li et. al., requires shorter reaction times but much higher reaction temperatures of 250^oC to drive the exchange between Cu^+ and Zn^{2+}.[37] Interestingly, the Ag domains originally present on the Ag_2S arms were

no longer observed after conversion to ZnS, as shown in the TEM image in **Figure 3.5(a)**, analogous to the removal tetrapods undergoing cationic

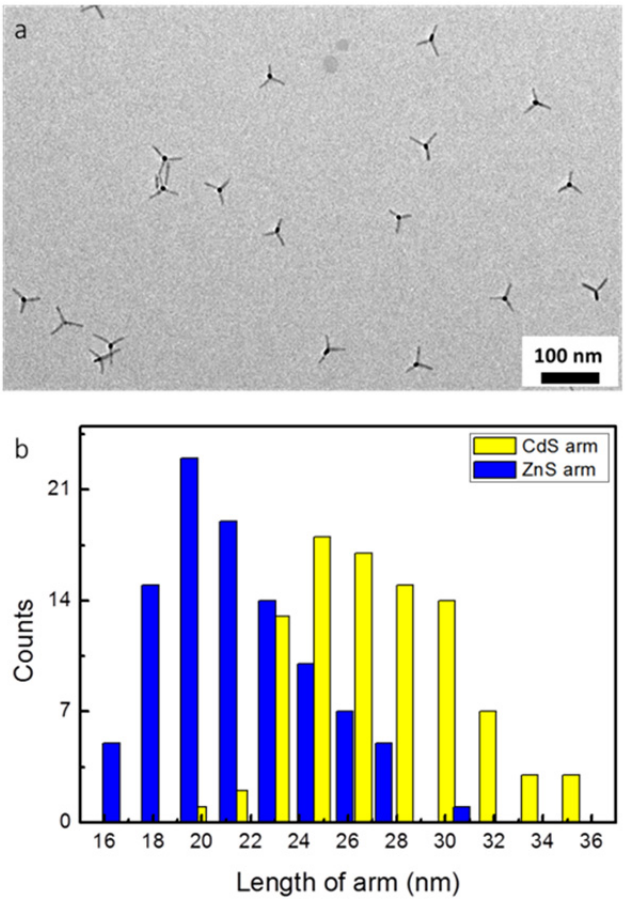

Figure 3.5 (a) Representative TEM image of InP/ZnS-ZnS tetrapod; (b) Size distribution of tetrapod arm length when comparing InP/ZnS-CdS and InP/ZnS-ZnS tetrapods

exchange with Ag^{+} [38] As illustrated of wurtzite ZnS. **Figure 3.6** presented the HRTEM of InP/ZnS-ZnS tetrapods, where the lattices fringe along the arm of wz-ZnS was presented as {002} where the d-spacing is 0.312 nm (smaller than wz-CdS (002) d-spacing of 0.33 nm along the arm). While it is seen that the general shape monodispersity of the Zn-exchanged tetrapods were preserved during the reaction, close examination of ~ 30 randomly chosen tetrapods revealedthat the length of the arms were shorter as compared with the original

InP/ZnS seeded CdS tetrapods (see **Figure 2.1(e)** in **Chapter 2**), which may be attributed to the fact that a volume contraction of ~ 21 % is expected going from wurtzite CdS to wurtzite ZnS

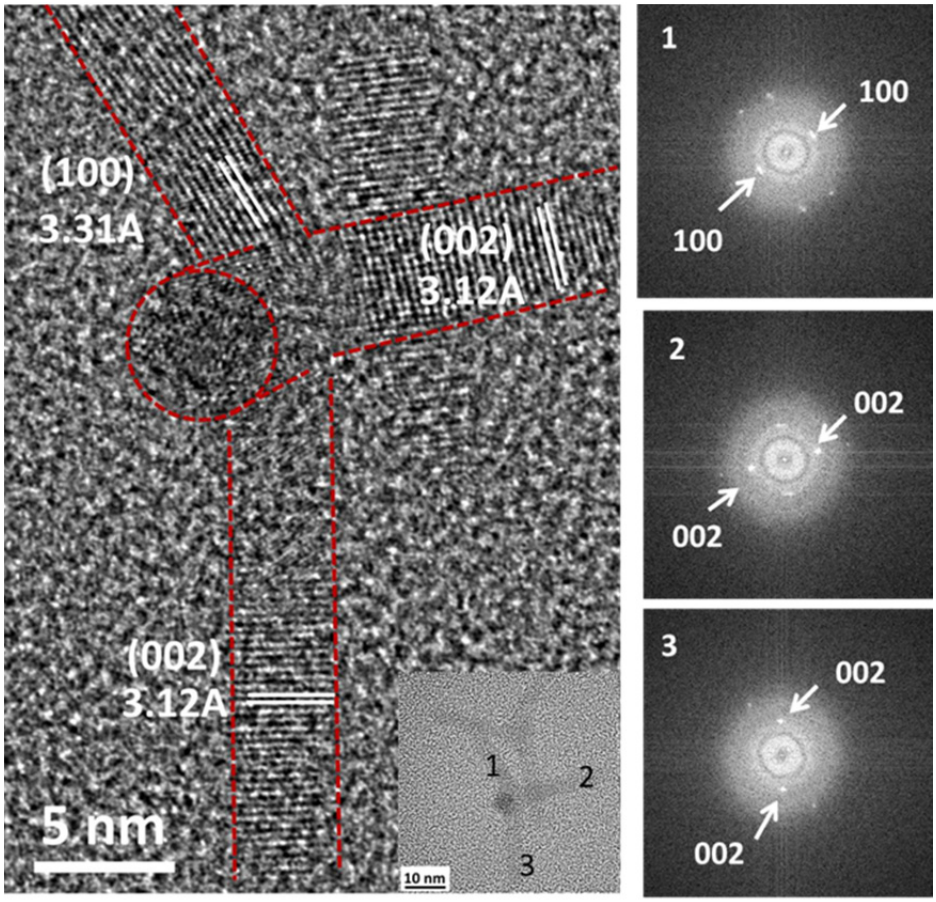

Figure 3.6 HRTEM of a InP/ZnS-ZnS tetrapod. Small inset is the zoom out image of the same tetrapod, with number one to three labeled on each arm.The labels (1), (2) and (3) correspond to the FFT analysis of the lattice planes on each arm (right side images).

. Characterization of the materials composition of the InP/ZnS-ZnS tetrapods was carried out via point EDX analysis which showed that Ag was wholly absent and that the arms of the tetrapods comprised entirely of ZnS while the branch point contained In, P, Zn and S, as may be seen in the EDX spectrum in **Figure 3.7**. This strongly suggests that the InP based core was preserved during the cation-exchange process between Ag^{+} and Zn^{2+}.

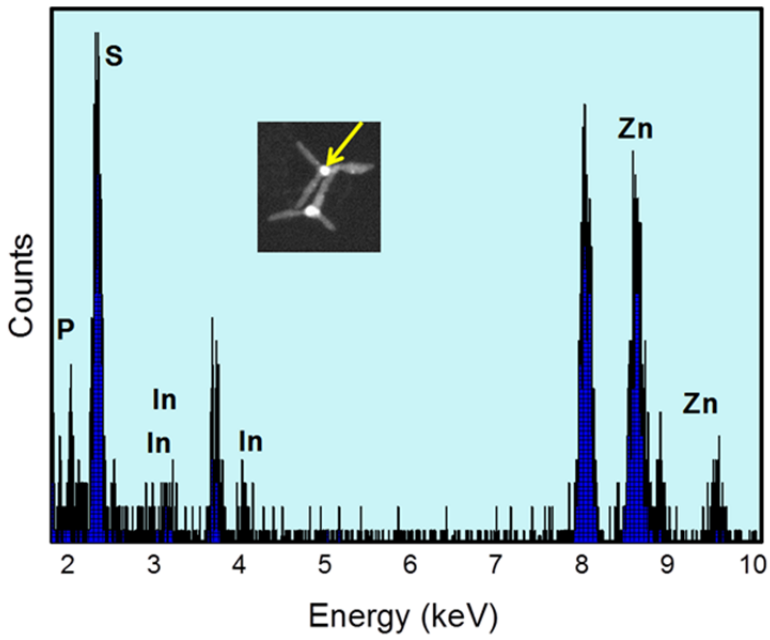

Figure 3.7 Point EDX at the central region of a typical tetrapod (HADDF image was shown in inset).

Further evidence for the conservation of the InP structure within the tetrapod branch point is given by PL measurements conducted at room temperature, which showed a remarkable recovery of fluorescence peaked at ~ 530 nm with a FWHM of ~ 0.35 eV, as seen in **Figure 3.8**. The emergence of this emission at a wavelength about 430nm to the blue of the InP/ZnS seeded CdS tetrapod emission is consistent with the transition from a Type II to Type I energy alignment between the InP/ZnS core and the ZnS arms. Compared to the original InP/ZnS seeds which exhibited fluorescence centred at ~510 nm, the PL peak of the InP/ZnS-ZnS tetrapods was red-shifted by ~ 20 nm, which may be explicated by the partial leakage of the electron wavefunction from the InP based core into the four ZnS arms. The absolute quantum yield of the InP/ZnS seeded ZnS tetrapods, however, was low and on the order of ~ 1% at an excitation wavelength of 360 nm. One plausible reason may be the presence of Ag^{+} impurities in sufficiently low amounts that were not detectable via EDX,

yet the incorporation of even a few impurity atoms per semiconductor nanoparticle is sufficient to drastically suppress its emissive properties.[39]

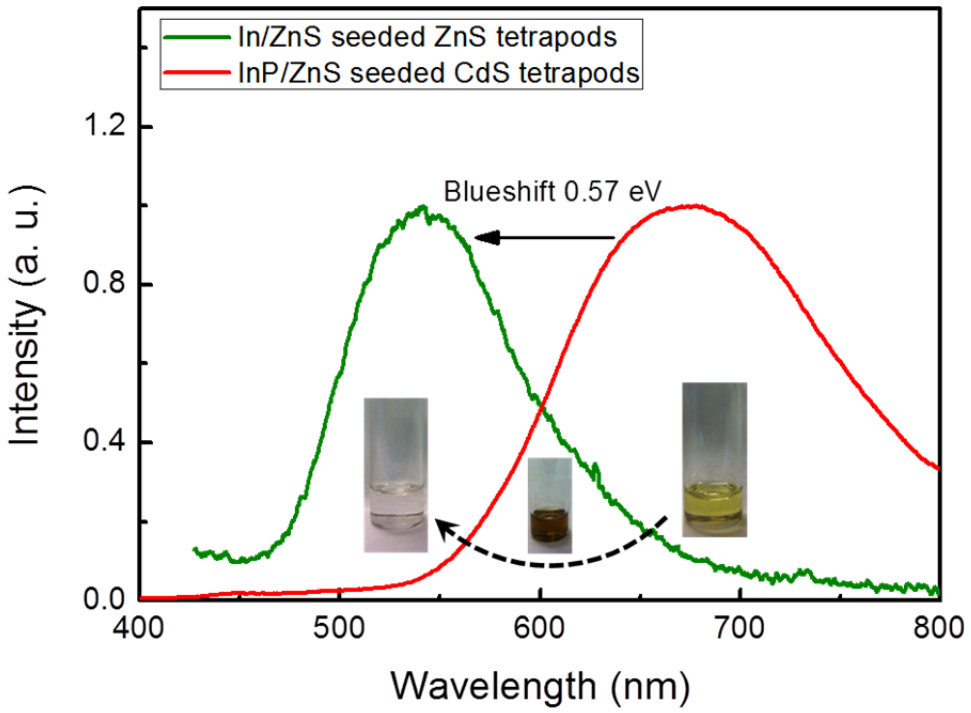

Figure 3.8 PL profile of InP/ZnS seeded ZnS tetrapods in toluene (dark green). The PL of the original InP/ZnS seeded CdS tetrapods (red) is included as reference. The digital photograph of the initial Type I tetrapod (light yellow in toluene), transform into InP/ZnS seeded ZnS Type I tetrapod (colorless in toluene) through Ag_2S tetrapods (dark brown color solution).

3.4 Conclusions

In summary, we have demonstrated the synthesis of monodisperse Type II InP/ZnS seeded CdS tetrapods. The success of this technique hinged upon the use of core-shell InP/ZnS particles as seeds, which importantly conferred structural stability to the InP core at high temperatures and retained its zinc-blende crystal phase. Via a sequential cationic-exchange process with Ag^+ and then Zn^{2+}, InP/ZnS-ZnS tetrapods were successfully produced at relatively low temperatures of ~60 – 80 ^oC, thus allowing the size-dispersity

and shape morphology of the original tetrapods to be retained. These Type I tetrapods exhibited emission in the visible range, about 170 nm blueshifted from their InP/ZnS-CdS counterparts. The unprecedented fabrication of these III-V semiconductor seeded tetrapods whose arms are comprised of a II-VI material opens up avenues for deriving novel optical properties based on III-V particles via facile cation-exchange processes. Coupled with the large absorption cross-section and potentially enhanced charge transport attributes that stem from a branched morphology, these tetrapods may find newfound utility in solution-processed optoelectronic devices.

3.5 References

1. Stuczynski, S. M.; Opila, R. L.; Marsh, P.; Brennan, J. G.; Steigerwald, M. L., *Chem. Mat.* **1991,** 3, 379.

2. Micic, O. I.; Curtis, C. J.; Jones, K. M.; Sprague, J. R.; Nozik, A. J., *J. Phys. Chem.* **1994,** 98, 4966.

3. Battaglia, D.; Peng, X. G., *Nano Letters* **2002,** 2, 1027.

4. Xie, R.; Battaglia, D.; Peng, X., *J. Am. Chem. Soc.* **2007,** 129, 15432.

5. Xu, S.; Ziegler, J.; Nann, T., *J. Mater. Chem.* **2008,** 18, 2653.

6. Guzelian, A. A.; Katari, J. E. B.; Kadavanich, A. V.; Banin, U.; Hamad, K.; Juban, E.; Alivisatos, A. P.; Wolters, R. H.; Arnold, C. C.; Heath, J. R., *J. Phys. Chem.* **1996,** 100, 7212.

7. Lim, J.; Bae, W. K.; Lee, D.; Nam, M. K.; Jung, J.; Lee, C.; Char, K.; Lee, S., *Chem. Mat.* **2011,** 23, 4459.

8. Kim, S.; Kim, T.; Kang, M.; Kwak, S. K.; Yoo, T. W.; Park, L. S.; Yang, I.; Hwang, S.; Lee, J. E.; Kim, S. K.; Kim, S. W., *J. Am. Chem. Soc.* **2012,** 134, 3804.

9. Yong, K. T.; Ding, H.; Roy, I.; Law, W. C.; Bergey, E. J.; Maitra, A.; Prasad, P. N., *ACS Nano* **2009,** 3, 502.

10. Ziegler, J.; Xu, S.; Kucur, E.; Meister, F.; Batentschuk, M.; Gindele, F.; Nann, T., *Adv. Mater.* **2008,** 20, 4068.

11. Yang, X. Y.; Zhao, D. W.; Leck, K. S.; Tan, S. T.; Tang, Y. X.; Zhao, J. L.; Demir, H. V.; Sun, X. W., *Adv. Mater.* **2012,** 24, 4180.

12. Dorfs, D.; Salant, A.; Popov, I.; Banin, U., *Small* **2008,** 4, 1319.

13. Talapin, D. V.; Nelson, J. H.; Shevchenko, E. V.; Aloni, S.; Sadtler, B.; Alivisatos, A. P., *Nano Lett.* **2007,** 7, 2951.

14. Manna, L.; Milliron, D. J.; Meisel, A.; Scher, E. C.; Alivisatos, A. P., *Nat. Mater.* **2003,** 2, 382.

15. Milliron, D. J.; Hughes, S. M.; Cui, Y.; Manna, L.; Li, J. B.; Wang, L. W.; Alivisatos, A. P., *Nature* **2004,** 430, 190.

16. Carbone, L.; Nobile, C.; De Giorgi, M.; Sala, F. D.; Morello, G.; Pompa, P.; Hytch, M.; Snoeck, E.; Fiore, A.; Franchini, I. R.; Nadasan, M.; Silvestre, A. F.; Chiodo, L.; Kudera, S.; Cingolani, R.; Krahne, R.; Manna, L., *Nano Lett.* **2007,** 7, 2942.

17. Fiore, A.; Mastria, R.; Lupo, M. G.; Lanzani, G.; Giannini, C.; Carlino, E.; Morello, G.; De Giorgi, M.; Li, Y.; Cingolani, R.; Manna, L., *J. Am. Chem. Soc.* **2009,** 131, 2274.

18. Yu, H.; Li, J. B.; Loomis, R. A.; Wang, L. W.; Buhro, W. E., *Nat. Mater.* **2003,** 2, 517.

19. Kan, S.; Mokari, T.; Rothenberg, E.; Banin, U., *Nat. Mater.* **2004,** 3, 72.

20. Ahrenkiel, S. P.; Micic, O. I.; Miedaner, A.; Curtis, C. J.; Nedeljkovic, J. M.; Nozik, A. J., *Nano Lett.* **2003,** 3, 833.

21. Shweky, I.; Aharoni, A.; Mokari, T.; Rothenberg, E.; Nadler, M.; Podov, I.; Banin, U., *Mater. Sci. Eng. C-Biomimetic Supramol. Syst.* **2006,** 26, 788.

22. Wang, F. D.; Buhro, W. E.,. *J. Am. Chem. Soc.* **2007,** 129, 14381.

23. Trentler, T. J.; Hickman, K. M.; Goel, S. C.; Viano, A. M.; Gibbons, P. C.; Buhro, W. E., *Science* **1995,** 270, 1791.

24. Holmes, J. D.; Johnston, K. P.; Doty, R. C.; Korgel, B. A., *Science* **2000,** 287, 1471.

25. Van de Walle, C. G.; Neugebauer, J., *Nature* **2003,** 423, 626.

26. Shaviv, E.; Schubert, O.; Alves-Santos, M.; Goldoni, G.; Di Felice, R.; Vallee, F.; Del Fatti, N.; Banin, U.; Sonnichsen, C., *ACS Nano* **2011,** 5, 4712.

27. Li, L.; Reiss, P., *J. Am. Chem. Soc.* **2008,** 130, 11588.

28. Ung, T. D. T.; Pham, T. T.; Nguyen, Q. L.; Li, L.; Reiss, P., *Appl. Phys. Lett.* **2010,** 96, 073102.

29. Ung, T. D. T.; Reiss, P.; Nguyen, Q. L., *Appl. Phys. Lett.* **2010,** 97, 193104.

30. Dennis, A. M.; Mangum, B. D.; Piryatinski, A.; Park, Y. S.; Hannah, D. C.; Casson, J. L.; Williams, D. J.; Schaller, R. D.; Htoon, H.; Hollingsworth, J. A., *Nano Lett.* **2012,** 12, 5545.

31. Son, D. H.; Hughes, S. M.; Yin, Y. D.; Alivisatos, A. P., *Science* **2004,** 306, 1009.

32. Zhang, J. T.; Tang, Y.; Lee, K.; Min, O. Y., *Science* **2010,** 327, 1634.

33. Li, H. B.; Zanella, M.; Genovese, A.; Povia, M.; Falqui, A.; Giannini, C.; Manna, L., *Nano Lett.* **2011,** 11, 4964.

34. Luther, J. M.; Zheng, H. M.; Sadtler, B.; Alivisatos, A. P., *J. Am. Chem. Soc.* **2009,** 131, 16851.

35. Mocatta, D.; Cohen, G.; Schattner, J.; Millo, O.; Rabani, E.; Banin, U., *Science* **2011,** 332, 77.

36. Du, Y. P.; Xu, B.; Fu, T.; Cai, M.; Li, F.; Zhang, Y.; Wang, Q. B., *J. Am. Chem. Soc.* **2010,** 132, 1470.

37. Li, H.; Brescia, R.; Krahne, R.; Bertoni, G.; Alcocer, M. J. P.; D'Andrea, C.; Scotognella, F.; Tassone, F.; Zanella, M.; De Giorgi, M.; Manna, L., *ACS Nano* **2012,** 6, 1637.

38. Lian, J.; Xu, Y.; Lin, M.; Chan, Y. T., *J. Am. Chem. Soc.* **2012,** 134, 8754.

39. Jain, P. K.; Beberwyck, B. J.; Fong, L. K.; Polking, M. J.; Alivisatos, A. P., *Angew. Chem.-Int. Edit.* **2012,** 51, 2387.

CHAPTER 4

Promoting 2D Growth in Transition Metal Sulfide Semiconductor Nanostructures via Halide Ions

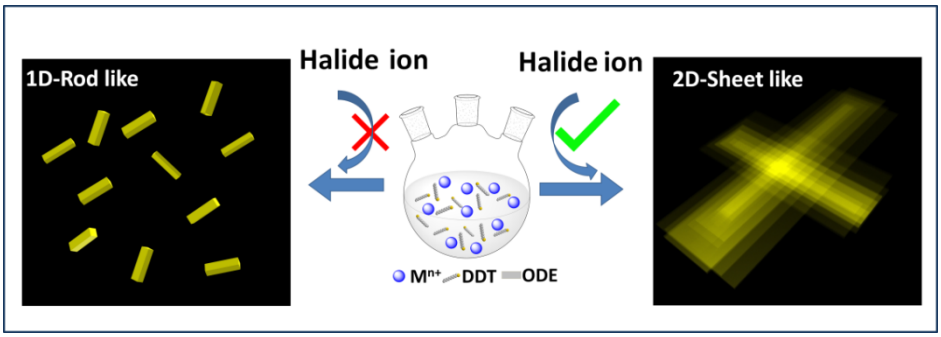

4.1 Introduction

Free-standing semiconductor nanostructures whose physical dimensions are restricted to a plane have recently garnered a tremendous amount of interest due to their unique physicochemical properties that are markedly different from their bulk, zero- and one-dimensional nanocrystal counterparts.[1, 2] For example, colloidal CdSe nanoplatelets were found to possess radiative lifetimes around two orders of magnitude faster than CdSe quantum dots of comparable emission wavelength and quantum yield at low temperature[3] whereas as-synthesized PbS nanosheets (NS) were able to achieve conductivity values higher than untreated films of PbS quantum dots.[4] However, in comparison with their spherical nanoparticle analogues, disk- or sheet-like semiconductor nanostructures have received much less attention, and a firm understanding of the parameters and reactions conditions that yield two-dimensional (2D) growth is at the present time not well established.

To date, a number of disk-, sheet- or ribbon-like colloidal semiconductor nanostructures such as SnSe, GeSe, CdSe, CdTe, CuS, PbS, and FeS_2 have been synthesized via wet-chemical approaches.[5] In nearly all of the syntheses of these materials, the use of long chain carboxylic acids (e.g. oleic or myristic acid) and/or primary amines (e.g. oleylamine or octylamine) were employed as surfactants.[6-8] Aside from their role as strong binding surface ligands,[9] it has been suggested that these molecules can serve as "soft" templates to support growth in the lateral direction.[10-12] The molecular structure of the precursor was found to facilitate sheet-like growth, as evidenced by single source precursors used to produce SnS,[13] MoS_2,[14] In_2S_3 nanosheets.[15] Additionally, the use of metal chelating molecules were found to

aid in ultrathin semiconductor sheet formation as well by modifying its growth kinetics.[16]

We show in this work that the presence of halides can also play a pivotal role in facilitating the sheet-like growth of non-layered semiconductor nanostructures, and the dimensionality of the synthesized nanostructure can be tuned from 0D to 2D by simply varying the concentration of halide ions added to the reaction. This was attributed to the reduction in the rates of nucleation and growth due to the formation of metal halide bonds which in turn lowered the rate of formation of metal thiolates. Nickel sulfide was identified as a choice material given its utility as a electrocatalyst,[17] electrode[18] and battery material.[19] Although it may be envisaged that an ultrathin and planar nickel sulfide morphology would be beneficial for such applications, there have been very few, if any, reports on the synthesis of colloidal nickel sulfide nanosheets via hot injection methods. We describe a novel synthesis route for the production of nickel sulfide nanosheets with lateral dimensions on the order of ~ 100 – 1000 nm with thicknesses down to ~ 4 nm. The use of halides to foster sheet-like growth was found to be applicable to Cu_2S as well, where triangular nanosheets with edge lengths ~ 120 nm long and an average thickness of ~ 1.7 nm were routinely achieved. The results described in this work collectively exemplified the use of halides in promoting lateral growth in transition metal sulfide nanostructures and added to the growing synthetic toolkit for synthesizing colloidal two-dimensional nanomaterials.

4.2 Experimental section

4.2.1 Synthesis of nanosheets

Chemicals and materials

Nickel (II) acetate tetrahydrate ($Ni(Ac)_2.4H_2O$, 99.9%), nickel (II) chloride ($NiCl_2$, 99%), nickel (II) bromide ($NiBr_2$, 99%), nickel (II) iodide (NiI_2, 99%), copper (I) chloride (CuCl, 99.99%), copper (II) acetate ($Cu(AC)_2$, 99%), copper (I) bromide (CuBr, 99%), copper (I) iodide (CuI, 99%), hydrochloride acid (HCl, 37% w/w), 1-octadecene (ODE, 90%), trioctylphosphine oxide (TOPO, 99%), 1-dodecanethiol (1-DDT, 97%), sulfur (S, reagent grade), were purchased from Sigma Aldrich. All the chemicals were used as received without further purification. Unless stated otherwise, all reactions were conducted in oven-dried glassware under nitrogen atmosphere using standard Schlenk techniques.

Synthesis of Ni_9S_8 nanosheets

Briefly, $Ni(Ac)_2.4H_2O$ (0.4 mmol), HCl (0.8 mmol), TOPO (2.5 mmol), ODE (20 mL) were mixed in a round bottom 3-neck flask (RBF) at room temperature. The mixture was kept stirring under N_2 flow for 15 min before degassed under vacuum at 90 ℃ for 1 hour. Then rapidly heat the reaction pot to the target growth temperature of 250 ℃. When the temperature reached 160 ℃ during the heating process, 1-DDT (4 mmol) was swiftly injected into the reaction flask and this mixture was kept under heat at 250 ℃ for 1 hr. This yielded cross-shaped Ni_9S_8 sheet-like structures with thickness of ~30 - 40 nm and lateral dimensions of about 250 - 300 nm., For further purification, the reaction mixture was cooled to room temperature, where 1 equivalent of

toluene and 8 equivalents of ethanol were added to 1 equivalent of the growth solution, followed by centrifugation at 3900 rpm for 3 min. The resulting precipitate was further processed via two cycles of dispersion in toluene and precipitation in ethanol. The resulting NCs were then dispersed in toluene and sonicated for ~1 hour for subsequent use.

Effect of chloride ion concentration on morphology of Ni_9S_8 nanostructures

To demonstrate the effect of chloride ion concentration on the morphology of Ni_9S_8 structures, we varied the amount of HCl added (0 mmol, 0.4 mmol, 0.8 mmol, 1.0 mmol), while keeping all other reaction parameters constant. This yielded Ni_9S_8 small rods (0 mmol Cl^-), rectangular plate-like structures less than 100 nm in their lateral dimensions (0.4 mmol Cl^-), and cross sheet-like structures with lateral dimensions of 300 – 400 nm (0.8 and 1.0 mmol Cl^-) respectively with continuous increasing of the chloride ion concentration. To isolate the product, we employed the same procedure as described above for Ni_9S_8 nanosheets.

Synthesis of Cu_2S nanosheets

Briefly, $Cu(Ac)_2$ (0.4 mmol), TOPO (2.5 mmol), ODE (20 mL), HCl (0.4 mmol) were degassed under vacuum at 90 ℃ in a round bottom 3-neck flask for 1 hour. 1-DDT (4 mmol) was then swiftly injected into the reaction flask at 160℃, upon which the mixture was kept on heating up until the growth temperature of 200 ℃ ~210 ℃ and then kept for 1 hour or more. This yielded Cu_2S sheets with thickness of 1.7 nm and lateral dimension reach about 130nm. For further purification, the reaction mixture was cooled to room temperature, where 1 equivalent of toluene and 8 equivalents of ethanol was added to 1 equivalent of raw solution, followed by centrifugation at 3900

rpm for 3 min. The resulting precipitate was processed twice via toluene-ethanol mixture. The processed NCs were then dispersed in toluene and sonicated for 1 hour (or longer if necessary) for subsequent use.

Effect of chloride ion concentration on morphology of Cu_2S nanostructures

To demonstrate the effect of chloride ion on the morphology of the synthesized Cu_2S nanostructures, we varied the amount of HCl added (0 mmol, 0.08 mmol, 0.2 mmol, 0.4 mmol), while keeping all other reaction parameters constant. This yielded Cu_2S spheres (0 mmol Cl^-), discs (0.08mmol Cl^-), and nanosheets (0.2 and 0.4 mmol Cl^-) respectively with continuous increasing of the chloride ion concentration. To isolate the products, we employed the same procedure for Cu_2S nanosheets as described above.

Use of other metal halide salts

In order to study the effects of other halide groups, other MX_n salts were used (M = Cu, Ni ; X = Br, I). Unless otherwise stated, the synthesis conditions were identical to those described above for the synthesis of Cu_2S and Ni_9S_8 nanosheets.

4.2.2 Structural characterization

Transmission Electron Microscopy (TEM)

A JEOL JEM 1220F (100 kV accelerating voltage) microscope was used to obtain bright field TEM images of the nanoparticles. For TEM sample preparation, a drop of the nanoparticle solution was placed onto a 300 mesh copper grid covered with a continuous carbon film. Excess solution was removed by an adsorbent paper and the sample was dried at room temperature. The High-Resolution TEM images and detailed elemental analysis were

carried out on a FEI Titan 80-300 electron microscope (operated at 200 KV) which is equipped with an electron beam monochromator, an energy dispersive X-ray spectroscopy (EDX) and a Gatan electron energy loss spectrometer. The probing electron beam size for point EDX measurements was around 0.3 nm. The dwell time for each EDX spectrum was about 10 s.

X-Ray Diffraction (XRD)

XRD data was obtained with a diffractometer (Bruker AXS, GADDS) using Cu-Kα radiation (λ=1.540598Å) in the range of 20˚ to 80˚. Thin film samples were prepared on a clean silicon wafer by placing several drops of concentrated nanoparticle samples in hexane on the silicon surface and dried at 60 ℃ in the oven. This was repeated several times until a thin layer of solid was formed on the silicon substrate. The powder form of XRD samples were prepared by several times of purification followed by drying under N_2.

Elemental Analysis

For Nickel and Copper determination: Dual-view Optima 5300 DV ICP-OES system.

For elemental Sulphur determination: Elementar Vario Micro Cube.

For anion (Cl^-, Br^-): Ion Chromatography (IC) Analysis, Instrumentation includes 818 IC Pump, 820 Separation Center, 830 Interface, 833 Liquid handling Unit, 732 Detector and 813 Compact Autosampler.

Atomic Force Microscope (AFM)

We recorded the AFM data via a Bruker Dimension FastScan AFM operating in tapping mode (FASTSCAN-A). We used the software named "WSxM 5.0 Develop 4.3" to determine the height profile of the sheet-like structures which were deposited onto the silicon substrates.

4.2.3 Optical characterization

Absorption spectra were obtained with an Agilent 8453 UV-Visible spectrophotometer using a quartz cuvette with a path length of 1 cm.

4.3 Results and discussions

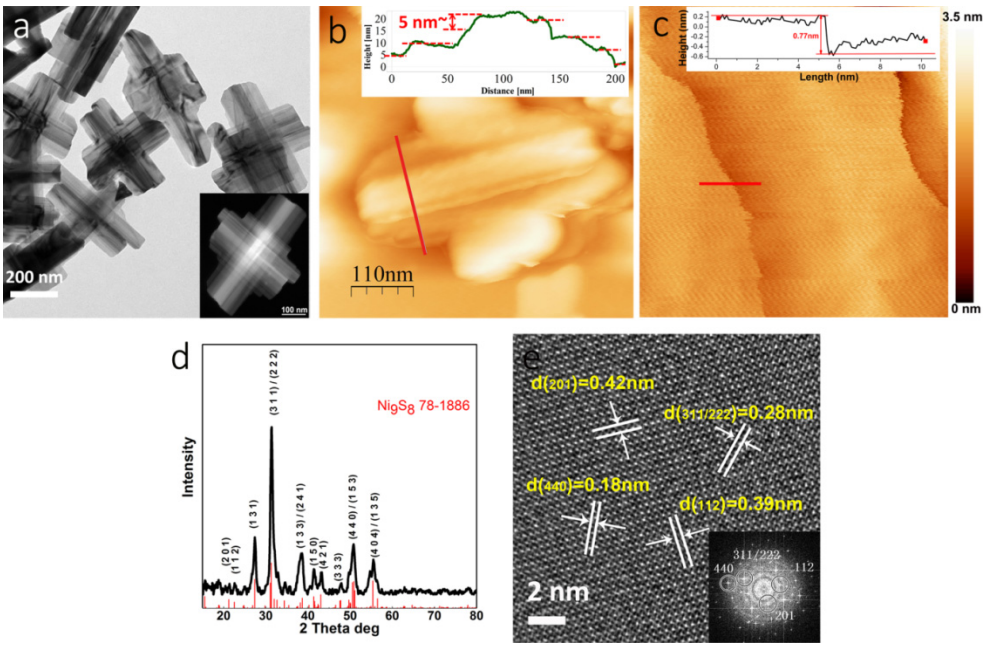

Figure 4.1 Structrual characterization of Ni_9S_8. (a) TEM image of cross-like nickel sulfide nanosheets formed in the presence of Cl^- ions. The inset is a HAADF-STEM image illustrating its step-terrace morphology; (b) AFM image showing thickness of each step-terrace is ~ 5 nm; (c) a zoom-in AFM image which shows a series of step-edges on the synthesized Ni9S¬8 nanosheets, height profile across a typical step-edge, which shows that the average thickness of each step is around ~ 0.8 nm; (d) XRD pattern of nanosheets with reference Ni_9S_8 (78-1886) peaks in red; (e) HRTEM of the Ni_9S_8 lateral plane.

Figure 4.1(a) is a typical transmission electron microscope (TEM) image of nickel sulfide nanosheets synthesized, where an unusual cross-like shape with lateral dimensions on the order of hundreds of nm is apparent. The step-terrace morphology of the nanosheets can be visualized more readily via High Angle Annular Dark Field STEM (HAADF-STEM) image, which is illustrated in the inset in **Figure 4.1(a)**. Characterization via atomic force

microscopy (AFM), as exemplified in **Figure 4.1(b)**, showed that the thickness of each step-terrace is ~ 5 nm with multiple step-like edges (see **Figure 4.1(c)**). Powder X-ray diffraction (XRD) measurements as illustrated in **Figure 4.1(d)** confirmed the crystal structure to be that of Ni_9S_8, which is a non-stoichiometric form of nickel sulfide that has not to the best of our knowledge been synthesized in the form of a nanosheet. Elemental analysis via Energy-dispersive X-ray spectroscopy (EDX) revealed a Ni to S ratio of 9:7.7, which is in good agreement with the formula Ni_9S_8. High-resolution TEM (HRTEM) analysis of the nanosheets obtained, as shown in **Figure 4.1(e)**, yielded lattice spacing consistent with that of Ni_9S_8, lending further support to its proposed identity.

The unusual cross-like morphology of the Ni_9S_8 structures observed may be visualized as a nanosheet with four wings each oriented at right angles to each other. **Figure 4.2(a)** is a zoomed-in TEM image of a single Ni_9S_8 nanocross oriented along [010] zone axis. From the corresponding diffraction pattern shown in **Figure 4.2(b)**, it may be deduced that the four wings of this single crystalline nanosheet are extended along the <101> direction. By considering the shape morphology of individual sheets within each sample, it was inferred that the order of the growth rate for the various planes follows as {101}>{001}≈{100}>>{010}. The slowest growth rate along the <010> direction results in primarily lateral growth into a sheet-like structure with exposed {010} facets at its top and bottom. **Figure 4.2(c)** is a simulated cross-sectional view of the Ni_9S_8 cell lattice from the

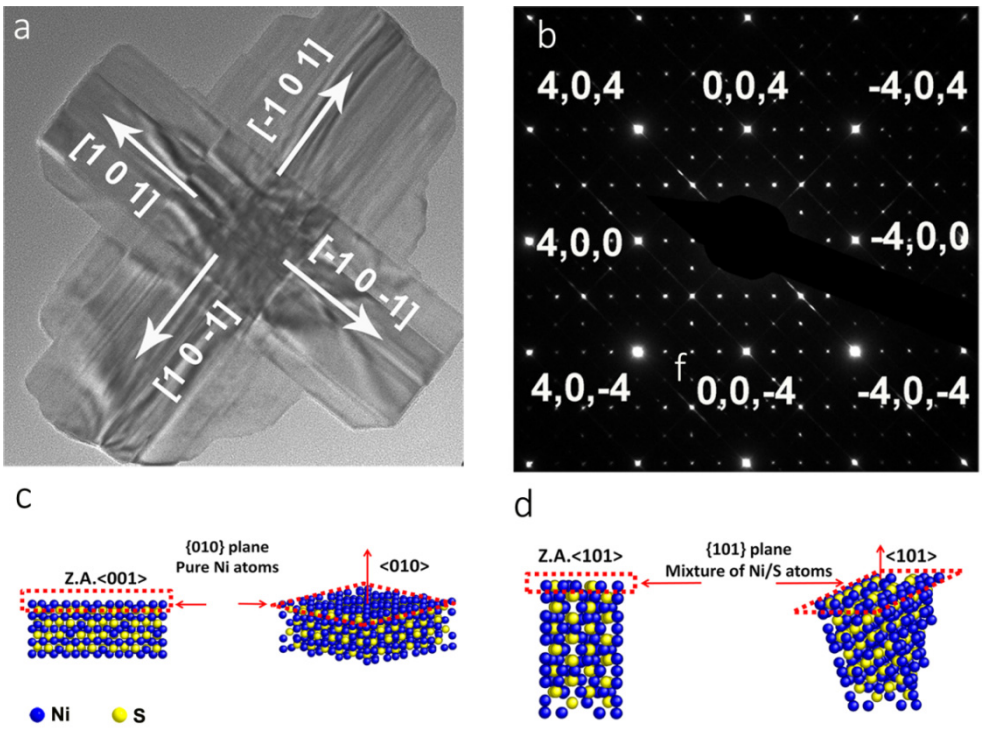

Figure 4.2 Diffraction pattern on single Ni_9S_8 nanosheet. (a) TEM image of a single Ni_9S_8 nanocrystal; (b) corresponding diffraction pattern. Schematic drawing of Ni_9S_8 unit cells viewed along: (c) the [001] direction showing the alternating layers of Ni and S atoms; (d) the [101] direction showing a mixture of Ni and S atoms.

<001> zone axis where it is seen that the {010} planes comprise of alternating layers of Ni and S atoms. On the other hand, each {101} plane comprises of a mixed number of Ni and S atoms, as seen in **Figure 4.2(d)**. This is consistent with our inference that the growth rate for the {101} facets is larger than that of {010} since it is expected that the DDT would inhibit the rate of monomer addition on the {010} facets by binding strongly to exposed Ni sites during growth. Conversely, one would expect less binding of DDT to the {101} facets which would result in faster growth.

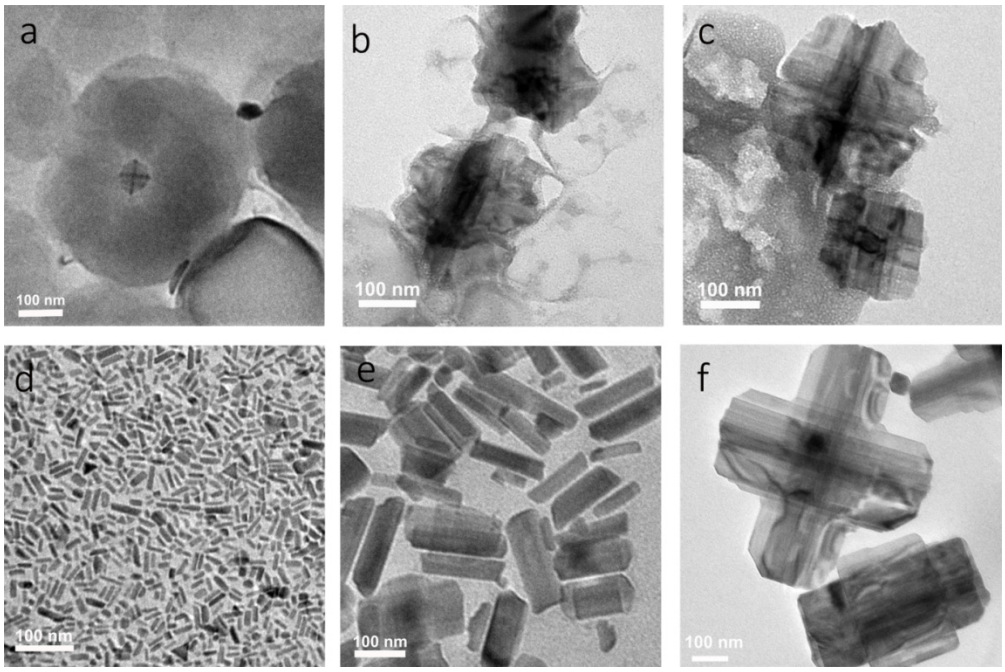

Figure 4.3 Growth evolution of Ni_9S_8 nanocrystals from (a) 230 ^oC, (b) 250 ^oC, (c) maintained at 250 ^oC for 5 min. Resulting Ni_9S_8 structures from use of: (d) 0 mmol of Cl^-; (e) 0.4 mmol of Cl^-; (f) 1 mmol of Cl^- at T = 250 ^oC.

The growth evolution of the nanosheets as a function of time was investigated by taking aliquots at different stages of the reaction and characterizing via TEM. At a Ni:Cl molar ratio of 1:2 and a reaction temperature of T = 230 ℃, sample aliquots yielded dense stacks of pre-formed intermediate films. Within these films, small plate-like crystals of Ni_9S_8 were seen, as illustrated in **Figure 4.3(a)**. When the reaction temperature had reached 250 ℃ with a growth time of ~ t = 1-2 min, consumption of the preformed films commensurate with growth of the plate-like structures into irregular thin sheets was evident, as shown in **Figure 4.3(b)**. Continued growth resulted in the formation of square-like nanosheets, as exemplified in **Figure 4.3(c)**, along with additional consumption of the intermediate film. Further growth at this temperature yielded the cross-like nanostructures shown in **Figure 4.1(a)**, with a near complete disappearance of the intermediate films.

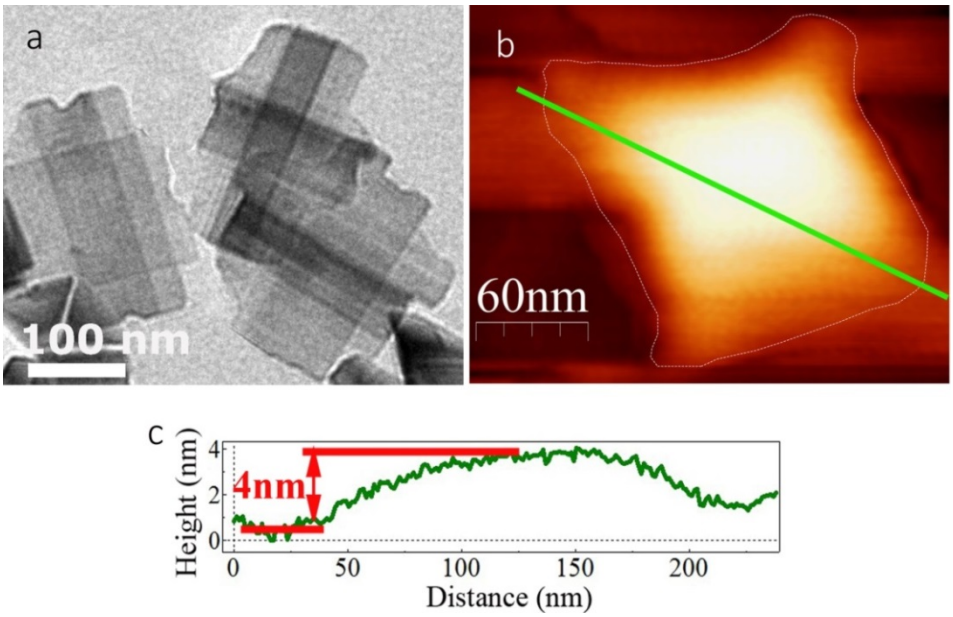

Figure 4.4 Ni_9S_8 nanosheets obtained at lower Ni(II) precursor concentration. (a) TEM image of the Ni_9S_8 sheet; (b) AFM image of a single Ni_9S_8 sheet; (c) Height profile across the green line in (b) showing that the height is around 4 nm.

The effect of the Cl^- concentration on the growth of the Ni_9S_8 nanostructures was also investigated by varying the amount of Cl^- added, fixing the reaction temperature at 250 ℃ and keeping all other parameters constant. When no Cl^- was added, nucleation and growth of the particles were completed within ~ 1 min, yielding short rod-like particles as shown in **Figure 4.3(d)**. Interestingly, a preformed, crystalline film comprising of Ni and S was also observed at early reaction times even though no Cl^- was added. At a Ni:Cl molar ratio of 1:1, the particles obtained were larger with a shape similar to that of a rectangular slab (**Figure 4.3(e)**), and took 25 ~ 30 mins for the pre-formed intermediate film to be entirely consumed. A Ni:Cl molar ratio of 1:2 yielded the nanosheets shown earlier in **Figure 4.1(a)** while even larger amounts of Cl^- added required much longer reaction times and caused larger cross-like sheets with thicknesses on the order of 100 nm to form, as

illustrated in **Figure 4.3(f)**. On the other hand, reducing the concentration of nickel precursor in the reaction flask while keeping the Ni to Cl^- ratio at 1:2 allows for the formation of the same sheet-like structure with lateral dimensions of ~ 200 nm but with a thickness of ~ 4 nm, which corresponds to a height of about 3 unit cells (**see Figure 4.4**).

The observations obtained from the above experiments afforded considerable insight into the mechanism of growth of Ni_9S_8 into nanosheets in the presence of Cl^-. It was previously reported that Ni(II) dodecanethiolate $[Ni_x(C_{12}H_{25}S)_z]$ can form a layered film structure,[20] although as indicated by our experiments, this condition is not sufficient to obtain ultrathin nanosheets. Within our reaction conditions, $Ni(Ac)_2$ can undergo nucleophilic substitution by both Cl^- and $C_{12}H_{25}S^-$, and an equilibrium is set up between the two different Ni(II) species formed. HAADF-STEM and EDX analysis of the preformed films which yielded Ni_9S_8 nanocrosses revealed the presence of Ni, S and Cl in an approximate atomic ratio of 1 : 0.4 : 1.6, as illustrated in **Figures 4.5(a)** and **4.5(b)**. These ratios are consistent with those obtained

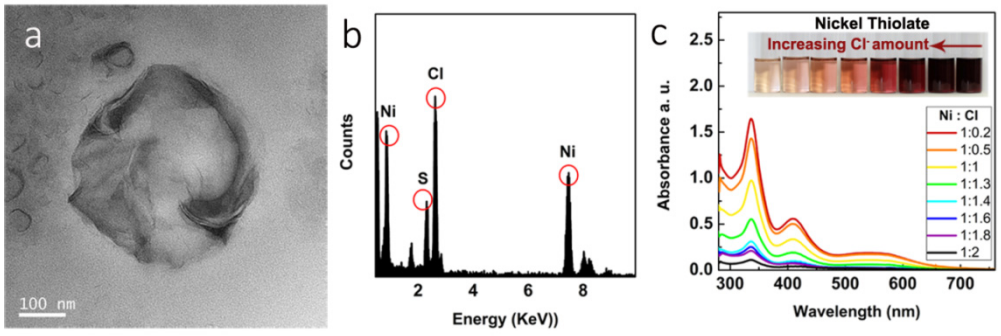

Figure 4.5 (a) TEM image of the $[Ni_x(C_{12}H_{25}S)_z]$ intermediate preformed film; (b) corresponding EDX giving a Ni:Cl:S ratio of 1:1.6:0.4; (c) UV-Vis spectra of the supernatant after injection of a fixed amount of 1-DDT at 160 °C for different Ni to Cl^- ratios; the inset is a digital photo showing the intensity of the color reducing upon increasing amounts of Cl^- introduced into the reaction system.

via Inductively Coupled Plasma Atomic Absorption Spectroscopy (ICP-AAS), suggesting that the films have a relatively uniform composition. It may be inferred from the elemental analyses conducted that the majority of bonds formed are that of Ni-Cl instead of Ni-S, and that the addition of Cl^- results in a lower amount of Ni(II) thiolate produced. In order to ascertain this, UV-Vis spectroscopy of the preformed films exposed to different concentrations of Cl^- was carried out, as shown in **Figure 4.5(c)**, and it is readily seen that the characteristic absorbance of Ni(II) thiolate decreases as higher amounts of Cl^- were added.

In the absence of Cl^-, nucleation and growth of the Ni_9S_8 nanostructures from the breakdown of Ni(II) thiolate precursors occurs at a rapid rate, whereas the addition of Cl^- results in the formation of Ni-Cl bonds and a concurrent reduction in the rate of $Ni(C_{12}H_{25}S)_2$ produced. Indeed, the use of $NiCl_2$ as a starting precursor instead of $Ni(Ac)_2$ gives essentially identical results in terms of nanostructures and intermediates produced, corroborating the reaction pathway proposed above. These findings strongly indicate that in addition to DDT acting as a strong binding ligand to the {010} basal plane of Ni_9S_8, slow growth kinetics is critical for the formation of nanosheets while fast growth kinetics yields sphere-like nanoparticles, as indicated in **Figure 4.2(c)**. The slow displacement of Cl^- by $C_{12}H_{25}S^-$ in the intermediate film resulted in less nickel sulfide nuclei and longer growth time, which ultimately led to the formation of thermodynamically stable nanosheets. There is also a strong possibility that in addition to $Ni(II)(C_{12}H_{25}S)_2$, $NiCl_2$ is also known to adopt a layered structure,[21] which can provide further impetus for sheet formation. TOPO in the synthesized nanosheets was not detected by

EDX, suggesting that it has little affinity for the Ni_9S_8 surface. While the primary role of TOPO may not be that of a strong binding ligand, removing TOPO from the reaction resulted in very large irregular sheet-like structures. This implies that TOPO accelerates the nucleation process, possibly by extracting Ni^{2+} from its salt given its capability for the solvent extraction of metals.[22]

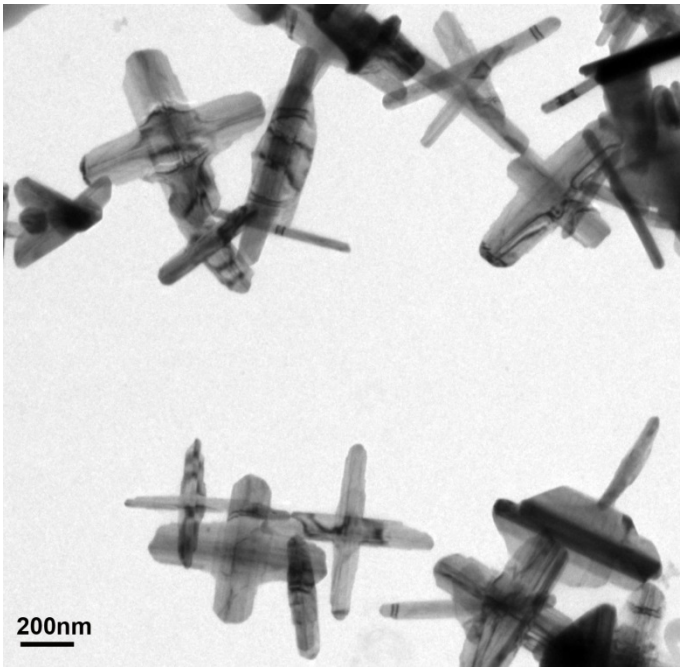

Figure 4.6 Low resolution TEM image of Ni_9S_8 nanostructures obtained via using $NiBr_2$ as the precursor, where all the other parameters were kept the same as that of the synthesis with Cl^-, with the sole exception that the growth temperature was set at 265 - 270 ℃. The resulting nanocrystals are several times larger in dimensions and with a poorer size distribution compared with those using Cl^-, but clearly exhibit a cross-like sheet morphology.

Aside from Cl, the presence of Br or I groups also facilitated the growth of cross-like Ni_9S_8 nanosheets, although it should be mentioned that reaction times were increased significantly with the use of $NiBr_2$ and NiI_2 as precursors. Raising the reaction temperature allowed for the reaction to be completed within 1 hour, but led to larger structures with the same morphology as those synthesized in the presence Cl^- (see **Figure 4.6**). If TR is

the time required for the reaction to go to completion, then TR (I^-) > TR (Br^-) > TR (Cl^-) at the same reaction temperature. The main difference in reaction rates associated with the use of these different precursors may primarily be attributed to the relative rates of substitution of the different halide groups with dodecanethiolate. The observed trend in reaction times cannot be rationalized by analyzing the relative nickel halide bond enthalpies[23] or nucleophilicities of the halides in comparison with thiolates in an aprotic solvent,[24] given that they both predict an opposite trend. This conundrum can be resolved by considering that the nucleophilic substitution reactions take place in a preformed intermediate film rather than with free metal halide molecules so that steric hindrance caused by bulky halide groups can prevent access to the Ni center and slow down the rate of $Ni(C_{12}H_{25}S)_2$ produced.

In the case of Ni_9S_8, lateral growth was mediated by the modification of growth kinetics caused by competition between the formation of nickel thiolates and nickel halides. We hypothesized that this approach to 2D growth may be applicable to other transition metal sulfides. To this end, we choose Cu_2S as our target, which is a p-type semiconductor with a bulk band gap of 1.2 eV and has potential utility as an active material in solar cells[25] and non-volatile memory devices.[26] Unlike in the case of Ni_9S_8, however, the formation of two-dimensional Cu_2S nanostructures has been suggested to occur via the decomposition of Cu(I) thiolate complexes in a columnar mesophase at elevated temperature.[27-30] It was previously reported that the morphology of Cu_2S nanostructures could be varied from disk- to sheet-like by introducing ligands of different chain lengths in a solventless reaction system, but the structures synthesized had a tendency to be fairly polydisperse.[30] The use of

$Sn(acac)_2Cl_2$ and $SnCl_4$ were also found to induce lateral growth in Cu_2S, however the structures formed were relatively thick with a diameter to thickness ratio of ~ 6.[31] By employing reaction conditions similar to the synthesis of Ni_9S_8 nanoplates, Cu_2S nanostructures with an average edge length of ~123.0 ± 26.5 nm and thickness of ~1.7 ± 0.2 nm (giving an edge length to thickness ratio of 72) were successfully derived. Briefly, copper acetate ($Cu(Ac)_2$), TOPO, ODE and HCl were degassed under vacuum at 90 ℃ for 2 hours before the swift injection of DDT at 160 ^oC under N_2. The growth temperature was raised to 200 ℃ for 1 hour before workup. **Figure 4.7(a)** is a typical TEM image of the Cu_2S nanosheets synthesized by using 0.2 mmol of Cl^-, which have lateral dimensions on the order of ~ 50 nm and a measured thickness of ~2 nm (via side view of TEM). Structural characterization via XRD confirmed that the nanosheets obtained were that of β-Cu_2S with a hexagonal crystal phase, as illustrated in **Figure 4.7(b)**. **Figures 4.7(c)** is the corresponding HRTEM image showing a d-spacing of 0.198 nm, which agrees well with the (110) lattice spacing of Cu_2S.The side view HRTEM (see **Figure 4.7(d)**) and structural analysis of individual sheet using diffraction pattern shows triangular Cu_2S nanosheets are of single crystalline nature, terminated by three identical {100} side planes and two {002} lateral surfaces. Interestingly, similar to Ni_9S_8 nanosheets, the two lateral {002} surfaces of Cu_2S are also terminated by pure Cu and S atoms respectively. The fact that the use of a Cu(II) salt did not result in CuS but consistently yielded Cu_2S may be explicated by the presence of Cl^- and excess DDT which are known to be mildly reducing.[32, 33]

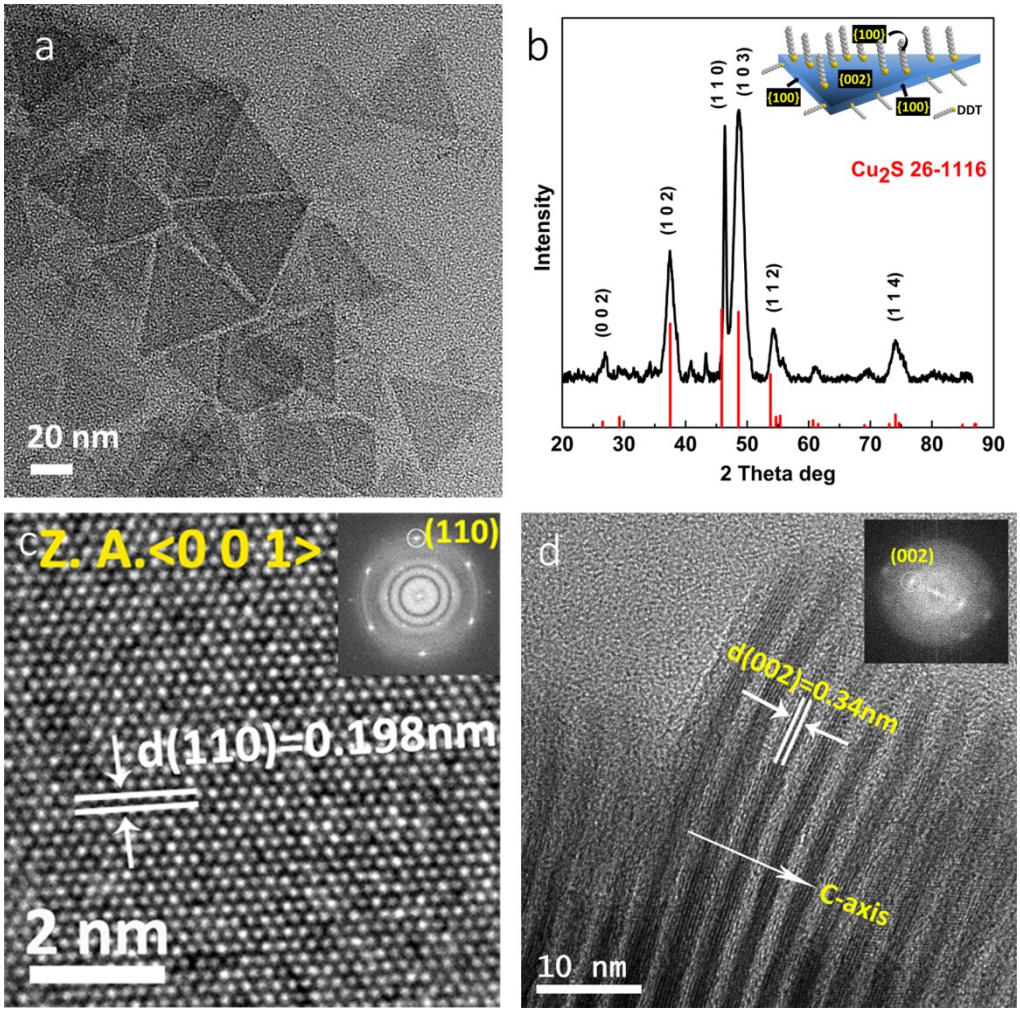

Figure 4.7 (a) Cu_2S ultrathin triangular sheets synthesized in the presence of Cl^-; (b) XRD of Cu_2S, inset is a cartoon showing that the three exposed edges are identical {1 0 0} facets and the top/down is the {0 0 2} plane; (c) HRTEM showing lattice spacings consistent with Cu_2S; (d) Corresponding HRTEM image of the same sample, showing a lattice d-spacing of 0.34 nm which represents the (0 0 2) plane. Inset shows the FFT of the selected area where the (0 0 2) plane spot in the pattern is clearly evident.

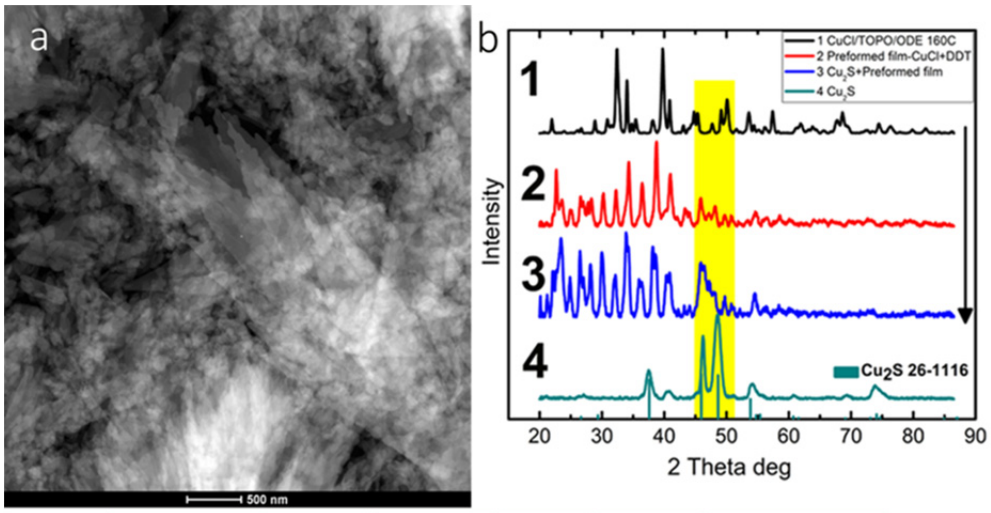

C

Elemental Analysis	Cu (w%)	S (w%)	Cl^- (w%)	Br^- (w%)	Cu:S:Halide (mol)
Preformed film (Cl^-)	18.86%	11.27%	1.30%		1:0.83:0.11
Preformed film (Br^-)	23.79%	9.86%		1.43%	1:1.2:0.12

Figure 4.8 (a) HAADF-STEM image of a preformed film comprising of Cu, S and Cl. Consumption of the film eventually leads to the nucleation and growth of Cu_2S nanosheets; (b) The evolution of XRD from (1) $CuCl.H_2O$ (2) the preformed film after DDT injection to the pot, when the growth temperature was at 200 ℃, (3) the Cu_2S nanosheet in co-existence with the preformed film of Cu_2S, to (4) the final Cu_2S nanosheet. (All samples were prepared in powder form). (c) Table SI: Elemental analysis on preformed film made via Cu : Cl^- /Br^- = 1:1.

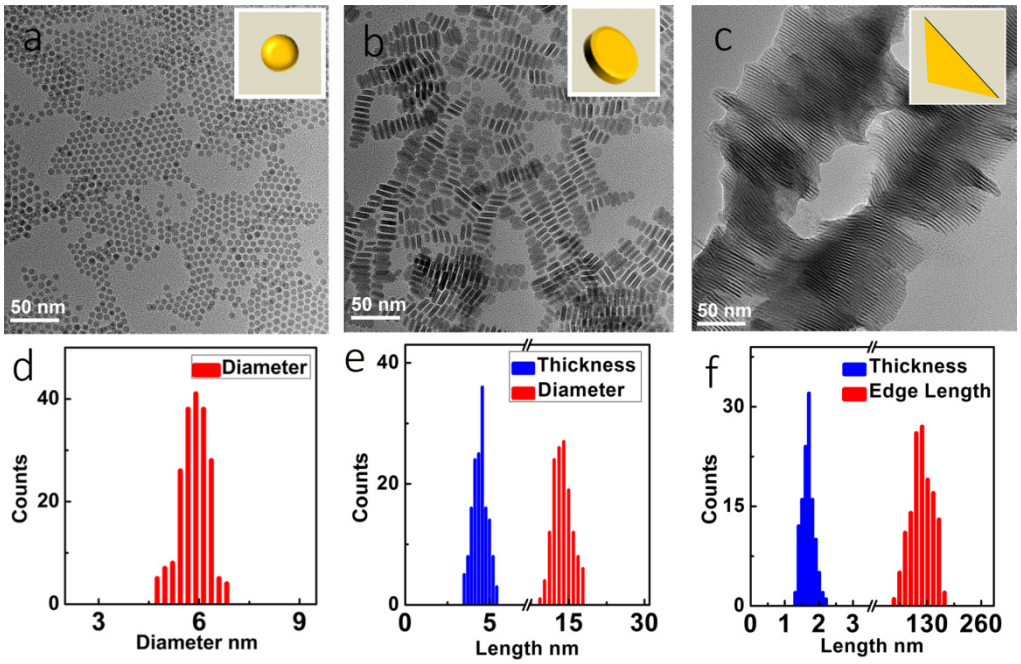

Figure 4.9 Cl^- effect on tuning the morphology of Cu_2S nanocrystal. (a) copper sulfide discs using $Cu(Ac)_2$ as the copper precursor with all other reaction conditions unchanged; (b), (c) are the same as the (a) but with different amounts of Cl^- introduced by addition of HCl (Cl^-: 0.08 mmol, 0.4 mmol for (b) and (c) respectively). Corresponding size histograms for (a)-(c) are presented in (d): diameter = 5.97 ± 0.43 nm; (e) thickness = 4.53 ± 0.44 nm, edge length = 14.15 ± 1.87 nm; (f) Thickness = 1.732 ± 0.18 nm, edge length = 123.13 ± 26.5 nm.

Analogous to the formation of the Ni_9S_8 nanosheets, a crystalline intermediate film comprising of Cu, S and Cl was present at early reaction stage (see **Figure 4.8**). Upon nucleation and growth of Cu_2S, consumption of the intermediate film became evident. Increasing the concentration of Cl^- added resulted in a progressive change towards a sheet-like morphology as depicted in **Figures 4.9(a) – (c)**, where relatively monodisperse spheres, disks and sheets are shown respectively. Notably, the ability to continuously tune particle morphology from 0D to 2D by simply varying the concentration of Cl^- added while keeping other parameters the same affords a facile and convenient synthetic route to deriving Cu_2S nanostructures with different degrees of quantum confinement.

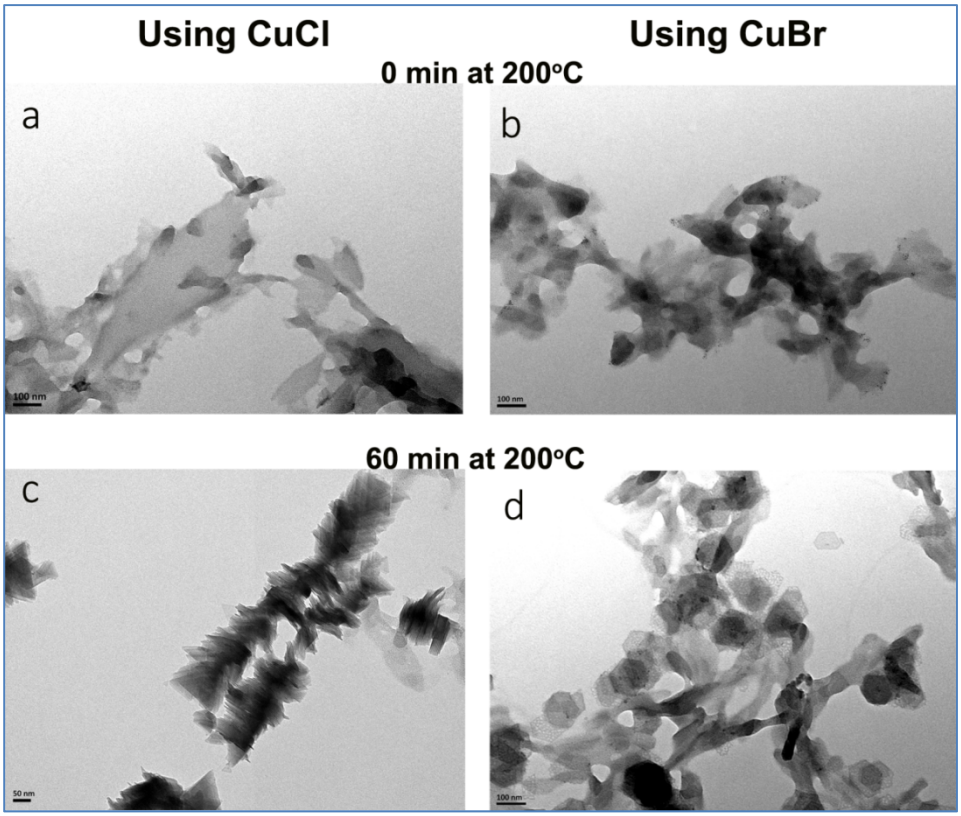

Figure 4.10 Comparing the rate of consumption of the preformed film while using (a,c) CuCl and (b,d) CuBr as the Cu precursor respectively. When the reaction temperature reached 200 ℃, both aliquots showed a similar looking preformed film structure, however after growth at (c) 200 ℃ for 60 min, the preformed films are almost fully consumed, leaving a large number of Cu_2S nanosheets; on the other hand, the consumption of the preformed film in case of CuBr case is very slow, where it is seen in (d) that a significant fraction of the preformed film remains even after 60 min of growth. Nevertheless, it is seen that hexagonal-shaped Cu_2S nanosheets were produced.

A histogram analysis of the sizes of the different structures synthesized (**Figures 4.9(d)-(f)**) showed that as the Cl^- concentration increased, the thickness of the resulting particles decreased, along with an increase in their lateral dimensions. Overall, the volume of the resulting nanostructures on a per particle basis was found to increase dramatically as well. These observations collectively support the hypothesis that the addition of Cl^- stabilizes the preformed film by binding to the copper centre as well, thereby

limiting and slowing down the nucleation process of Cu_2S which yielded larger nanostructures, as was in the case of Ni_9S_8. The effect of different halides on the synthesis of Cu_2S nanostructures was also explored. By using CuBr and CuI as precursors, it was found that nanosheets were also obtained, albeit at a higher reaction temperature than when Cl^- was introduced (see **Figure 4.10**). As with the growth of Ni_9S_8 nanosheets, the presence of Br or I groups inhibits the formation of Cu(I) thiolate and modifies the growth kinetics of Cu_2S such that a sheet-like morphology is produced. While the arrangement into stacked plates is rationalized by the assembly of the Cu(I) thiolate complex into a columnar mesophase, it is evident from our observations on the various morphologies obtained using different Cu(I) to halide ratios that modification of growth kinetics by the introduction of halides can play a dramatic role in obtaining 2D growth.

4.4 Conclusions

In summary, we have shown in this work that halide ions can play a decisive role in determining the morphology of nickel sulfide nanostructures, and the use of sufficiently large molar equivalents of halides results in nanoplate growth. This was attributed to Ni(II)-halide bonds which inhibited the formation of Ni(II) thiolates, resulting in suppressed nucleation and modified growth kinetics. This led to the formation of Ni_9S_8 nanoplates that possessed an unusual cross-like structure filled with step-like edges. Their unique stoichiometry, large surface-to-volume ratios and numerous exposed edge facets potentially make Ni_9S_8 nanoplates potent TMS-based electrocatalysts for dye-sensitized solar cells[17] or hydrogen evolution from

water.[34, 35] The use of halides in promoting sheet-like growth was successfully extended to Cu_2S, where ultrathin triangular nanoplates were produced via a similar synthetic protocol. Additionally, it was shown that monodisperse spheres, disks and plates of Cu_2S could be obtained by simply increasing the amount of Cl^- present in the reaction. It is remarkable that the ability to induce 2D growth in Cu_2S via the use of halides is analogous to our strategy employed in the case of Ni_9S_8 despite their different growth mechanisms. The findings in this work afford deeper insight into the formation of 2D semiconductor nanostructures and offer a highly facile route to the colloidal synthesis of such materials.

4.5 References

1. Hu, S.; Wang, X. *Chem. Soc. Rev.* **2013,** 42, 5577.

2. Chhowalla, M.; Shin, H. S.; Eda, G.; Li, L. J.; Loh, K. P.; Zhang, H. *Nat. Chem.* **2013,** 5, 263.

3. Ithurria, S.; Tessier, M. D.; Mahler, B.; Lobo, R.; Dubertret, B.; Efros, A. *Nat. Mater.* **2011,** 10, 936.

4. a. Schliehe, C.; Juarez, B. H.; Pelletier, M.; Jander, S.; Greshnykh, D.; Nagel, M.; Meyer, A.; Foerster, S.; Kornowski, A.; Klinke, C.; Weller, H. *Science* **2010,** 329, 550; b. Dogan, S.; Bielewicz, T.; Cai, Y. X.; Klinke, C. *Appl. Phys. Lett.* **2012,** 101, 073102 (1-4).

5. Bouet, C.; Tessier, M. D.; Ithurria, S.; Mahler, B.; Nadal, B.; Dubertret, B. *Chem. Mat.* **2013,** 25, 1262.

6. Ithurria, S.; Dubertret, B. *J. Am. Chem. Soc.* **2008,** 130, 16504.

7. Vaughn, D. D.; In, S. I.; Schaak, R. *ACS Nano* **2011,** 5, 8852.

8. Kirkeminde, A.; Ruzicka, B. A.; Wang, R.; Puna, S.; Zhao, H.; Ren, S. Q. *ACS Appl. Mater. Interfaces* **2012,** 4, 1174.

9. Li, Z.; Peng, X. G. *J. Am. Chem. Soc.* **2011,** 133, 6578.

10. Liu, Y. H.; Wang, F. D.; Wang, Y. Y.; Gibbons, P. C.; Buhro, W. E. *J. Am. Chem. Soc.* **2011,** 133, 17005.

11. Son, J. S.; Wen, X. D.; Joo, J.; Chae, J.; Baek, S. I.; Park, K.; Kim, J. H.; An, K.; Yu, J. H.; Kwon, S. G.; Choi, S. H.; Wang, Z. W.; Kim, Y. W.; Kuk, Y.; Hoffmann, R.; Hyeon, T. *Angew. Chem. Int. Edit.* **2009,** 48, 6861.

12. Huo, Z. Y.; Tsung, C. K.; Huang, W. Y.; Fardy, M.; Yan, R. X.; Zhang, X. F.; Li, Y. D.; Yang, P. D. *Nano Lett.* **2009,** 9, 1260.

13. Zhang, Y. J.; Lu, J.; Shen, S. L.; Xu, H. R.; Wang, Q. B. *Chem. Commun.* **2011,** 47, 5226.

14. Yan, Y.; Xia, B. Y.; Ge, X. M.; Liu, Z. L.; Wang, J. Y.; Wang, X. *ACS Appl. Mater. Interfaces* **2013,** 5, 12794.

15. Acharya, S.; Dutta, M.; Sarkar, S.; Basak, D.; Chakraborty, S.; Pradhan, N. *Chem. Mat.* **2012,** 24, 1779.

16. Li, L.; Chen, Z.; Hu, Y.; Wang, X. W.; Zhang, T.; Chen, W.; Wang, Q. B. *J. Am. Chem. Soc.* **2013,** 135, 1213.

17. Li, Y.; Wang, H.; Zhang, H.; Liu, P.; Wang, Y.; Fang, W.; Yang, H.; Li, Y.; Zhao, H. *Chem. Commun.* **2014,** 50, 5569.

18. Chi, W. S.; Han, J. W.; Yang, S.; Roh, D. K.; Lee, H.; Kim, J. H. *Chem. Commun.* **2012,** 48, 9501.

19. Mahmood, N.; Zhang, C. Z.; Hou, Y. L. *Small* **2013,** 9, 1321.

20. Calderon, M. F.; Zelaya, E.; Benitez, G. A.; Schilardi, P. L.; Creus, A. H.; Orive, A. G.; Salvarezza, R. C.; Ibanez, F. J. *Langmuir* **2013,** 29, 4670.

21. Hacohen, Y. R.; Grunbaum, E.; Tenne, R.; Sloan, J.; Hutchison, J. L. *Nature* **1998,** 395, 336.

22. Love, J. C.; Estroff, L. A.; Kriebel, J. K.; Nuzzo, R. G.; Whitesides, G. M. *Chem. Rev.* **2005,** 105, 1103.

23. Kerr, J. A., *CRC Handbook of Chemistry and Physics 1999-2000 : A Ready-Reference Book of Chemical and Physical Data (CRC Handbook of Chemistry and Physics)*. 81st ed.; CRC Press: Florida, USA, **2000**.

24. Macomber, R. S., *Organic Chemistry*. University Science Books: Sausalito, CA, USA, **1996**; Vol. 2.

25. Wu, Y.; Wadia, C.; Ma, W. L.; Sadtler, B.; Alivisatos, A. P. *Nano Lett.* **2008,** 8, 2551.

26. Chen, L.; Xia, Y. D.; Liang, X. F.; Yin, K. B.; Yin, J.; Liu, Z. G.; Chen, Y. *Appl. Phys. Lett.* **2007,** 91, 073511.

27. Espinet, P.; Lequerica, M. C.; Martin-Alvarez, J. M. *Chem.-Eur. J.* **1999,** 5, 1982.

28. Sandhyarani, N.; Pradeep, T. *J. Mater. Chem.* **2001,** 11, 1294.

29. Wang, Y.; Hu, Y. X.; Zhang, Q.; Ge, J. P.; Lu, Z. D.; Hou, Y. B.; Yin, Y. D. *Inorg. Chem.* **2010,** 49, 6601.

30. Bryks, W.; Wette, M.; Velez, N.; Hsu, S. W.; Tao, A. R. *J. Am. Chem. Soc.* **2014,** 136, 6175.

31. Li, X. M.; Shen, H. B.; Niu, J. Z.; Zhang, Y. G.; Wang, H. Z.; Li, L. S. *J. Am. Chem. Soc.* **2010,** 132, (37), 12778.

32. Clugston, M.; Flemming, R., *Advanced Chemistry*. Oxford University Press: Oxford, UK, **2000**; Vol. 18.

33. Macomber, R. S. *Organic Chemistry*. University Science Books: Sausalito, CA, USA, **1996**; Vol. 1.

34. Zhang, W.; Wang, Y. B.; Wang, Z.; Zhong, Z. Y.; Xu, R. *Chem. Commun.* **2010,** 46, 7631.

35. Hong, J. D.; Wang, Y. S.; Wang, Y. B.; Zhang, W.; Xu, R. *ChemSusChem* **2013,** 6, 2263.

CHAPTER 5

Unique N-type PbS Nanosheets via Cation Exchange from Cu_2S Nanosheets

5.1 Introduction

Colloidal quantum dots based photovoltaic devices have been extensively studied due to their benefits such as low cost, solution-processable and band gap tuning ability.[1] Among the existing quantum dot materials, lead chalcogenides (PbS/Se), especially PbS, have received extensive attention lately due to its large exciton Bohr radius and enhanced absorption cross section that allows maximum solar energy harvesting across the whole visible range, all the way to near infrared (IR).[2-5] The great potential for using PbS as the photovoltaic material has been strongly demonstrated after Sargent's group published PbS quantum dots based solar cell efficiency up to 7% in 2012.[6] Recently, Bawendi et. al. reported the highest power conversion efficiency of 8.55% achieved by using PbS spheres as the active layer which introduced a promising approach of achieving PbS based high performance and air-stable photovoltaic devices.[7]

However, PbS nanocrystals based photovoltaic devices are still unstable due to surface oxidation in air. Also, the information on these nanocrystals' surface is vastly lacking. For instance surface geometry, exposed specific facets and ligand passivation, where the development on understanding these surface behaviors is essential. Thus, it would be of high importance to improve material properties for extensive surface characterizations as well as device stability under ambient condition.

It has been reported that the as-synthesized PbS nanocrystals generally exhibit a Pb excess surface which makes them intrinsic n-type material.[8] It was reasoned that excess Pb-salt present in the synthesis process helped them to passivate well. Moreover, when exposed to ambient air, PbS could be

oxidized easily (or become oxygen-doped) and behaved as p-type material in most cases, rendering it more difficult to obtain air stable n-type PbS. A recent report pointed out that depending on atomic infusion of impurities into the thin film, PbSe or PbS could result in p- or n-type behavior in field effect transistor (FET) device.[9] This is very significant for development of QD based electronic devices, since one could utilize solution processable inorganic nanocrystals with strong quantum confinement for the fabrication of the whole p-/n- junction without introducing any other type of n-type materials. Moreover, surface impurities as well as surface passivation can lead to different types of properties.

Along with theoretical simulation of the PbS surface passivation,[10-12] many attempts have been put to achieve such air stable Pb-rich property. Earlier, Sargent's group reported a method to retain the inherent n-type characteristic of PbS spheres by halide ion (Cl^-, Br^-) protection, however this n-type PbS device will be transformed into p-type when exposed to O_2 flow for even less than 10 min.[13] Later, with iodide treatment, they managed to obtain air-stable n-type PbS solid and further achieved quantum junctions devices with process-compatible n- and p- type colloidal quantum dots solids. [3] In addition, post synthetic treatments have been adopted to transform the quantum dot insulating thin film firstly into p-type and then n-type by dipping it into the Na_2S followed by $PbCl_2$ solution.[14, 15] This dramatic switch from p- to n-type behavior is because the Pb-rich surface could recover the n-type nature of Pb chalcogenide, when Pb-salt was used to passivate the surface. Therefore, Pb-rich surface are crucial to preserve n-type nature. Jeong et al. achieved stable PbS by shrinking their size into ultrasmall spheres, where they

pointed out that n-type stability requires the majority termination facets to be Pb-rich ±{111} planes on the nanocrystal surface which could only be possible when the size is very small. The atomic orientation of such facets could strongly improve the ligand passivation on the outward of the nanocrystals which crucially determines the stability of these materials.[16] Thus, large dimensional Pb-rich ±{111} planes in PbS nanostructures would be highly desirable for future applications.

Most of the photovoltaic devices were made by spherical PbS dots as the solar energy absorbing layer and the optimal efficiency were not reflected on these devices as the problem of charge hopping and tunneling many times among the dots in the active layer occurs.[17] Two dimensional nanosheet morphology could potentially address this charge transportation issue by largely reducing the hopping and tunneling process owing to the comparatively large lateral dimension for each nanosheet.[18] Moreover, nanosheet could offer plenty of new physical properties due to their one dimensional confinement, for instance, CdSe nanoplatelets could give ultra-narrow emission FWHM, and the band gap of MoS_2 nanosheets could switch from indirect to direct while reducing the thickness from bulk to one or two monolayers.[19, 20] There are little reports on two dimensional PbS nanosheets. Weller's group reported their achievement of ultrathin solution processable colloidal PbS nanosheet with large lateral dimension of up to 500 nm, by injecting chlorine-containing solvents into the reaction pot filled with as-synthesized PbS spheres. They managed to trigger the oriented attachment of PbS spheres to further grow into nanosheets.[21] Other examples included PbS nanosheets achieved by compression of PbS nanowires while floating on the

air-water interface, followed by high temperature annealing,[22] and hydrothermal approach to fabricate micrometer-size PbS sheets. [23, 24]

Here in this work, we aim to achieve continuous PbS nanosheet (150~200nm) via novel cation exchange reaction where we use Cu_2S as starting materials. Our as synthesized Cu_2S nanosheets possesses ±{002} facets as basal plane which are similar to those ±{111} for PbS. Thus, we hypothesized to obtain large exposure of Pb-rich {111} facet after cation exchange reaction. These materials will be well passivated by $Pb(Oleate)_2$ on both top and bottom planes, which can potentially help to achieve a highly air-stable PbS nanosheets. The atomic layer of Pb atoms were half coordinated (with three neighboring S atoms) and one more electron of Pb should be binded with anionic oleate ligand for perfect passivation. This unique Pb-rich PbS nanosheet is a promising candidate for achieving n-type material that can stabilize itself under ambient air and possess excellent FET performance**.**

5.2 Experimental section

5.2.1 Chemicals and materials

Copper (I) chloride (CuCl, 99.99%), 1-octadecene (ODE, 90%), trioctylphosphine oxide (TOPO, 99%), 1-dodecanethiol (1-DDT, 97%), lead (II) acetate ($Pb(Ac)_2$, $3H_2O$), oleic acid (90%, technical grade), trioctylphosphine (TOP, 97%), 3-mercaptopropionic acid (MPA, 99%) were purchased from Sigma Aldrich. All the chemicals were used as received without further purification. Unless stated otherwise, all reactions were conducted in oven-dried glassware under nitrogen atmosphere using standard Schlenk techniques.

5.2.2 Synthetic details

Synthesis of Cu_2S nanosheets

Briefly, CuCl (0.4 mmol), TOPO (2.5 mmol), ODE (20 mL) were degassed under vacuum at 90 ℃ in a round bottom 3-neck flask for 1 hour. 1-DDT (4 mmol) was then swiftly injected into the three neck reaction flask at 160℃, upon which the mixture was continuously heated until the growth temperature of 210 ℃ and then kept at this temperature for 2~3 hours. This yielded Cu_2S sheets with thickness of 3~ nm and lateral dimension of about 150~200 nm. For further purification, the reaction mixture was cooled to room temperature, where 1 equivalent of toluene and 8 equivalents of ethanol were added to 1 equivalent of raw solution, followed by centrifugation at 3900 rpm for 5 min. The resulting precipitate was redispersed in toluene and reprecipitated by ethanol for another two rounds. The processed NCs were then dispersed in toluene and sonicated for 1 hour (or longer if necessary) for subsequent use.

Cation exchange of Cu_2S nanosheets to PbS nanosheets

This Pb(II) exchange process was also followed by the reported[1] procedure. Initially, lead oleate was prepared by dissolving $Pb(Ac)_2 \cdot 3H_2O$ (3.3 mmol), oleic acid (7.9 mmol) in ODE (6.1 mL) in a three-neck RBF flask. This mixture was degassed at 90°C for 30 min followed by heating at 250°C. In a typical reaction, $Pb(Ac)_2 \cdot 3H_2O$ (0.7 mmol), dissolved in 3 mL of methanol, was added rapidly to a stirring solution of Cu_2S nanosheets that were dispersed in toluene. Next, 3 mL of lead oleate was added to enhance the solubility to the

solution. We used huge excess of Pb(II) ion for this exchange method. Finally, 0.6 mL of TOP as added to remove the Cu^+ ion by favorable complex formation with TOP. A progressive color change to black was observed during the time span of the reaction. The solution was allowed to react for 6 to 7 days before being precipitated with methanol and then re-dispersed in chloroform.

5.2.3 Characterizations

Transmission Electron Microscopy (TEM)

A JEOL JEM 1220F (100 kV accelerating voltage) microscope was used to obtain bright field TEM images of the nanoparticles. For TEM sample preparation, a drop of the nanoparticle solution was placed onto a 300 mesh copper grid covered with a continuous carbon film. Excess solution was removed by an adsorbent paper and the sample was dried at room temperature. The High-Resolution TEM images and detailed elemental analysis were carried out on a FEI Titan 80-300 electron microscope (operated at 200 KV) which is equipped with an electron beam monochromator, an energy dispersive X-ray spectroscopy (EDX) and a Gatan electron energy loss spectrometer. The probing electron beam size for point EDX measurements was around 0.3 nm. The dwell time for each EDX spectrum was about 10 s.

X-Ray Diffraction (XRD)

XRD data was obtained with a diffractometer (Bruker AXS, GADDS) using Cu-Kα radiation (λ=1.540598Å) in the range of 20˚ to 80˚. Thin film samples were prepared on a clean silicon wafer by placing several drops of concentrated nanoparticle samples in hexane on the silicon surface and dried at 60˚C in the oven. This was repeated several times until a thin layer of solid

was formed on the silicon substrate. The powder form of XRD samples were prepared by several times of purification followed by drying under N_2.

Atomic Force Microscope (AFM)

We recorded the AFM data via a Bruker Dimension FastScan AFM operating in tapping mode (FASTSCAN-A). We used the software named "Nanoscope Analysis" to determine the height profile of the sheet-like structures which were deposited onto the silicon substrates.

5.2.4 Optical characterization

Solution sample and thin film sample:

Absorption spectra were obtained with an Agilent 8453 UV-Visible spectrophotometer using a quartz cuvette with a path length of 1 cm.

5.2.5 Device Fabrication

Top-contact, bottom-gate FET device with lead sulfide sheets as the active component was fabricated on a SiO_2/Si wafer in inert atmosphere.

The wafer was cleaned by sonication in acetone and then IPA for 15 minutes each. The cleaned wafer was then dried with nitrogen gun. The PbS sheets were then coated on the wafer via layer-by-layer sequential spin coating technique. Ligand exchange process was performed with MPA for each layer. Then, a chloroform solution of PbS nanosheets was spin coated on the wafer with a speed of 4000 rpm for 10 seconds. Subsequently few drops of MPA solution in methanol was added to the film on the wafer and wait for 20 seconds then spun with same speed and time. Finally, the film was washed by methanol and chloroform. The process was repeated for 10 layers.

Subsequently, pairs of gold electrode of 50nm thickness as source and drain were deposited by thermal evaporation through a shadow mask to complete the FET device with a configuration of channel length of 80 μm and channel width of 6 mm. Silicon oxide at the backside of the silicon wafer of the FET device was removed with sandpaper to provide a conductive gate contact. Characterization of FET behavior of the device was then carried out with a Keithley SCS-4200 probe station inside glove box.

5.3 Results and discussions

The idea of obtaining Pb-rich PbS nanocrystal behaving as air-stable n-type material opens a novel path to the solution processable p-/n- junction. Noticeable efforts have been made for achieving Pb-rich stoichiometry i.e., exposed {111} plane, and most of them required post synthetic treatments.[3, 13, 14] It has been reported that PbS nanocrystals could be Pb-rich and highly stable with an ultra-small size of 1 to 2 nm, because the exposed facets were dominated by {111} plane, which composed of pure Pb atomic layer. Due to the wet chemistry synthetic approach while using oleic acid as the major surfactant, the {111} planes were terminated by Pb atoms with strongly binded oleic acid surfactant absorbed on their surface. [10-12] Herein, we propose that with our PbS nanosheet possessing Pb-rich {111} plane as the top and bottom lateral surface, one can directly achieve a stable and n-type PbS material without any post synthetic treatment to the device. However, the surface energy of {111} plane is the highest among the common planes that exist in PbS nanocrystals. Comparatively lower energy facets are {110} and {100} planes, where both comprised of mixture of Pb and S atoms in each atomic layer. As a result, the existence of {111} plane is less

thermodynamically favourable in normal bottom-up wet chemistry synthesis for large nanocrystal sizes, where the initially formed {111} facets were gradually replaced by {100} facets instead. To this point, we decided to adopt the cation exchange reaction by starting with an existing nanosheet material which possess similar facet orientation with a lateral plane comprising of specific facet (in this case, from {002} to {111}) and also with pure metal or S atomic layer. Besides, there are two major advantages of cation exchange approach: (i) retain the nanostructure morphology while varying the components in semiconductor nanocrystals, (ii) due to the structurally similarity among the different semiconductors, it allows the formation of special crystal phases which is not easy to obtain via normal synthetic methods.

The solution processable Cu_2S nanosheets will have the potential to enable us to further vary the semiconductor components via cation exchange reaction where the Cu^+ could be eventually replaced by Pb^{2+} while retaining the sheet-like morphology after being fully exchanged. We have reported previously,[25] that the synthetic parameters of Cu_2S nanosheets, such as precursors, surfactants, growth time and temperature, could be tuned for achieving various thicknesses and sizes of monodisperse nanosheets. We chose Cu_2S nanosheets with thickness of around 3 to 4 nm for the Pb^{2+} exchange reaction because ultrathin Cu_2S sheets could easily become holly after Pb^{2+} exchange while their thicker counterparts were difficult to be fully exchanged even after being exposed in Pb^{2+} for long time (more than two weeks).

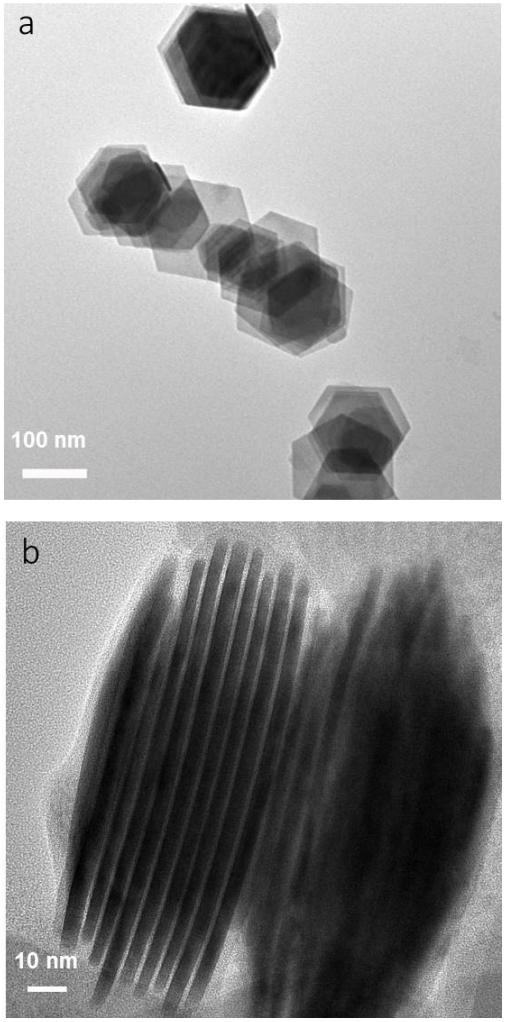

Figure 5.1 (a) A typical low resolution TEM image of Cu_2S nanosheets; (b) stacking Cu_2S nanosheets showing their thickness of around 3 to 4 nm.

Figure 5.1(a) shows the representative low resolution TEM image of as-synthesized Cu_2S nanosheets, purified and redispersed in toluene, and further dropcasted on carbon film coated 300 mesh copper grid. The shape of the nanosheets were presenting as hexagons, and the lateral dimension were around 150 nm to 200 nm. When projected from the side, where the Cu_2S nanosheets could stack together giving a side-view of the nanosheets in **Figure 5.1(b)**, we were able to measure the average thickness of nanosheets which was around 3 to 4 nm. Powder X-ray diffraction has been carried out and the results were displayed in **Chapter 4 Figure 4.7(b).** The experimental

XRD reflection matched well with the standard JCPDS-26-1116 data with a stoichiometry of Cu_2S, where the weak {002} peak implied the thin nature of the as-synthesized Cu_2S nanosheets and the sharp intense {110} signal could be possibly due to the large lateral dimension of the sheets. High resolution TEM of such Cu_2S nanosheets possessed good crystallinity, as seen in **Figure 5.2(a)**, revealed very clear lattice fringes of {110} planes from the top-down view and as well as {002} planes from the side view in **Figure 5.2(b)**.

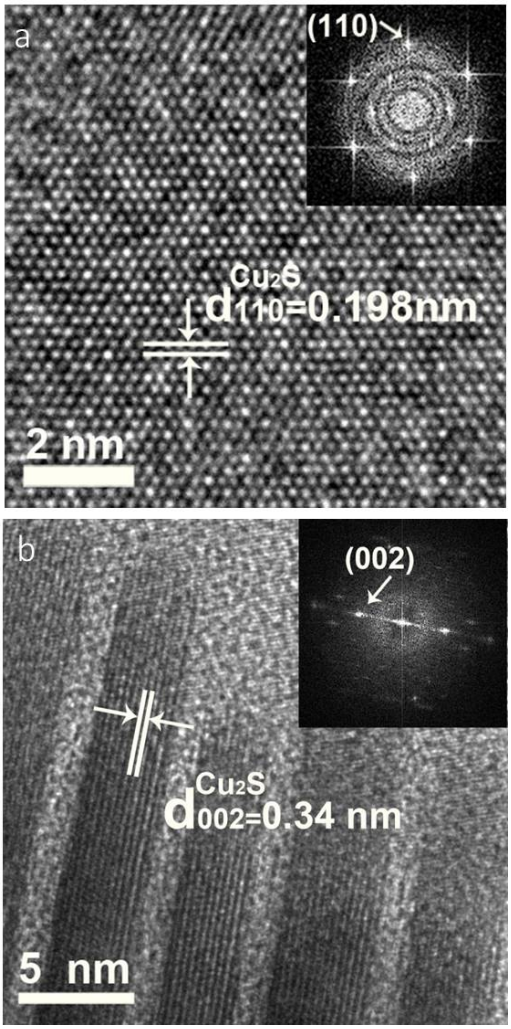

Figure 5.2 HRTEM of Cu_2S nanosheets from (a) top-down view, showing lattice d-spacing of {110} with the value of 0.198 nm, and (b) side-view of stacking nanosheets showing the lattice d-spacing of 0.34 nm representing {002} planes, as calculated from FFT pattern shown in the inset of (b).

Further investigation on the Cu_2S nanosheets structure and facet orientation via diffraction pattern and simulation on the reciprocal pattern were shown in **Figure 5.3**. The diffraction pattern revealed a larger prominent regular hexagonal pattern in the center with a smaller one inside, rotated at an angle of 30 degrees. These experimental results matched well with the simulated reciprocal pattern with the zone axis set as [0,0,1] in **Figure 5.3(b)**. The reflected spots in the larger hexagon implied that the six edges of the Cu_2S nanosheets were terminated by the fast growth {110} planes, while the spots in the smaller hexagon indicated the six edges of {100} planes as shown in the cartoon in **Figure 5.3(c)**. As the direction of projection was set to be [0,0,1] in the simulation, we were able to conclude the lateral plane of top and bottom should be the exposed {001} planes. With the use of the Crystallographic Data published in Solid State Ionics in 1981, [26] where the space group of $P6_3/mmc$, with unit cell lattice constants of a=0.3967 nm, b=0.3967 nm, c=0.6795 nm, α=90°, β=90°, γ=120°, we generated the expanded unit cell crystals as shown in **Figure 5.4(a)**. The nanosheet model possessed a large lateral plane of {002} on both top and bottom, which could be either terminated by Cu (orange atoms) or S (yellow atoms) atomic layers. Due to the similar alternating atomic layer of metal (Cu or Pb) and sulfur in Cu_2S and PbS lattices, the {002} facet could be a potential candidate when performing Pb^{2+} exchange reaction for achieving PbS nanosheets with Pb atom terminated lateral planes as presented in **Figure 5.4(b)**..

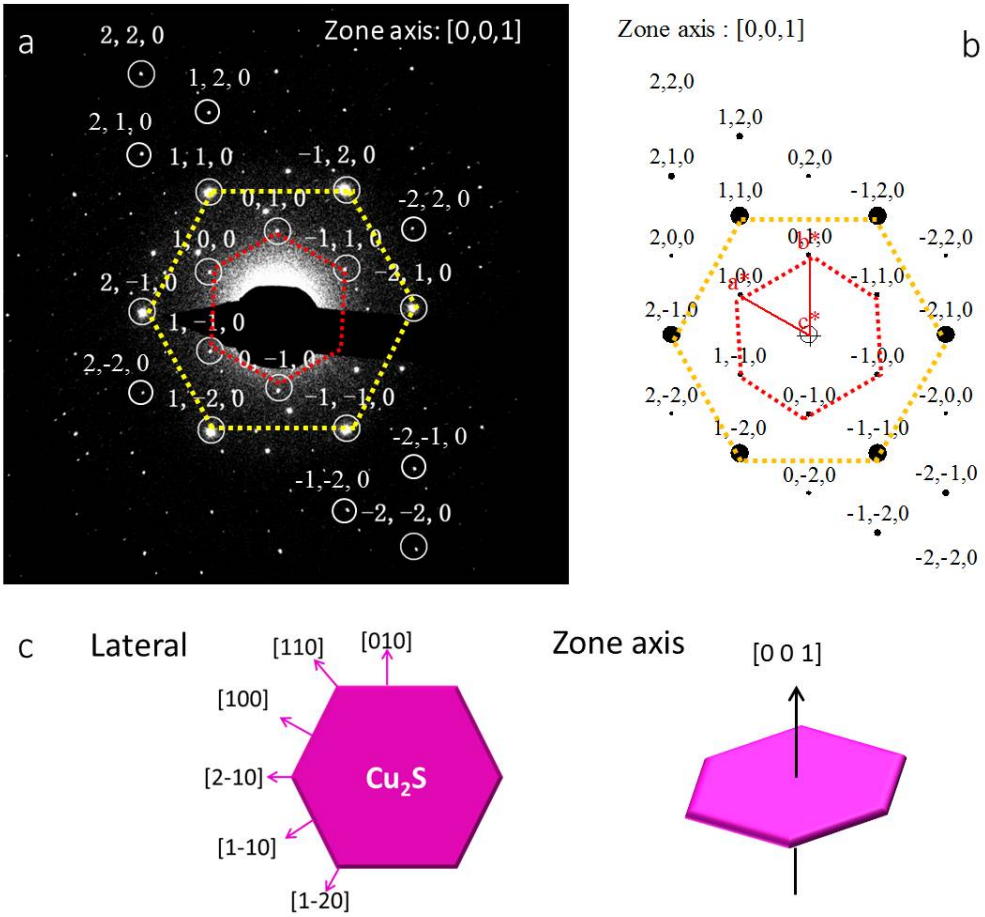

Figure 5.3 Facet orientation on Cu_2S nanosheets. (a) Diffraction pattern while projected on a single Cu_2S nanosheet lying flat on the copper grid, showing a prominent regular hexagonal pattern which matched well with (b) simulated reciprocal pattern while setting the zone axis as [0 0 1]; (c) cartoon indicated the facet orientation for the lateral and side planes, where the nanosheets corner were {110} and edges were {100}, the large lateral plane was {111}.

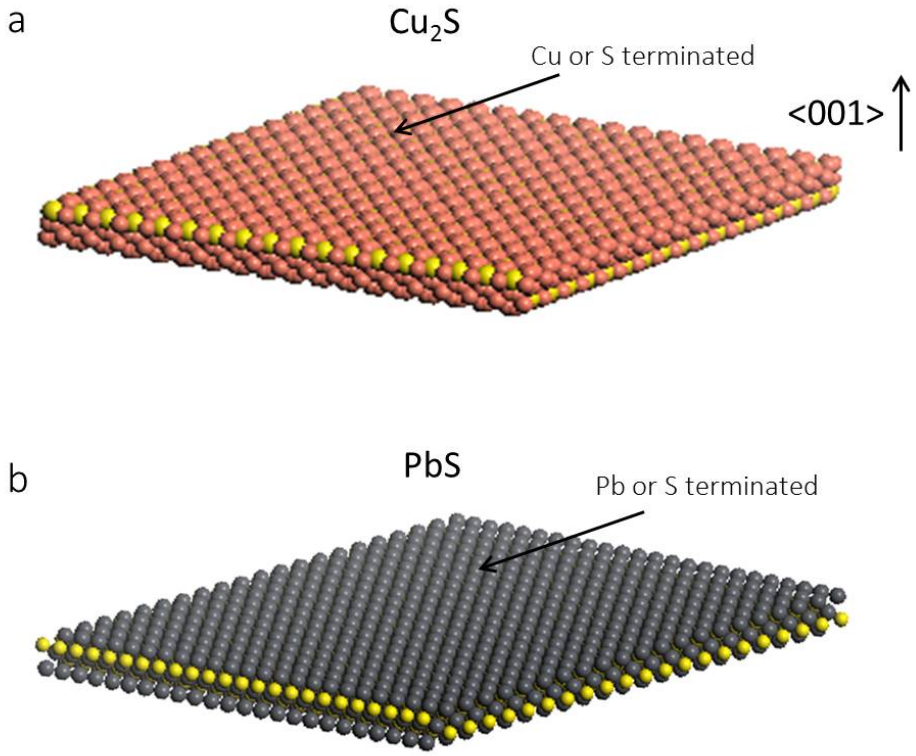

Figure 5.4 Possibility of achieving Pb-terminated PbS nanosheets via Pb^{2+} exchange on Cu_2S nanosheets. (a) model of Cu_2S nanosheets with lateral plane of {002}; (b) possible PbS nanosheet obtained from Cu_2S via cation exchange reaction with Pb-terminated lateral planes.

We carried out the Pb^{2+} exchange reaction by exposing Cu_2S nanosheets to excess amount of $Pb(Ac)_2$ and $Pb(Oleate)_2$ in the presence of TOP. The reaction was carried out under room temperature and lasted for several days for the exchange reaction to be completed. Aliquots were taken at suitable intervals during the exchange reaction, where a clear color change of the nanosheets suspension across the whole reaction time scale, from light brownish (on the left) to finally dark grey (on the right), was observed as shown in the digital photograph in **Figure 5.5(a)**. The color change also implied the components of nanosheets gradually being transformed from Cu_2S to intermediate Cu/PbS and then, to pure PbS. The vial on the right side is the final PbS nanosheets suspended in toluene, which is black in color. The optical

absorption spectrum of the PbS nanosheets dispersed in toluene was relatively featureless, with a broad absorbance profile that extended across the NIR spectral window (see **Figure 5.5(b)**). Previous efforts to exchange Pb-based

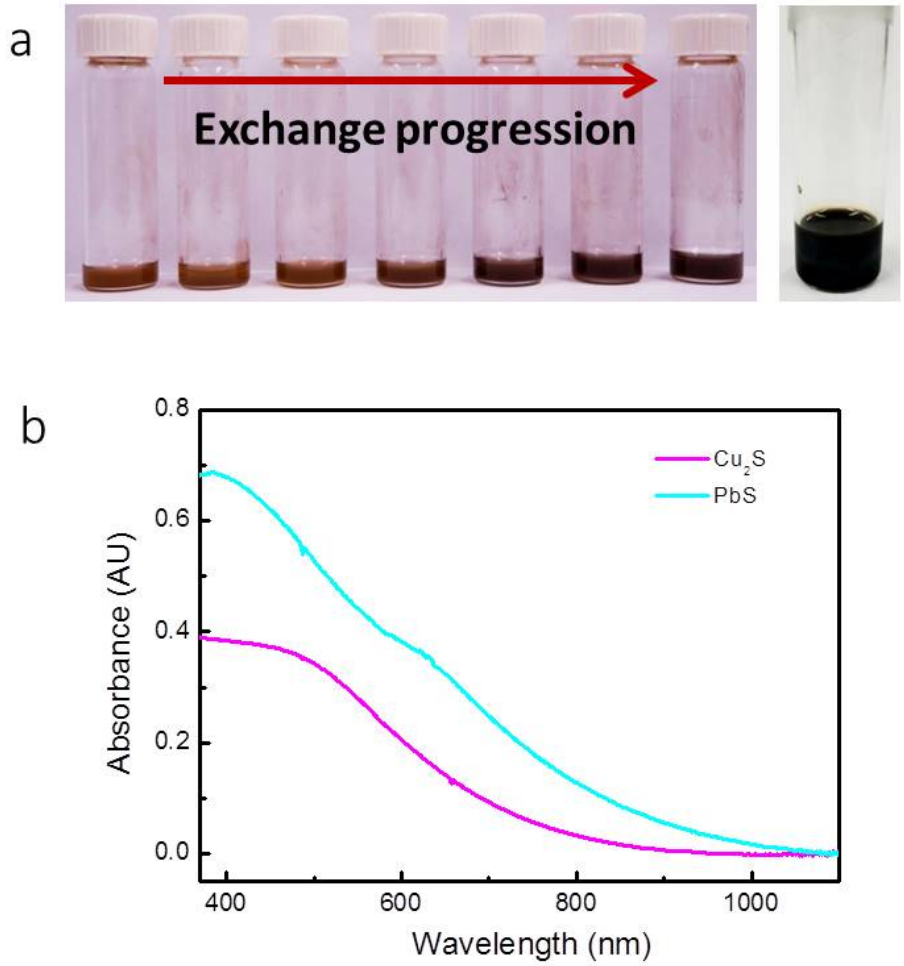

Figure 5.5 (a) Digital photograph of different time aliquots during the cation exchange reaction progression; (b) UV-vis absorption spectra of Cu_2S and PbS nanosheets suspended in toluene.

nanostructures are mainly confined in spheres and nanorod structures. [27] Due to the timescale of the exchange reaction of nanosheets, we reasoned that our choice of material can shed light on the progression of cation exchange process, which is difficult to obtain even in nanorod structures. Additionally, the long timescale of the reaction not only allowed us to study the intermediate stage obtained during the exchange reaction, but also to investigate their

mechanism in detail. Schematic representation about the progression of Pb-exchange process is illustrated in **Figure 5.6(a)**. We hypothesized that the exchange process will start at the edges of the nanosheets, which are most reactive,and then progress towards the center. This is clearly evident from the characteristic chemical mapping of the corresponding elements (Pb^{2+} (cyan),

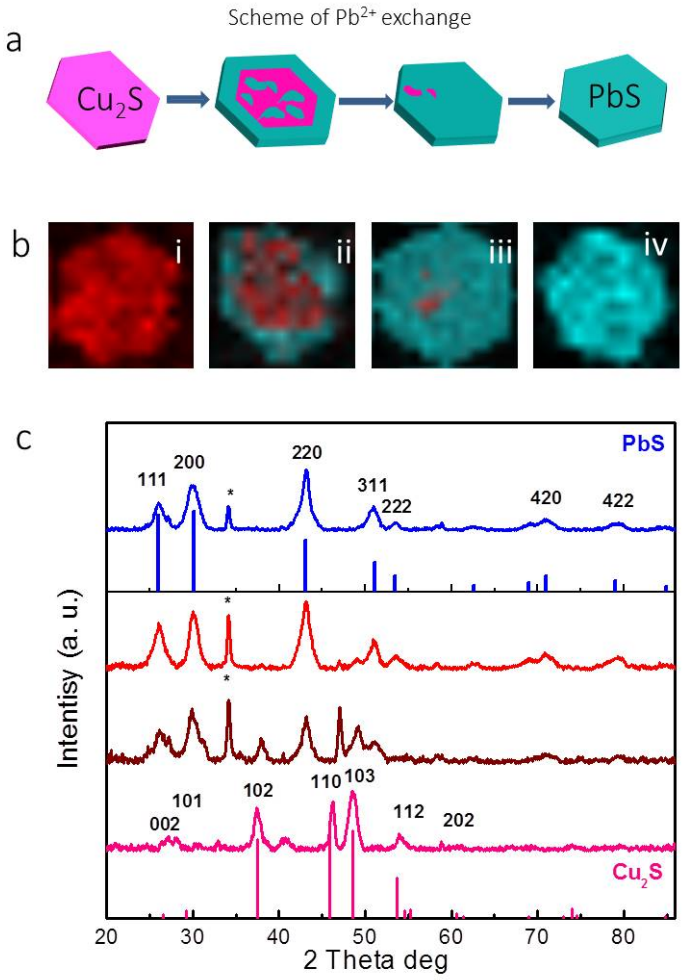

Figure 5.6 Monitoring the cation exchange by EDX mapping and XRD. (a) Schematic diagram of ultrathin PbS nanosheet formation by cation exchange process, where Pb^{2+} is introduced to pre-synthesized Cu_2S nanosheet. The exchange occurs from the edges towards the center, which is characterized in the chemical mapping of elements image in (b). It shows that Pb^{2+} (cyan) replaces Cu^{+} (red) at the edges first, and progressed towards the center region. (c) Systematic XRD study on nanosheets with different chemical compositions when the aliquots are taken at different time scale. From the XRD characteristic peaks, it is clearly evident that the initial Cu_2S peaks are slowly disappearing while PbS peaks appears as the exchange reaction progress.

Cu^+ (red)) in **Figure 5.6(b)**. At the beginning of the reaction, significant Pb signals were observed from the edges and the signals spreaded towards the center as the reaction proceeded. Structural characterization of the PbS nanosheets as well as their intermediate products were carried out via X-ray diffraction (XRD) measurements, as depicted in **Figure 5.6(c)**. During systematic XRD study, we observed different chemical compositions when the aliquots are taken at different time scale. The peaks obtained were referenced to starting material, i.e. hexagonal Cu_2S (JCPDS 26-1116) as well as final nanosheet structures, i.e. cubic PbS (JCPDS 78-1058). The close agreement with all of the reference index planes of Cu_2S and PbS suggests that they are highly crystalline in nature. Exquisite conservation of the anionic lattice of the original crystalline Cu_2S nanosheets is achieved in PbS nanosheets, despite undergoing long cationic-exchange reactions at room temperature. It is clearly evident that the initial Cu_2S peaks especially {102}, {110} and {103} are slowly disappearing while the PbS related peaks become more prominent during spontaneous exchange. Characteristic PbS peaks such as {111}, {200} and {220} clearly prove the existence of cubic face-centered PbS crystals.

Figure 5.7(a) is the reconstructed HRTEM image of the interface between hexagonal Cu_2S and rock salt PbS captured during cation exchange progression. Two different phases existed in the left and right part separated by a clear interface highlighted by yellow dash line in the image. The corresponding FFT of both parts were displayed in **Figure 5.7(b)** and **5.7(c)** respectively. A pair of reflection spots were labeled by the red arrow with a

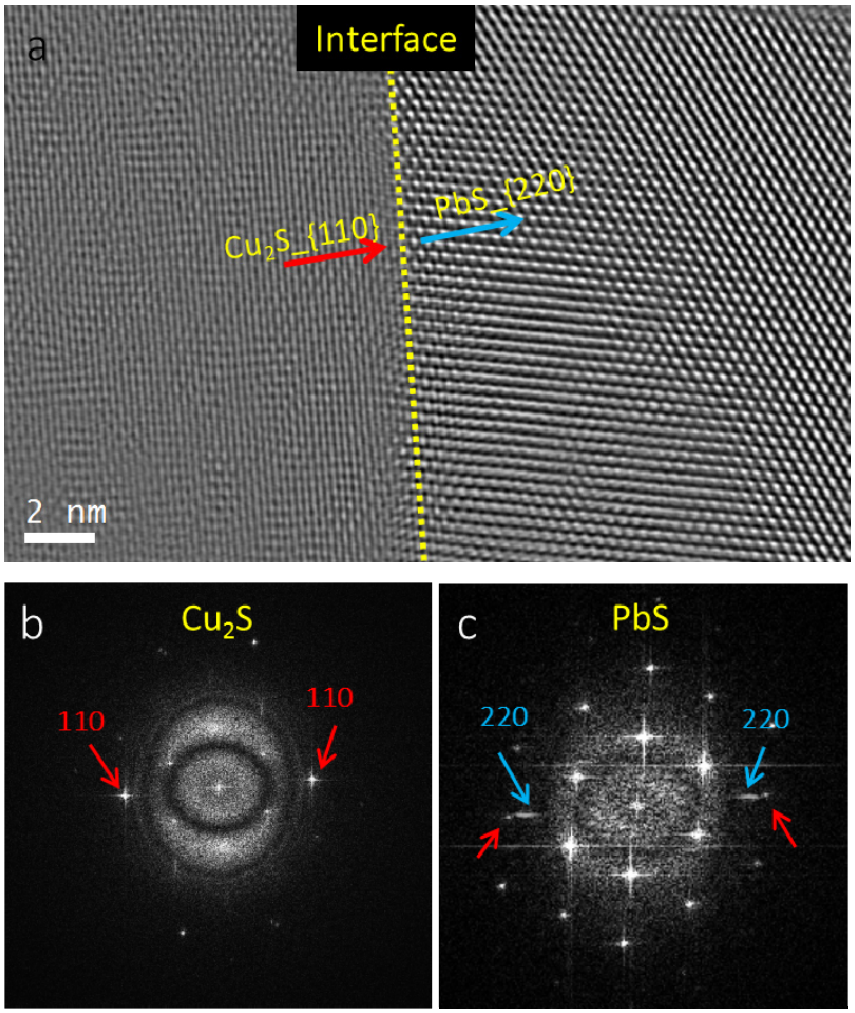

Figure 5.7. Interface between Cu_2S and PbS. (a) HRTEM imaging shows a representative interface transformed by inversed FFT; (b) FFT of the Cu_2S part (left part in (a)) revealed a pair of reflected spot of {110} plane; (c) the FFT on the PbS part (right part in (b)) showing a presented {220} reflected spot .

calculated d-spacing of 0.198 nm representing {110} planes belong to Cu_2S (as seen in **Figure 5.7(b)**). This pair of spots slightly shifted towards the center in FFT pattern, as seen in **Figure 5.7(c)**, obtained from the right part of the image where the blue arrows pointed out the new pair of spots corresponding to $\{220\}_{PbS}$, which were closer to the center but remaining the same direction as Cu_2S_{110}. As a result, the left side still remained with unexchanged Cu_2S and right part have already been transformed into PbS, showing an interface on the boarder between $\{110\}_{Cu_2S}$ and $\{220\}_{PbS}$.

Furthermore, the Pb^{2+} exchange reaction could possibly carried out along {110} plane of Cu_2S which have a comparatively higher surface energy over {100}, and finally arrived at atomically more similar {220} planes in PbS.

Detailed structural characterizations have been carried out, as shown in **Figure 5.8**. A representative low resolution TEM was taken after fully cation exchange from Cu_2S to PbS, as seen in **Figure 5.8(a)**, the sheet-like morphology were well preserved with lateral dimension of around 150~200 nm and average thickness of 3 to 4 nm. HRTEM image as well as inset FFT of the Pb-exchanged nanosheets are presented in **Figure 5.8(b) and 5.8(c)**. The observed d-spacing valued ~0.21 nm and ~0.34 nm corresponds to (220) and (111) plane of PbS material. Interestingly, these PbS nanosheets are stacked along <111> axis with largely exposed ±{111} planes in large lateral dimention where as previous report to obtain PbS nanosheets relys on oriented attachment processes where most reactive ±{110} facets are fused leaving other facets ±{100} exposed.[20] However, we observed a rare facet orientation in exchanged PbS nanosheet structures where most reactive ±{111} planes are mainly exposed from the top and bottom surfaces of the nanosheets. On the other hand, the diffraction pattern on single PbS nanosheet matched well with the simulated pattern obtained from CaRIne v3.1, with the zone axis set as<111>, as shown in **Figure 5.9(a)** and **5.9(b)**. According to the HRTEM, diffraction pattern as well as the shape of the PbS nanosheet, we suggested a possible facet orientation after cation exchange reaction, as depicted in **Figure 5.9(c)**. The six edges of the hexagon were possibly terminated by {200} plane, while {220} planes were exposed at the corners. With XPS characterization of

as-synthesized PbS nanosheet revealed the atomic ratio between Pb and S is 0.57 : 0.43 with a slightly higher Pb amount. Based on the above

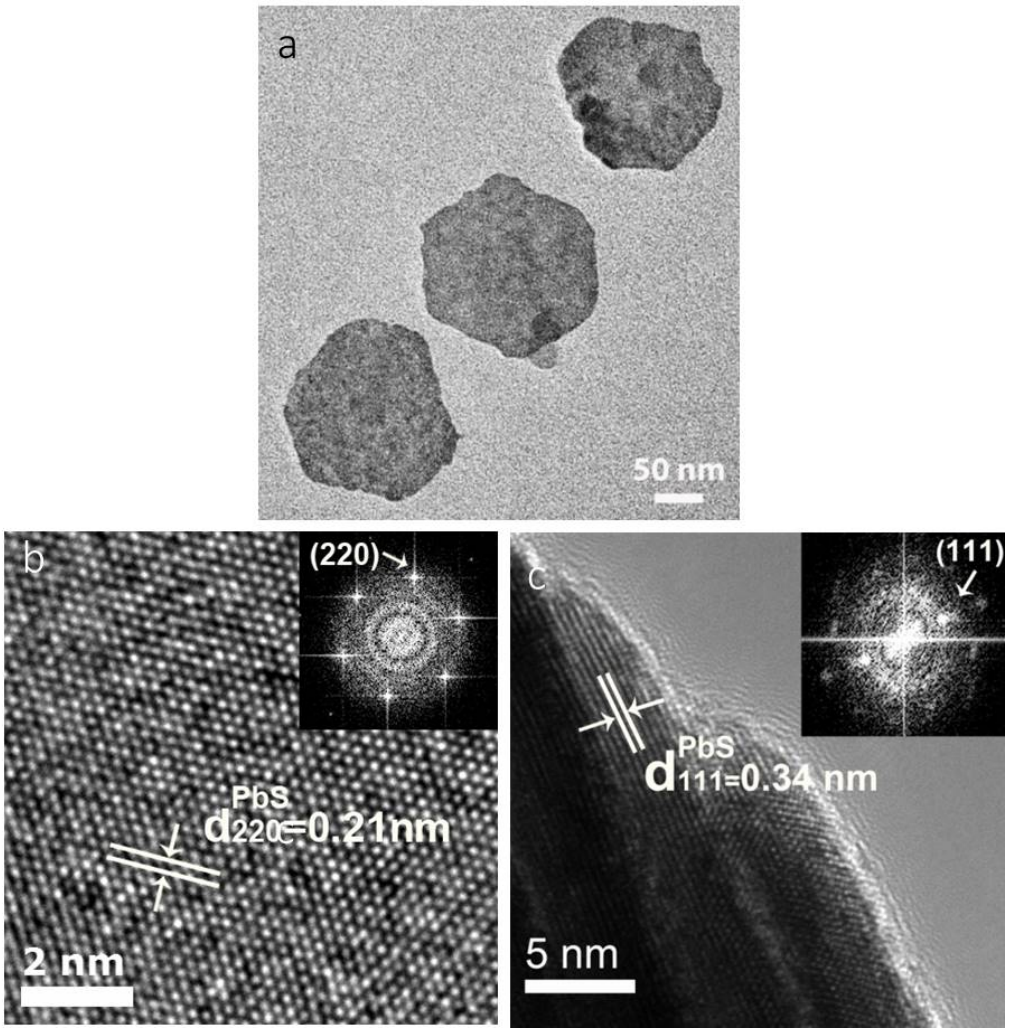

Figure 5.8 Representative top-view (a) low resolution TEM of PbS nanosheets; (b) the HRTEM images, the lattice spacing of 0.21 nm and inset FFT image clearly show the {2 2 0} plane in PbS structures. Side-view HRTEM images as well as inset FFT images confirm corresponding lattice spacing values of (c) PbS nanosheets equals to 0.34 nm matching with the standard lattice d-spacing of {111} planes.

characteriaztions, the PbS nanosheets presented two novel features: (i) both

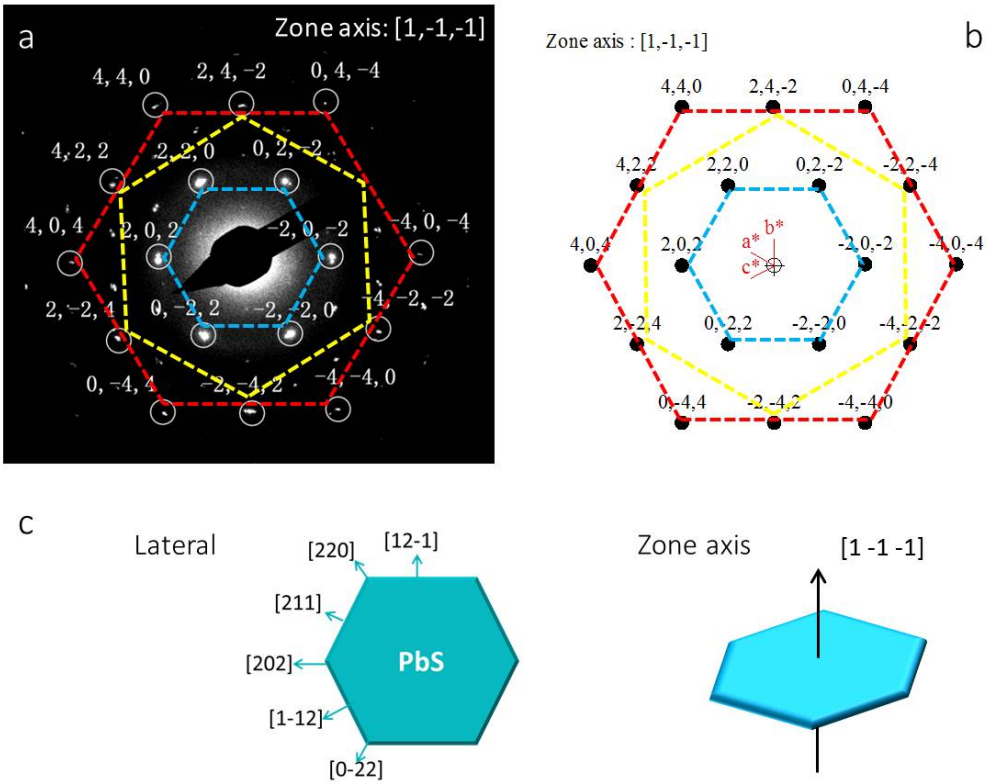

Figure 5.9 Diffraction pattern on single PbS nanosheet. (a) Experimental diffraction pattern on PbS nanosheet, revealing a most prominent hexagonal pattern in the center representing {220} plane (blue dash line), and two other larger hexagonal patterns (yellow and red dash lines); these reflected spots matched well with (b) simulated reciprocal pattern when set the zone axis as [1,-1,-1], indicated that the lateral plane of PbS nanosheets was indeed {111} facets; (c) cartoon for displaying the facets orientation on the lateral plane and side / corner planes.

top and bottom facets were {111} planes; (ii) these {111} planes could possibly be Pb-terminated facets with close-packed $Pb(Oleate)_2$ as surface passivation, that could lead to air-stable n-type conduction behavior.

So, the as synthesized PbS nanosheets were purified and redispersed in chloroform for fabrication of FET in order to support our hypothesis that PbS nanosheets would be n-type in carrier conduction. We fabricated bottom gate

top-contact FET configuration as shown in **Figure 5.10(a)**. The thin film of PbS nanosheets was prepared by layer-by-layer sequential spin-coating technique on SiO_2/Si wafer. Finally a pair of gold electrode was deposited which serve as source and drain of the FET device.

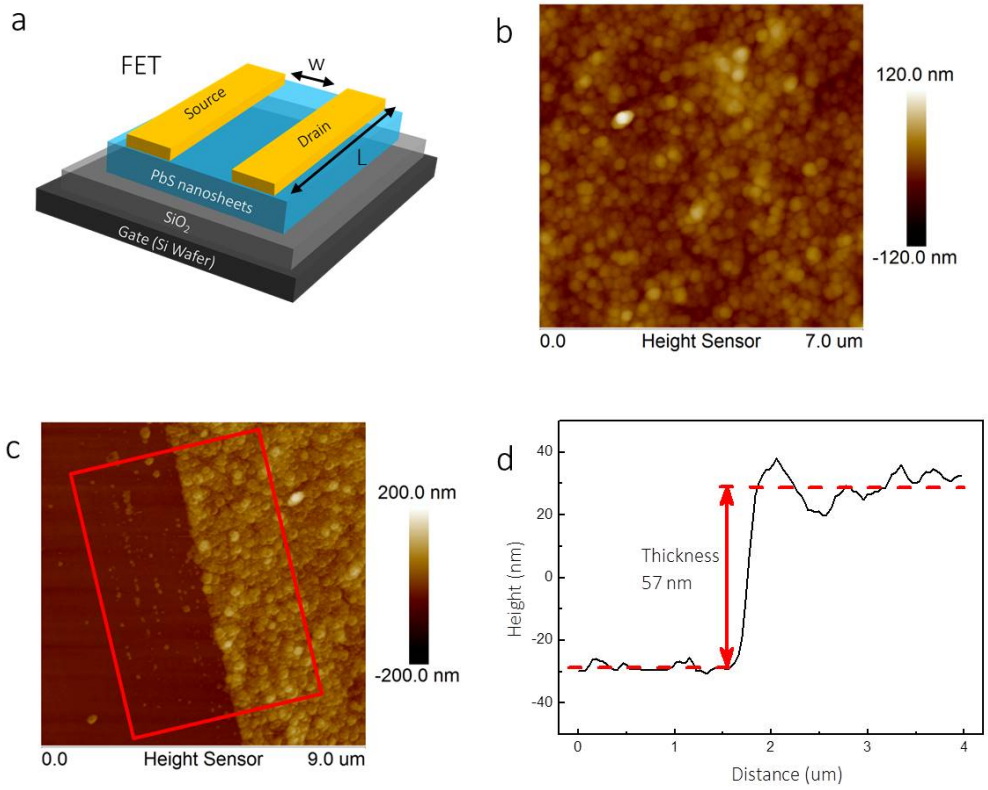

Figure 5.10 FET configuration and AFM characterization of the PbS film. (a) Schematic drawing of Field Effect Transistor with a Top-contact, bottom-gate configuration. Channel width (W) is 80 μ m and channel length (L) is 6 mm. (b) AFM characterization of the PbS thin film on the device, roughness is around 15 to 16 nm; (c) AFM image on the scratched thin film, the red color rectangular area was selected for measuring average film thickness; (d) the height profile of the film thickness is around 57 nm on average.

We studied the surface morphology of the thin film of PbS nanosheets via AFM as shown in **Figure 5.10(b-d)**. The thin film was prepared with same technique and condition as it was for FET device. From the roughness analysis, it shows a Root mean square (RMS) roughness around 15 nm. We usually

obtained a comparatively higher roughness value which might be due to the reason that the nanosheets were more difficult to be made into a close packed film because of their anisotropic shape with large aspect ratio as compared to their spheres counterparts. They might easily tilt or stack irregularly rather than lie down flat and perfectly in the thin solid film. The roughness have been further improved by using combination of solvents to disperse nanosheets during the spincasting process, and surface treatment during the film fabrication. We introduced MPA to treat the film after each spin-coated layer, which eventrally reduced the roughness of the final film. To improve the stability of the FET device, the as prepared device was kept under inert atmosphere prior to any measurement of the device.

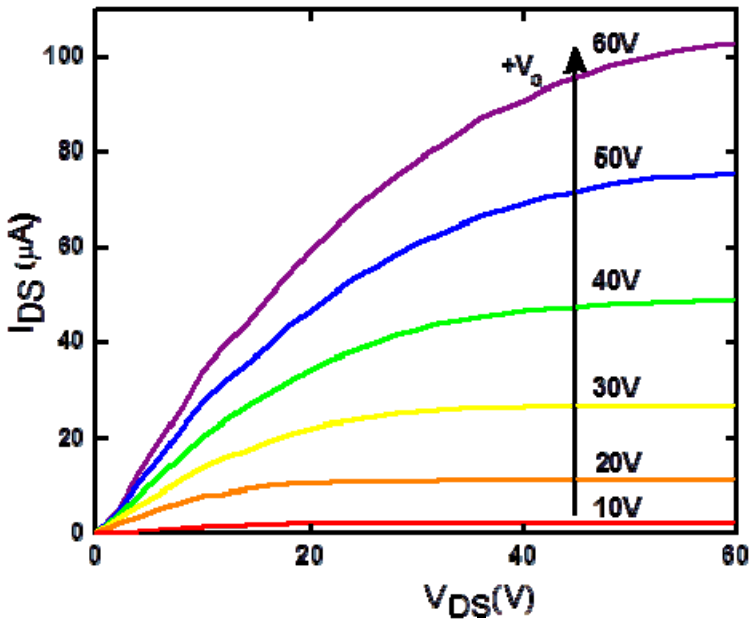

Figure 5.11. PbS based FET shows obvious n-type conduction as a function of applied gate voltage.

Figure 5.11 shows the I_D-V_D output characteristics of the FET device at different applied gate voltage. Characteristics that support the n-channel

operation of the FET device included the increase in drain current with more positive gate voltage and also a clear linear and saturation region. We extracted the electron mobility data from the saturation regime using the equation below:

$$\mu_{sat} = \frac{2L(\frac{\partial I_D^{1/2}}{\partial V_G})^2}{WC_i}$$

where I_D is the drain current, μ is the field-effect mobility, C_i is the capacitance per unit area of the gate dielectric layer, V_G is gate voltage, W is channel width of 6 mm and L is channel length of 80 μ m.

The electron mobility was calculated from the output characteristics and was calculated to be 8.7 x 10^{-3} cm^2/Vs. As we hypothesized that large exposed Pb-rich facet of the PbS nanosheets could be responsible for n-type carrier conduction, FET characteristics supported the same.

5.4 Conclusions

We have successfully achieved the Pb-rich PbS nanosheets by cation exchange reaction while adopting Cu_2S as our starting material. The unique facet orientation of as-synthesized PbS possessed a special Pb-terminated {111} plane on both top and bottom of the nanosheets in a large lateral dimension, which is very difficult to achieve in normal wet chemistry synthetic approach due to the highest surface energy of {111} planes. Furthermore, the Pb-rich nature gave us a great opportunity to retain the n-type behaviour of PbS semiconductors and help to resist surface oxidation. Our discovery of n-type PbS nanosheets with novel facet orientation opens up

a path for fabrication of high performance quantum junctions with high stability under operation in ambient air.

5.5 References

1. Kramer, I. J.; Sargent, E. H., *Chem. Rev.* **2014,** 114, 863.

2. Pattantyus-Abraham, A. G.; Kramer, I. J.; Barkhouse, A. R.; Wang, X. H.; Konstantatos, G.; Debnath, R.; Levina, L.; Raabe, I.; Nazeeruddin, M. K.; Gratzel, M.; Sargent, E. H., *ACS Nano* **2010,** 4, 3374.

3. Ning, Z. J.; Voznyy, O.; Pan, J.; Hoogland, S.; Adinolfi, V.; Xu, J.; Li, M.; Kirmani, A. R.; Sun, J.-P.; Minor, J.; Kemp, K. W.; Dong, H.; Rollny, L.; labelle, A.; Carey, G.; Sutherland, B.; Hill, L.; Amassian, A.; Liu, H.; Tang, J.; Bakr, O. M.; Sargent, E. H., *Nat. Mater.* **2014**, DOI: 10.1038/NMAT4007.

4. Johnston, K. W.; Pattantyus-Abraham, A. G.; Clifford, J. P.; Myrskog, S. H.; MacNeil, D. D.; Levina, L.; Sargent, E. H., *Appl. Phys. Lett.* **2008,** 92, 3.

5. Koh, W. K.; Koposov, A. Y.; Stewart, J. T.; Pal, B. N.; Robel, I.; Pietryga, J. M.; Klimov, V. I., *Sci Rep* **2013,** 3, 8.

6. Ip, A. H.; Thon, S. M.; Hoogland, S.; Voznyy, O.; Zhitomirsky, D.; Debnath, R.; Levina, L.; Rollny, L. R.; Carey, G. H.; Fischer, A.; Kemp, K. W.; Kramer, I. J.; Ning, Z. J.; Labelle, A. J.; Chou, K. W.; Amassian, A.; Sargent, E. H., *Nat. Nanotechnol.* **2012,** 7, 577.

7. Chuang, C.-H. M.; Brown, P. R.; Bulovic, V.; Bawendi, M. G., *Nat. Mater.* **2014**, DOI: 10.1038/NMAT3984.

8. Allgaier, R. S.; Scanlon, W. W., *Phys. Rev.* **1958,** 111, 1029.

9. Luther, J. M.; Pietryga, J. M., *ACS Nano* **2013,** 7, 1845.

10. Bealing, C. R.; Baumgardner, W. J.; Choi, J. J.; Hanrath, T.; Hennig, R. G., *ACS Nano* **2012,** 6, 2118.

11. Argeri, M.; Fraccarollo, A.; Grassi, F.; Marchese, L.; Cossi, M., *J. Phys. Chem. C* **2011,** 115, 11382.

12. Zherebetskyy, D.; Shcheele, M.; Zhang, Y.; Bronstein, N.; Thompson, C.; Britt, D.; Salmeron, M.; Alivisatos, P.; Wang, W.-L., *Science* **2014,** 344, 1380.

13. Zhitomirsky, D.; Furukawa, M.; Tang, J.; Stadler, P.; Hoogland, S.; Voznyy, O.; Liu, H.; Sargent, E. H., *Adv. Mater.* **2012,** 24, 6181.

14. Oh, S. J.; Berry, N. E.; Choi, J. H.; Gaulding, E. A.; Lin, H. F.; Paik, T.; Diroll, B. T.; Muramoto, S.; Murray, C. B.; Kagan, C. R., *Nano Lett.* **2014,** 14, 1559.

15. Oh, S. J.; Berry, N. E.; Choi, J. H.; Gaulding, E. A.; Paik, T.; Hong, S. H.; Murray, C. B.; Kagan, C. R., *ACS Nano* **2013,** 7, 2413.

16. Choi, H.; Ko, J. H.; Kim, Y. H.; Jeong, S., *J. Am. Chem. Soc.* **2013,** 135, 5278.

17. Konstantatos, G.; Sargent, E. H., *Proc. IEEE* **2009,** 97, 1666.

18. Acharya, S.; Sarma, D. D.; Golan, Y.; Sengupta, S.; Ariga, K., *J. Am. Chem. Soc.* **2009,** 131, 11282.

19. Bouet, C.; Tessier, M. D.; Ithurria, S.; Mahler, B.; Nadal, B.; Dubertret, B., *Chem. Mat.* **2013,** 25, 1262.

20. Chhowalla, M.; Shin, H. S.; Eda, G.; Li, L. J.; Loh, K. P.; Zhang, H., *Nat. Chem.* **2013,** 5, 263.

21. Schliehe, C.; Juarez, B. H.; Pelletier, M.; Jander, S.; Greshnykh, D.; Nagel, M.; Meyer, A.; Foerster, S.; Kornowski, A.; Klinke, C.; Weller, H., *Science* **2010,** 329, 550.

22. Acharya, S.; Das, B.; Thupakula, U.; Ariga, K.; Sarma, D. D.; Israelachvili, J.; Golan, Y., *Nano Lett.* **2013,** 13, 409.

23. Fang, Z.; Wang, Q.; Wang, X. Q.; Zhu, B. C.; Fan, F.; Wang, C. Y.; Liu, X. W., *Cryst. Res. Technol.* **2012,** 47, 635.

24. Dong, L. H.; Tang, S. S.; Xia, G. Q., *Micro Nano Lett.* **2013,** 8, 696.

25. Chapter 4: Promoting 2D Growth in Transition Metal Sulfide Semiconductor Nanostructures via Halide Ions .

26. Cava, R. J.; Reidinger, F.; Wuensch, B. J., *Solid State Ion.* **1981,** 5, 501.

27. Luther, J. M.; Zheng, H. M.; Sadtler, B.; Alivisatos, A. P., *J. Am. Chem. Soc.* **2009,** 131, 16851.

CHAPTER 6

Conclusions and Outlook

6.1 Conclusions of the thesis

This thesis has introduced novel wet chemically synthetic approach of colloidal semiconductor nanocrystals with mixed dimensionalities, and emphasized on their unique dimension-related physicochemical properties. Thorough structural characterizations were carried out to extensively explore these nanocrystals' growth mechanisms, while their promising optical and electronic properties have been demonstrated for potential optoelectronic applications.

In **Chapter 2**, we have successfully achieved MME from Type II InP/ZnS seeded CdS tetrapods and demonstrated the crucial role of their anisotropic tetrapod shape and the staggered band alignment at the interface. Such tetrapod-shaped nanoheterostructures possessed efficient dual emission, high photostability and wide color tunability due to the large valence band offset and suppressed Auger recombination. Via a further sequential cationic-exchange process of as-synthesized type II InP/ZnS seeded CdS tetrapods with Ag^{+} and then Zn^{2+}, we achieved InP/ZnS seeded ZnS Type I tetrapods in **Chapter 3**. These tetrapods exhibited emission in the visible range, about 170 nm blueshifted from their InP/ZnS-CdS counterparts. Coupled with the large absorption cross-section and potentially enhanced charge transport, these branched tetrapods may find newfound utility in solution-processed optoelectronic devices.

Then we have focused on synthesis of free-standing transition metal sulfides 2D nanosheets in **Chapter 4** and **5**. A halide-assisted synthetic route has been established in **Chapter 4**, where we obtained Ni_9S_8 sheet-like nanostructures that possessed an unusual cross-like shape filled with step-like

edges. Due to their unique stoichiometry, large surface-to-volume ratios and numerous exposed edge facets, Ni_9S_8 sheet-like structures could be potentially utilized as TMS-based electrocatalysts for dye-sensitized solar cells[1] or hydrogen evolution from water.[2, 3] The use of halides in promoting sheet-like growth was successfully extended to Cu_2S, where ultrathin triangular nanosheets were produced via addition of halide ions as well. We further adopted Cu_2S as our starting material to realize the Pb-rich PbS nanosheets by cation exchange reaction in **Chapter 5**. The unique facet orientation of as synthesized PbS possessed a special Pb-terminated {111} plane on both top and bottom of the nanosheets in a large lateral dimension which is very difficult to achieve in normal wet chemistry synthetic approach due to the highest surface energy of {111} planes. Furthermore, the Pb-rich nature provided us a great opportunity to retain the n-Type behaviour of PbS semiconductors and help to resist surface oxidation. Our work of n-type PbS nanosheets with novel facet orientation opens up a path for fabrication of high performance quantum junctions with high stability under operation in ambient air. These findings afford deeper insight into the formation of sheet-like semiconductor nanostructures and offer a highly facile route to the colloidal synthesis of such materials.

6.2 Outlook

The colloidal semiconductor heterostructures with branched morphologies are promising candidates for photovoltaic and light emitting devices due to their increased absorption cross section and tunable band alignment at the core-arm interface.[4, 5] The type II InP/ZnS seeded CdS tetrapod we have achieved in this thesis, possess efficient dual wavelength

emission and high photostability, which would be potentially useful for fabrication of tetrapod based LED.

Comparing to branched 3D nanoheterostructures, free-standing 2D nanosheets with lower dimensionality and ultrathin morphology is evolving very rapidly with novel synthetic methods, physical properties and potential applications due to the strong one dimensional confinement effect.[6] We tend to extend the halide ion assisted synthetic method developed in this thesis to other transition metal sulfide nanosheets, such as SnS, CdS et al., which would possess interesting optoelectronic properties for further device application. In addition, with carefully optimization of the parameters, we aim for ultra-large nanosheets with lateral dimension up to a few micrometers while retaining ultrathin thickness. With such 2D semiconductor nanosheets, the electronic measurements performed on single sheet level will be possibly realized.

6.3 References

1. Li, Y.; Wang, H.; Zhang, H.; Liu, P.; Wang, Y.; Fang, W.; Yang, H.; Li, Y.; Zhao, H. *Chem. Commun.* **2014,** 50, 5569.

2. Zhang, W.; Wang, Y. B.; Wang, Z.; Zhong, Z. Y.; Xu, R. *Chem. Commun.* **2010,** 46, 7631.

3. Hong, J. D.; Wang, Y. S.; Wang, Y. B.; Zhang, W.; Xu, R. *ChemSusChem* **2013,** 6, 2263.

4. Tong, S. W.; Mishra, N.; Su, C. L.; Nalla, V.; Wu, W. Y.; Ji, W.; Zhang, J.; Chan, Y.; Loh, K. P., *Adv. Funct. Mater.* **2014,** 24, 1904.

5. Wong, J. I.; Mishra, N.; Xing, G. C.; Li, M. J.; Chakrabortty, S.; Sum, T. C.; Shi, Y. M.; Chan, Y. T.; Yang, H. Y., *ACS Nano* **2014,** 8, 2873.

6. Bouet, C.; Tessier, M. D.; Ithurria, S.; Mahler, B.; Nadal, B.; Dubertret, B., *Chem. Mat.* **2013,** 25, 1262.

LIST OF PUBLICATIONS

1. "**High Performance Hybrid Solar Cell Made from CdSe/CdTe Nanocrystals Supported on Reduced Graphene Oxide and PCDTBT**"

S. W. Tong, N. Mishra, C. L. Su, V. Nalla, **W. Wu**, W. Ji, J. Zhang, Y. Chan* and K. P. Loh* *Adv. Funct. Mater.* **2014**, 24, 1904.

2. "**Promoting 2D growth in colloidal transition metal sulfide semiconductor nanostructures via halide ions**"

W. Y. Wu, S. Chakrabortty, C. K. L. Chang, A. Guchhait, M. Lin * and Y. Chan* *Chem. Mater.* **2014***,* 26, 6120.

3. "**Efficient Color-Tunable Multiexcitonic Dual Wavelength Emission from Type II Semiconductor Tetrapods**"

W. Y. Wu, M. Li, J. Lian, X. Wu, E. K. L. Yeow, M. H. Jhon, Y. Chan* *ACS Nano*. **2014**, 8 (9), 9349.